

THEORY AND NUMERICAL ANALYSIS OF INDEX-ANTIGUIDED WAVEGUIDE
LASERS

by

Chaofan Wang

A dissertation submitted to the faculty of
The University of North Carolina at Charlotte
in partial fulfillment of the requirements
for the degree of Doctor of Philosophy in
Optical Science and Engineering

Charlotte

2017

Approved by:

Dr. Tsing-Hua Her

Dr. Faramarz Farahi

Dr. M. Yasin Raja

Dr. Stuart Smith

ABSTRACT

CHAOFAN WANG. Theory and numerical analysis of index-antiguided waveguide lasers. (Under the direction of DR. TSING-HUA HER)

Index-antiguided (IAG) waveguide is promising for high-power application due to simple step-index structure and the property to introduce higher waveguide loss for higher-order-modes (HOMs). The loss ratio between fundamental mode (FM) and 1st HOM is fixed at 4 for IAG planar waveguides and 2.54 for IAG fibers. Since 2006, robust single-transverse-mode oscillation has been reported both in IAG fibers with diameter up to 400 μm and IAG planar waveguides with 220 μm core width. Although IAG waveguides seem to be promising for large-single-mode operation, the main challenges are the low output efficiency in end-pumped IAG lasers and the effect of HOM oscillation. The objective of the research is to solve the above two challenges.

In this dissertation, both core and cladding pumping schemes are numerically studied, demonstrating that cladding pumping is not efficient in IAG fiber lasers due to both index-antiguiding effect and large core size, and core pumping should be implemented instead. To achieve high output efficiency, laser parameters need to be carefully designed to satisfy that the gain length $L_{gain} = 1/\sigma_{ap}N$ is much smaller than the decay length $L_{decay} = -\ln R_{oc}/2\alpha_s$, and the fiber length should be chosen such that $L_{gain} \leq L \ll L_{decay}$. This conclusion works well to explain the low output efficiency issue for the published experimental results.

In addition, the investigation of transverse mode competition effect in IAG lasers shows that in order to maintain single-mode operation, the maximal extraction efficiency of single-fundamental-mode is suppressed to 66.7% and 50% (from 100%) for IAG slab

and fiber lasers, respectively. This low efficiency is due to the small loss ratio (2.54 for IAG fibers and 4 for IAG planar waveguides) in IAG waveguide lasers.

DEDICATION

To my wife and parents

ACKNOWLEDGEMENTS

I would like to express my deepest gratitude to my advisor, Dr. Tsing-Hua Her, for providing me the opportunity and his excellent guidance on the research. His knowledge, professional experience and great research resource have efficiently guided me to the right research direction.

I would also like to express my gratitude to Dr. Lee Casperson for his guidance and helpful discussion on my research.

I would also like to thank Yuanye Liu and other lab members for their help, encouragement, and friendship during my doctoral study.

Finally, I would like to thank my wife Nan Wu and my parents for their endless supports during my whole life.

TABLE OF CONTENTS

LIST OF FIGURES	X
LIST OF TABLES	XIV
CHAPTER 1 INTRODUCTION	1
1.1 Motivation.....	2
1.2 Outline	3
CHAPTER 2 REVIEW OF HIGH-POWER FIBER LASERS	4
2.1 Application of high-power fiber lasers	4
2.2 Advantages of fiber lasers over conventional solid-state bulk lasers	5
2.3 Limitations of high power capability.....	6
2.4 Large-mode-area fiber lasers and mode area scaling.....	11
2.5 Summary.....	16
CHAPTER 3 INDEX-ANTIGUIDED PLANAR WAVEGUIDE AMPLIFIERS AND LASERS.....	18
3.1 Modal characteristics of index-antiguided planar waveguides.....	19
3.1.1 The complex \tilde{V}^2 number	20
3.1.2 Modal profile and waveguide loss	21
3.2 Index-antiguided planar waveguide amplifiers with homogeneous broadening	24
3.2.1 Model and numerical method	24
3.2.2 Field Evolution.....	26
3.2.3 Power evolution	28
3.2.4 Gain saturation and modal confinement	32
3.2.5 Output intensity and optimized length.....	35
3.3 Index-antiguided planar waveguide lasers with uniform side pumping.....	37

3.4 Transverse mode competition in uniformly side-pumped index-antiguided slab lasers	43
3.4.1 Introduction.....	43
3.4.2 Oscillator model.....	45
3.4.3 The gain oscillation threshold of the first higher-order mode	46
3.4.4 Regions of single-fundamental-mode operation.....	47
3.4.5 Extraction efficiency of single fundamental mode	49
3.5 Summary.....	57
CHAPTER 4 OUTPUT CHARACTERISTICS OF INDEX-ANTIGUIDED FIBER LASERS IN FUNDAMENTALLY SINGLE MODE REGIME	59
4.1 Modal characteristics of index-antiguided fiber lasers.....	60
4.2 Pumping schemes	62
4.2.1 Side pumping	62
4.2.2 End pumping.....	63
4.2.3 Some improvements for end pumping scheme	70
4.3 Output characteristics of uniformly side-pumped index-antiguided fiber lasers....	73
4.4 Output characteristics of core-pumped index-antiguided fiber lasers	75
4.4.1 Oscillator model for core-pumped index-antiguided fiber lasers	76
4.4.2 Improve output efficiency in core-pumped index-antiguided fiber lasers.....	83
4.4.3 Design guidelines to improve the output efficiency in core-pumped index-antiguided fiber lasers	98
4.5 Power limit.....	100
4.6 Summary.....	105
CHAPTER 5 TRANSVERSE MODE COMPETITION IN INDEX-ANTIGUIDED FIBER LASERS	107
5.1 Transverse mode competition in uniformly side-pumped index-antiguided fiber lasers	107

5.1.1 Oscillator model.....	108
5.1.2 Regions of single-fundamental-mode operation.....	109
5.1.3 Extraction efficiency of single fundamental mode	110
5.2 Model validation from published experimental work.....	112
5.3 Transverse mode competition in core-pumped index-antiguidded fiber lasers	114
5.3.1 Oscillator model.....	115
5.3.2 The gain oscillation threshold of the first higher-order mode	116
5.3.3 Regions of single-fundamental-mode operation	117
5.3.4 Extraction efficiency of single fundamental mode	119
5.4 Summary	122
CHAPTER 6 CONCLUSION.....	124
REFERENCES	126
APPENDIX SIMULATION CODE	133

LIST OF FIGURES

Figure 2-1 (a) High-power laser sales from IPG Photonics over the past 5 years and (b) market by end-use [43].	5
Figure 2-2 Typical structure and output single mode of PCFs	12
Figure 2-3 Typical structure of LCFs	14
Figure 2-4 Typical structure of chirally coupled core fibers	15
Figure 2-5 Typical structure of large pitch fibers	15
Figure 3-1 Structure and index profile of an index-antiguided waveguide	19
Figure 3-2 (a) Gain thresholds of FM (solid blue) and 1 st HOM (solid red) in IAG planar waveguides, the dashed lines are the corresponding estimated gain threshold values from Eqs. (3.10) and (3.11). (b) The ratio of gain threshold G_2^{th} / G_1^{th} between FM and the 1 st HOM, showing an asymptotic value of 4 at large $-\Delta N$	23
Figure 3-3 (a-c) Evolution of the electric field amplitude in IAG waveguide for $-\Delta N = 10, 100, \text{ and } 1000$, respectively. (d-f) Gain profiles and (g-i) the corresponding normalized field amplitudes at several distances along the waveguide [24].	26
Figure 3-4 Co-propagation of the FM and 1 st HOM in an IAG planar waveguide with $-\Delta N = 1000$. The vertical scale is the electric field amplitude (V/cm) [24].	27
Figure 3-5 The evolution of the power in the core normalized to the input power along the propagation distance for different strengths of index antiguiding [24]. The solid circles are results obtained from the beam propagation method, and the black solid lines are the analytic results as discussed in the text.	32
Figure 3-6 Modal gain coefficient g_m and decay coefficient w_r of the cladding field as a function of propagating distance for different strength of index antiguiding. Open symbols are obtained from BPM, and lines are obtained from analytical calculation [24].	33
Figure 3-7 Normalized output length (solid colors, referred to the left axis) and output core intensity (dash black, referred to the right axis) as a function of the ratio of unsaturated gain coefficient to the loss coefficient, for different input intensities [24]. ..	36
Figure 3-8 Maximum extraction efficiency versus optimum output coupler reflectance of homogeneously broadened IAG slab lasers for various values of g_0L and αL [25]. ...	40
Figure 3-9 Dependence of the ratio η_r of η_{\max} of IAG slab oscillators to that of plane-wave oscillators on g_0L for different αL [25].	42

- Figure 3-10 Near-field mode profiles at different lasing powers of (a) 3 mW, (b) 61 mW, (c) 237 mW and (d) 512 mW in a 400- μm IAG slab laser, showing clear HOM oscillation [20]. 45
- Figure 3-11 Contour plots of (a) single-pass threshold gain $g_1^{\text{th}}L$ of the fundamental mode, (b) single-pass threshold gain $g_2^{\text{th}}L$ of the 1st HOM, and (c) threshold gain contrast $g_2^{\text{th}} / g_1^{\text{th}}$, as a function of single-pass loss α_1L of the fundamental mode (logarithmic scale) and output coupler R_{oc} (linear scale) [17], in uniformly side-pumped IAG slab lasers. 48
- Figure 3-12 For $\alpha_1L = 0.1$, (a) extraction efficiency of the fundamentally single mode vs. output coupling for selected fixed gains, and (b) threshold gain vs. output coupling for FM and 1st HOM in a MM IAG laser. In (a), red dash-dot-dot is the locus of maximal extraction efficiency of the FM, blue dash-dot is η_1 at the threshold of 1st HOM, and black circle is the maximal single-fundamental-mode extraction efficiency in a MM IAG laser [17]. 51
- Figure 3-13 (a) Maximal extraction efficiency of the single fundamental mode in a multimoded IAG slab laser (η_{SM}^{max}) and optimal output coupler reflectance R_{opt} , for various single-pass gains (solid lines) and distributive losses (dash lines). (b) Same as (a) except maximal extraction efficiency of a fundamentally single-moded laser (η_1^{max}) [17]. 53
- Figure 4-1 (a) Gain thresholds of LP₀₁ (solid blue) and LP₁₁ (solid red) in IAG fiber waveguides, the dashed lines are the corresponding estimated gain threshold values from Eq. (4.4). (b) The ratio of gain threshold $G_2^{\text{th}} / G_1^{\text{th}}$ between FM and the 1st HOM, showing an asymptotic value of 2.54 at large $-\Delta N$ 61
- Figure 4-2 Side pumping scheme for IAG fiber lasers 63
- Figure 4-3 End pumping scheme for IAG fiber lasers (the above figure is an example of core pumping) 64
- Figure 4-4 Power evolution profiles in the core (solid blue) and cladding (solid red) in case of cladding pump for the initial pump field with phase noise amplitudes of (a) $N_p = 0$, (b) $N_p = 0.4$ and (c) $N_p = 1$. Corresponding absorption coefficients of the core power are 279, 233 and 193 m^{-1} , respectively. As a comparison, the power evolution profiles in the core for core pumping (dotted blue) are also plotted, with the absorption coefficient of 278 m^{-1} 66
- Figure 4-5 Power evolutions in core and cladding for flat-top cladding pump in IAG and IG fibers at input phase noise amplitudes of (a) $N_p = 0$ and (b) $N_p = 0.4$ 69
- Figure 4-6 Power evolutions in core and cladding for flat-top cladding pump in IAG and IG fiber lasers with small core diameter of 40 μm and inner cladding of 125 μm , at input phase noise amplitudes of (a) $N_p = 0$ and (b) $N_p = 0.4$ 70

Figure 4-7 (a) Schematic of Bragg IAG fiber, (b) Radial index profile and (c) Schematic of pump and signal propagation in Bragg IAG fibers.....	71
Figure 4-8 Schematic of using dispersion to control the indices of core and cladding	72
Figure 4-9 Maximum extraction efficiency versus optimum output coupler reflectance in uniformly side-pumped IAG fiber lasers for various values of g_0L and αL (fundamentally-single-mode operation is assumed).	75
Figure 4-10 (a) General four-level system such as 1060 nm Nd^{3+} , (b) general three-level system like Er^{3+} , and (c) generalized two-level system.	77
Figure 4-11 Laser parameters that relate to the output efficiency. Here the gain is only dependent on fiber length L , pump absorption $\sigma_{ap}N$ and pump IAG loss α_p , while δ_r is only dependent on fiber length L , output coupler R_{oc} and signal IAG loss α_s	87
Figure 4-12 Output power as a function of input pump power for different pump waveguide losses of 1.01 m^{-1} and 10.1 m^{-1} , while the absorption coefficient is maintained at 278 m^{-1}	89
Figure 4-13 (a) Gain and (b) integrated gain evolutions along the propagation. Here L_{gain} is the defined length corresponding to $1/e$ of the gain.	90
Figure 4-14 Output power as a function of input pump power at different δ_r of 4.5 (solid line), 45 (dashed line) and 0.028 (dotted line).	92
Figure 4-15 Slope efficiency as a function of fiber length for the output coupler of 98%. The simulation parameters are from Table 4-1 (Ref. [21]) except the fiber length is varied.....	95
Figure 4-16 (a) Slope efficiency and (b) corresponding threshold power as a function of fiber length for different output couplers (solid lines), while the dashed lines represents the locus of optimal output couplers. (c) Maximum slope efficiency (solid line) and corresponding optimal fiber length L_{opt} (dashed line) as a function of output coupler R_{oc} . (d) Minimum threshold power (solid line) and corresponding optimal fiber length L_{2_opt} (dashed line) as a function of output coupler R_{oc}	98
Figure 4-17 (a) Polymer temperature (referred to coolant temperature T_c) and (b) Temperature at core center (referred to coolant temperature T_c) as a function of total heat transfer coefficient h , for different heat load of 10, 50, 100, 200 and 500 W/m. The core and cladding diameters are 200 and 340 μm , respectively. The coating thickness is 20 μm	102
Figure 4-18 Polymer temperature (referred to coolant temperature T_c) as a function of total heat transfer coefficient h for (a) different cladding diameter of 340, 400 and 500 μm (with core diameter is 200 μm and the coating thickness is 20 μm) and (b) different	

coating thickness of 20, 50 and 75 μm (with core and cladding diameters of 200 and 340 μm).....	102
Figure 5-1 Contour plot of gain threshold ratio g_2^{th} / g_1^{th} , as a function of single-pass loss $\alpha_1 L$ of the fundamental mode (logarithmic scale) and output coupler R_{oc} (linear scale), in uniformly side-pumped IAG fiber lasers.	109
Figure 5-2 Maximal extraction efficiency of the single fundamental mode in uniformly side-pumped IAG fiber lasers (η_{SM}^{max}) as a function of optimal output coupler reflectance R_{opt} , for various single-pass gains (solid lines) and distributed losses (dash lines).....	111
Figure 5-3 Contour plot of average gain threshold ratio $\bar{g}_2^{th} / \bar{g}_1^{th}$, as a function of single-pass loss $\alpha_1 L$ of the fundamental mode (logarithmic scale) and output coupler R_{oc} (linear scale) in core-pumped IAG fiber lasers.	118
Figure 5-4 Maximal extraction efficiency of the single fundamental mode (η_{SM}^{max}) in a multimoded core-pumped IAG fiber laser as a function of optimal output coupler R_{opt} , for various single-pass gains (solid lines) and distributed losses (dash lines).....	121

LIST OF TABLES

Table 2-1 Scaling factors to maintain a constant V	12
Table 3-1 Solution of the kink points that satisfy the scaling law	57
Table 4-1 Simulation parameters	89
Table 5-1 Solution of the kink points in IAG fiber lasers.....	112
Table 5-2 Calculated threshold power of the 1 st HOM for the data from Ref. [22]	114
Table 5-3 Simulation parameters for Figure 5-3.....	118
Table 5-4 Kink points in core-pumped IAG fiber lasers	122

CHAPTER 1 INTRODUCTION

High-power fiber lasers have been popular during the past decades [1]. Compared to the conventional solid-state bulk lasers, fiber waveguide lasers have advantages of robust single transverse mode, high efficiency, broad gain linewidth, broad absorption band, easy handling, low cost and compact size [1]. With the technology of cladding pumping [2], single-mode core can be efficiently pumped and beam brightness can be largely enhanced with close to 5 orders [3] compared to the pump. Fiber lasers have proven to be power scalable and the output power has greatly increased over the last two decades, with a continuous-wave power from 110W [4] reaching to 10 kW [5] in single-mode operation.

The high power capability of fiber laser is mainly limited by nonlinear effects, such as stimulated Brillouin scattering, stimulated Raman scattering, self-phase modulation and four-wave mixing, as well as thermal effect and facet damage. Large-mode-area (LMA) waveguides are highly desired for high-brightness operation due to their advantages of mitigating the above nonlinear and thermal effects. However, the increase of core size will finally introduce higher-order-modes (HOMs). Several approaches have been proposed to suppress the HOMs using specialty fibers such as photonic crystal fibers [6], photonic bandgap fibers [7, 8], leakage channel fibers [9, 10], chirally coupled core fibers [11, 12], index-antiguided (IAG) fibers [13, 14] and others [15, 16]. Among these techniques, index antiguiding is a relatively simple approach, where the negative index step between core and cladding naturally introduces higher loss for HOMs, with a loss ratio (between fundamental mode - FM and 1st HOM) of 4 [17] for IAG planar waveguides and 2.54 [14] for IAG fibers. The idea of IAG waveguide lasers was firstly proposed by Siegman in 2003 [18] and experimentally demonstrated in 2006 [19] with side flashlamp pump on an IAG

fiber with 100 μm -core diameter. After that, robust single-fundamental-mode oscillation has been reported both in IAG fibers with diameter up to 400 μm [13] and IAG planar waveguides with 220 μm core width [20].

1.1 Motivation

Many LMA fiber structures listed above are aimed to enlarge modal loss (between FM and HOMs) to ensure single-mode operation. IAG waveguides seem to be promising due to its simple step-index structure and property of differential modal loss. Many experiments [13, 19, 21-23] have verified the single-mode operation in IAG waveguide lasers during the past years. Comprehensive theoretical study on IAG amplifiers and lasers were also firstly proposed by us in 2011 [24] and 2012 [25], giving the idea how the laser cavity parameters, such as small-signal gain, internal loss, cavity length and output coupling, affect the output power characteristics. It is noted that the theoretical model only assumes that the IAG waveguide lasers are fundamentally single-moded (*i.e.*, HOMs can never oscillate).

However, recently Liu [20] observed clear HOM oscillation in a 400 μm IAG slab laser. This observation indicates the necessity to consider transverse mode competition due to transverse spatial hole burning [26] in such multimode IAG waveguide lasers. Therefore part of my work will focus on the comprehensive study of the transverse mode competition effect in IAG fiber lasers. In addition, the published result [21] demonstrated very low output efficiency in an end-pumped IAG fiber laser. Therefore another topic of the dissertation will emphasize on improving the output efficiency in end-pumped IAG fiber lasers. In summary, the main topics of the dissertation include:

1. Understand the effect of transverse mode competition in IAG waveguide lasers.

2. Improve output efficiency in end-pumped IAG fiber lasers.

1.2 Outline

The dissertation is structured as follows: In Chapter 2, a review of the high-power fiber lasers will be given including the application of high-power fiber lasers, advantages of fiber waveguide lasers over conventional solid-state bulk lasers, high power limitations and introduction of different types of LMA fibers for high power implementations. Chapter 3 illustrates the theory of IAG planar waveguide lasers, including the modal properties of IAG planar structures, output characteristics of fundamentally single mode (assume no HOMs oscillation) in IAG planar waveguide amplifiers and lasers, and finally the transverse mode competition in IAG slab lasers. Chapter 4 will focus on IAG fiber lasers. The modal property of IAG fibers will be provided and different pumping schemes will be investigated. The efficiency between core and cladding pumping schemes will be carefully studied. The output efficiency in both uniformly side-pumped or core-pumped IAG fiber lasers will be investigated, and the rules to improve the output efficiency in will be given. Chapter 5 focuses on the study of transverse mode competition in IAG fibers lasers. Both oscillator models for uniformly side-pumped and core-pumped IAG fiber lasers with transverse mode competition are provided, with the output characteristics of single fundamental mode (*i.e.*, only FM is oscillated in a multimode laser) comprehensively analyzed. The last chapter is the summary of work and suggestions for future work.

CHAPTER 2 REVIEW OF HIGH-POWER FIBER LASERS

In this chapter, a short review of high-power fiber lasers will be given. The first section introduces the application of high power fiber lasers. The following section discusses the advantages of fiber lasers than traditional solid-state bulk lasers. The third section focuses on the main limitations of high power capability. As it is generally important to pursue high power as well as maintaining single-mode operation, the fourth section will introduce the theory of mode area scaling and provide the background of some general large-mode-area fiber lasers.

2.1 Application of high-power fiber lasers

High-power fiber lasers are widely used in the world. Figure 2-1(a) demonstrates the high-power laser sales from the world largest vendor - IPG Photonics Corporation over the past 5 years, showing an increase of over 15% every year. Figure 2-1(b) demonstrates the high-power laser market by end-use, from which it is seen that majority of the high-power fiber lasers are used for material processing. High-power fiber lasers provide a simple, cost-effective, low-pollution way in cutting, welding and micromachining metals [27, 28], which are widely used in the automotive industry. In addition, 1064- and 532-nm fiber lasers have large impact on the manufacturing of solar cells like scribing the cell interconnect pattern, processing edge isolation grooves and drilling vias [29, 30], due to their advantages of high scribing speed, high reliability and low cost.

In the area of medicine, Tm^{3+} - and Ho^{3+} -doped fiber lasers are also widely implemented [31, 32] as their 2 μm emission wavelength overlaps with the absorption wavelength of O-H bond in water [33]. The incision of soft tissues in many organs like

brain [34, 35], kidneys [36], skins [37, 38] and prostate [39] benefits from these 2- μm lasers due to their excellent ablative and low carbonization properties [40].

Moreover, directed-energy weapons based on high-power fiber lasers are used in many military applications [41], like the detonation of land mines, bombs and rockets [42]. Many ongoing projects like Area Defense Anti-Munitions (ADAM), Excalibur, Laser Weapon System (LaWS) and Robust Electric Laser Initiative (RELI) [41] are dedicated to develop ultra-high-power lasers with over 10s of kilowatt output.

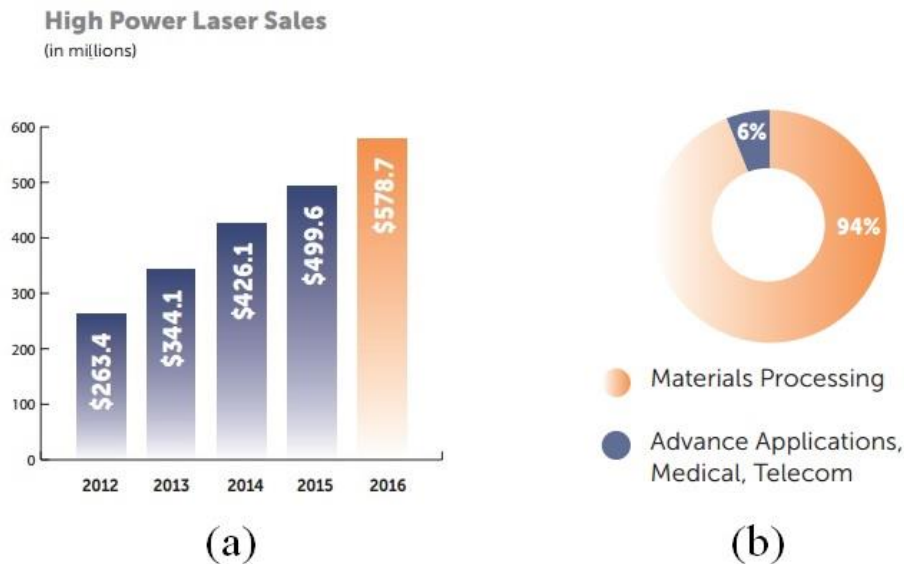


Figure 2-1 (a) High-power laser sales from IPG Photonics over the past 5 years and (b) market by end-use [43].

2.2 Advantages of fiber lasers over conventional solid-state bulk lasers

Fiber lasers are getting more attractions than traditional solid-state bulk lasers due to the following advantages [1],

1. Compact size and easy alignment. Traditional solid-state bulk lasers typically have large gain mediums and cavities than small fiber lasers. Moreover, bulk lasers

- require careful alignment of free-space components, which is more difficult than the alignment of fiberized cavities.
2. High beam quality. The beam quality is often reduced in traditional solid-state bulk lasers due to the thermally induced mode distortion. Therefore, it is difficult for solid-state lasers to maintain a good transverse-mode profile.
 3. High output efficiency. The internal loss in fiber waveguide is smaller than free-space medium, resulting higher output efficiency. Moreover, fiber lasers can work for low-gain conditions while bulk lasers fail to work.
 4. Broad gain linewidth (can achieve 20 THz), which allows wide wavelength tuning range and ultrashort pulse operation.

Although fiber lasers have the above advantages, bulk lasers work better in some scenarios. For instance, bulk lasers have more potential for high pulse energies either with Q switching or mode locking. Fiber lasers are prone to be affected by nonlinear or thermal effects when the peak power is too high. Moreover, bulk lasers are more suitable if there is a requirement of output linearity. In addition, bulk lasers can generate unusual output wavelengths, like the broad tunable Ti: sapphire laser with the wavelengths ranging from 0.7 – 1 μm .

2.3 Limitations of high power capability

As the peak power is getting higher, nonlinear effects [44, 45] like stimulated Brillouin scattering (SBS), stimulated Raman scattering (SRS), self-phase modulation (SPM, occurred in pulsed lasers) and four-wave mixing (FWM) become evident and affect the output performance. Among these, SBS and SRS are the most common limitations in high power fibers, SBS will introduce a small frequency shift of 10 – 20 GHz in silica

fibers while SRS has a larger shift at ~ 13 THz. The threshold power of stimulated Brillouin scattering can be approximated by [46]

$$P_{SBS}^{th} = \frac{21A_{\text{eff}}}{g_B L_{\text{eff}}} \quad (2.1)$$

where A_{eff} is the effective mode area, g_B is the peak Brillouin gain coefficient with a typical value of 5×10^{-11} m/W and L_{eff} is the effective fiber length. The Brillouin gain coefficient is also dependent on the pump laser spectral linewidth with an expression of

$$\tilde{g}_B = g_B \frac{\Delta\nu_B}{\Delta\nu_B + \Delta\nu_P}. \quad (2.2)$$

where $\Delta\nu_B$ is the spectral linewidth of Brillouin gain with typical value of few 10 MHz in silica fiber, while $\Delta\nu_P$ is the spectral linewidth of input pump. Therefore the SBS threshold power is dependent on the pump linewidth.

Compared to Brillouin scattering, the threshold power of stimulated Raman scattering is usually larger, with an approximate expression of [46]

$$P_{SRS}^{th} = \frac{21A_{\text{eff}}}{g_R L_{\text{eff}}}. \quad (2.3)$$

where the peak Raman gain coefficient is $g_R \approx 1 \times 10^{-13}$ m/W in fused silica at the pump wavelength of 1 μm . It is seen from the above equations that large mode area and shorter fiber length will reduce the SBS and SRS effects.

In addition to nonlinear effects, power scaling is also limited by thermal effects which are due to the heat generated by quantum effect and other effects like unabsorbed pump and non-radiative decay. Thermally-induced change of refractive index will alter the beam confinement and therefore lead to beam distortion and thermal lensing [47-49]. The limit of heat load per unit length for thermal lensing effect can be estimated as [49]

$$q_{lens} = \frac{\pi\kappa\lambda_s^2}{2a^2 dn/dT}. \quad (2.4)$$

where κ is the thermal conductivity of the core material, which is 1.38 W/m/K for silica [50]. λ_s is the signal wavelength. a is the core radius and dn/dT is the change of refractive index due to temperature, which is $\sim 1.2 \times 10^{-5} \text{ K}^{-1}$ for silica [50]. The limit of input power is then expressed as

$$P_{lens}^{in} = q_{lens} \frac{L}{\eta_{heat}} = \frac{L}{\eta_{heat}} \frac{\pi\kappa\lambda_s^2}{2a^2 dn/dT}. \quad (2.5)$$

where η_{heat} is the deposit heat efficiency which is mostly estimated as (but actually larger) than $1 - \lambda_p/\lambda_s$, with λ_p the pump wavelength. L is the fiber length. Equation (2.4) indicates that thermal lens is prone to occur if the core size is very large.

Moreover, high power (more accurately, heat load per unit length) will also results in thermal fracture with the limited heat load per unit length estimated as [49]

$$q_{fracture} = \frac{4\pi R_m}{1 - \frac{a^2}{2b^2}}. \quad (2.6)$$

where a is the core radius and b is the cladding radius. R_m is the rupture modulus of the glass, which is between 2500 and 4000 W/m for silica [51].

In addition, high power will cause the melting of the core, with the limit of heat load per unit length expressed as [49],

$$q_{melt} = \frac{4\pi\kappa(T_m - T_c)}{1 + \frac{2\kappa}{bh} + 2\ln \frac{b}{a}}. \quad (2.7)$$

where T_m and T_c are the melting and coolant temperatures, respectively. h is the combined convective and radiative heat transfer coefficient. The convective heat transfer coefficient

could be $\sim 1000 \text{ W/m}^2/\text{K}$ for forced airflow or $\sim 10000 \text{ W/m}^2/\text{K}$ for forced liquid flow cooling [49].

Another damage that is most likely to occur is the thermal damage of the fiber coating. Since most of the polymer coatings work under temperature limit of $\sim 150 \text{ C}$ [52]. Large heat load is likely to induce high temperature in the coating. The limit of heat load for this case is usually smaller than the effect of core melting as the melting temperature of most silica cores is $\sim 1000 \text{ C}$, except some special glass like phosphate which has a lower melting point of $\sim 600 \text{ C}$. The temperature distribution in the transverse and longitudinal direction of the fiber can be solved by the following heat transfer equations [53]

$$\frac{1}{r} \frac{\partial}{\partial r} \left[r \frac{\partial T_1(r, z)}{\partial r} \right] = -\frac{q(r, z)}{\pi a^2}, \quad 0 \leq r \leq a \quad (2.8)$$

$$\frac{1}{r} \frac{\partial}{\partial r} \left[r \frac{\partial T_2(r, z)}{\partial r} \right] = 0, \quad a \leq r \leq b \quad (2.9)$$

$$\frac{1}{r} \frac{\partial}{\partial r} \left[r \frac{\partial T_3(r, z)}{\partial r} \right] = 0, \quad b \leq r \leq c \quad (2.10)$$

together with the following boundary conditions

$$\left. \frac{\partial T_1(r)}{\partial r} \right|_{r=0} = 0. \quad (2.11)$$

$$T_1(r=a) = T_2(r=a), \quad \kappa_1 \left. \frac{\partial T_1(r)}{\partial r} \right|_{r=a} = \kappa_2 \left. \frac{\partial T_2(r)}{\partial r} \right|_{r=a}. \quad (2.12)$$

$$T_2(r=b) = T_3(r=b), \quad \kappa_2 \left. \frac{\partial T_2(r)}{\partial r} \right|_{r=b} = \kappa_3 \left. \frac{\partial T_3(r)}{\partial r} \right|_{r=b}. \quad (2.13)$$

$$\left. \frac{\partial T_3(r)}{\partial r} \right|_{r=c} = \frac{h}{\kappa_3} [T_c - T_3(r=c)]. \quad (2.14)$$

Here $q(r, z)$ is the heat load per unit length which can be estimated as

$$q(r, z) \approx q(z) = P_p(z) \eta_{heat} \alpha(z). \quad (2.15)$$

where $P_p(z)$ is the pump power and $\alpha(z)$ denotes the pump decay coefficient which is the combination of pump absorption coefficient, pump waveguide loss coefficient and scattering loss coefficient. As pump power is the largest at the input end of the fiber, the heat load per unit length is usually largest at the input end. T_1 , T_2 and T_3 are the temperatures in the core, cladding and coating materials, respectively. κ_1 , κ_2 and κ_3 are the thermal conductivities of the core, cladding and coating materials, respectively. a , b and c are the radii of core, cladding and coating. h is the combined convective and radiative heat transfer coefficient and T_c is the coolant temperature. Note that the validity of the above Eqs. (2.8)-(2.10) assumes that the thermal transition in the longitudinal direction is negligible compared to the transverse transition ($\partial^2 T / \partial z^2 \approx 0$), which is usually true for fiber lasers.

Based on the above equations, the temperature distributions can be derived

$$\begin{aligned}
 T_1(r, z) &= T_c + \frac{q(z)}{4\pi} \left[\frac{2}{hc} + \frac{1-(r/a)^2}{\kappa_1} + \frac{2}{\kappa_2} \ln \frac{b}{a} + \frac{2}{\kappa_3} \ln \frac{c}{b} \right], \\
 T_2(r, z) &= T_c + \frac{q(z)}{4\pi} \left[\frac{2}{hc} - \frac{2}{\kappa_2} \ln \frac{r}{b} + \frac{2}{\kappa_3} \ln \frac{c}{b} \right], \\
 T_3(r, z) &= T_c + \frac{q(z)}{4\pi} \left[\frac{2}{hc} - \frac{2}{\kappa_3} \ln \frac{r}{c} \right].
 \end{aligned} \tag{2.16}$$

The limit of heat load per unit length can then be derived based on the limit of coating temperature (say 150 C).

Besides the above mentioned thermal effects, surface damage [54] is another type of damage that will be induced if the incident beam intensity is over a certain damage threshold, which is estimated to be $\sim 10 \text{ W}/\mu\text{m}^2$ [49].

2.4 Large-mode-area fiber lasers and mode area scaling

Large-mode-area (LMA) fibers are desired to reduce the thermal and nonlinear effects which limit the high-power capability. However, the size of the core is limited by single-mode operation, which can be explained by the theory of mode area scaling.

Let us consider a general step-index fiber with a core index slightly higher than the cladding, which ensures the guidance of light based on total internal reflection. The V parameter is used to characterize the guiding property, with the expression of

$$V = k_0 a \sqrt{n_{core}^2 - n_{cl}^2} \approx k_0 a \sqrt{2n_{core} \Delta n} \approx k_0 a \cdot NA. \quad (2.17)$$

where k_0 is the free-space wavenumber, a is the core radius, n_{core} , n_{cl} are the core and cladding indexes, Δn is the index difference between the core and cladding and NA is the numerical aperture. It is well known that a single mode is maintained if V is less than 2.405. This means that, in order to maintain the same single-mode profile with large core radius a , the NA should be relatively reduced. For example, if the core size is increased by a factor of 2, the NA should be reduced by a factor of 2 and Δn needs to be reduced by a factor of 4. The difficulty to precisely control small Δn imposes a limit on large-core fibers with single-mode operation. On the other hand, the change of Δn associates with other parameters such as thermal load [55], bending [56] and Kerr nonlinearity, all of which need to be relatively scaled. When the core size is doubled, the bending radius is scaled by a factor of 2^3 [57], which means a large-core fiber needs to be very straight (large bending radius) in order to maintain the same single mode. This adds more difficulty to the design of fiber rod. In addition, the thermal load needs to be reduced by a factor of 4 [58] in order to maintain the same single mode, which limits the high power capability from the thermal

perspective. All scaling factors are summarized in Table 2-1, from which it is seen that it is difficult to simply increase the core size while maintaining the single-mode property.

Table 2-1 Scaling factors to maintain a constant V

Parameter	Scaling factor
Core diameter	k
NA	$1/k$
Index difference Δn	$1/k^2$
Bending radius	k^3
Thermal load	$1/k^2$

Photonic crystal fiber (PCF) could be a good candidate for LMA fiber lasers and amplifiers, which was first proposed by Birks in 1996 [59], with a typical structure and output single mode shown in Figure 2-2. The NA of PCF is dependent on the pitch and hole size. After proper control of these two parameters, very low NA could be achieved [60] to ensure single mode capability at large core sizes. Some early work [6, 61] demonstrated large-core high-power PCFs with core diameter up to 35 μm and output power of 120 W. However, PCFs with low NA are very sensitive to bending effect, which makes them inappropriate for high average power lasers that usually require long fibers.

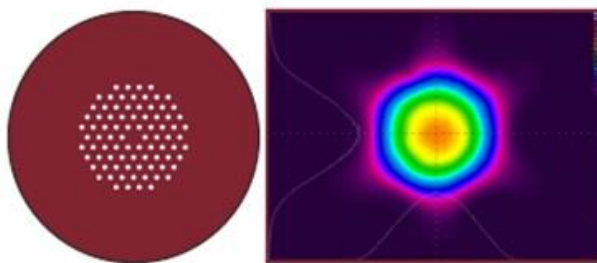


Figure 2-2 Typical structure and output single mode of PCFs

It is seen that PCFs still work in a traditional way to scale the NA and increase the mode size, which turns out to be ineffective. The design of LMA fiber waveguides with effective single-mode operation needs to consider other alternatives which can be categorized into two different types: 1) increase of differential modal loss (between FM and HOMs) and 2) introduction of higher gain for FM than HOMs, or sometimes called HOM delocalization [62]. The general LMA fibers that belong to the first type are photonic bandgap fibers (PBFs) [7, 8], leakage channel fibers (LCFs) [63], chirally coupled core (CCC) fibers [12] and index-antiguided (IAG) fibers [13]. Large pitch fibers (LPFs) [64], distributed mode filtering rod fibers (DMFs) [65, 66] and multitrench fibers (MTFs) [67, 68] belong to the second type where the HOMs are delocalized away from the gain area. Below is a brief review of these general LMA fibers.

Photonic bandgap fibers, which usually include a core surrounded by a cladding that consists of periodic high-index rods embedded in the host material. Modes are confined not by the traditional index-guided structure with higher-index core, but by the bandgap effect from the periodic structure. After proper optimization of the rod-size and pitch [7], PBFs could be designed to easily generate significant loss ratio of over 100 [69] between LP_{01} and LP_{11} . A mode field diameter of $58\ \mu\text{m}$ [69] and power of higher than 900 W [70] was reported using the all-solid PBF.

Leakage channel fibers, with the typical structure shown in Figure 2-3, provide another way to generate large differential modal loss. In LCFs, the cladding shares the same background material (same refractive index) as the core except that several layers of low-index photonic crystal structures, like air holes [71] or fluorine-doped silica glass [72] are embedded. As the core-cladding boundary disappears, all of the propagating modes

suffer transmission loss. The first LCF was demonstrated in 2005 with a simple one layer of air holes [71], generating a large mode field diameter of $\sim 42 \mu\text{m}$. Under proper structure design, the FM loss can be kept for very low while the HOMs suffer higher loss. A loss ratio (between LP_{01} and LP_{11}) of over 10 [73] can be obtained in LCFs, and large core size of over $100 \mu\text{m}$ can be achieved [73, 74].

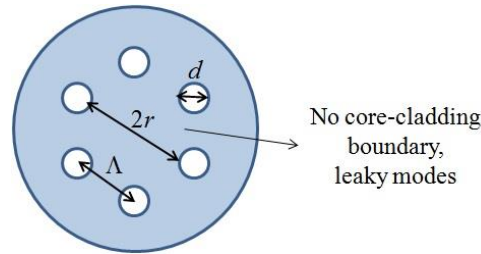


Figure 2-3 Typical structure of LCFs

Index-antiguidded fibers, which are similar to leakage channel fibers, have lower refractive index in the core than the cladding, such that all propagation modes are leaky. The very simple step-index structure creates an intrinsic loss ratio of ~ 2.54 [14] between LP_{01} and LP_{11} , making IAG fiber a promising candidate for high-power fiber lasers. Ultra-large single-mode was reported with core size up to $400 \mu\text{m}$ [13]. The capability of high-power and single-mode operation will be discussed in following chapters.

Chirally coupled core fiber, which was firstly reported in 2007 [75], generally has a large central core accompanied by a smaller helical side core, as shown in Figure 2-4. The helical cores are fabricated by spinning the small-core preform during the draw. In CCC fibers, the HOMs are coupled to the small side core while FM is still confined in the central core. The angular-momentum assisted quasi-phase-matching condition can be used to analyze the mode coupling [76]. As helical structure introduces large bending loss to the HOMs, FM can be differentiated from HOMs. After proper engineering design, over 20

dB differential modal loss [12] can be achieved between LP_{01} and LP_{11} . The reported core diameter of CCC fibers was over $50\ \mu\text{m}$ [12].

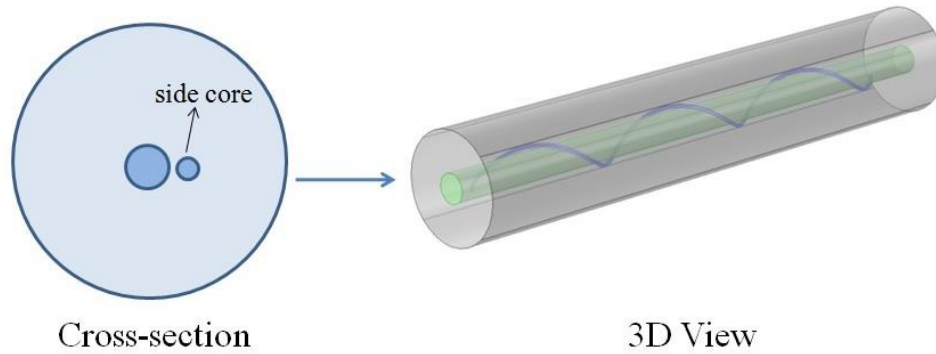


Figure 2-4 Typical structure of chirally coupled core fibers

The above LMA fibers differentiate FM from HOMs based on differential modal loss. Large pitch fibers, on the other hand, operate in a different way named HOM delocalization. The typical structure is shown in Figure 2-5. The design with large pitch (usually > 10 times of the wavelength) will push the HOMs away from the central core area where the doping material usually dominates. As a result, FM will enjoy much larger gain than HOMs due to the larger overlap of FM and doped region. A $100\ \mu\text{m}$ mode-field diameter and $100\ \text{W}$ of average output power was successfully demonstrated in a LPF [77]. The idea of HOM delocalization was also implemented in other LMA fibers like DMFs [66] and MTFs [68].

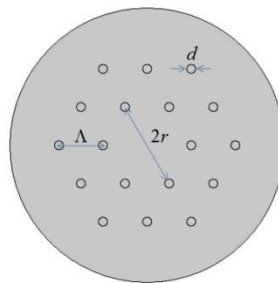


Figure 2-5 Typical structure of large pitch fibers

2.5 Summary

High-power fiber lasers are widely used in many applications, such as military, automotive manufacturing, medicine and other general material processing. Compared to traditional solid-state bulk lasers, fiber lasers have smaller size, better mode quality, smaller loss, easier alignment, broader gain linewidth, etc. The peak power in fiber lasers is limited due to the nonlinear effects like SBS and SRS, thermal effects and surface damage. Large-mode-area fibers are desired to reduce the nonlinear effects and increase the output power. However, in order to maintain single-mode operation, it is seen from the theory of mode area scaling that the numerical aperture needs to be inversely scaled if the core size is increased. As it is generally difficult to manufacture very small numerical aperture (< 0.06) in step-index fibers, the core size is limited to ensure single-mode operation. Photonic crystal fibers can yield very small numerical aperture as it is dependent on the pitch and hole size. However, they are very sensitive to bending effect which makes them unsuitable for high power applications where long fibers are usually desired. Several large-mode-area fiber lasers adopt a different way for single-mode operation by increasing the differential loss between the fundamental and higher-order modes. Examples belong to this type are photonic bandgap fibers, leakage channel fibers, index-antiguided fibers and chirally coupled core fibers, within all of which only index-antiguided fibers were experimented to show single-mode output in ultra large core up to $400\ \mu\text{m}$ while others with core size generally less than $100\ \mu\text{m}$. The second type of large-mode-area fibers achieve single-mode operation by delocalizing the higher-order-modes away from the center area where gain material is doped, therefore yielding lower gains for higher-order-

modes. Typical examples belong to the second type is the large pitch fiber with the demonstrated mode size to 100 μm .

As index-antiguided fibers have simple structure which intrinsically introduce differential modal loss and experimentally yield ultra large single mode. The topic of the dissertation will focus on high power and single mode capabilities of index-antiguided waveguide lasers. The following chapter will first investigate index-antiguided planar waveguide lasers.

CHAPTER 3 INDEX-ANTIGUIDED PLANAR WAVEGUIDE AMPLIFIERS AND LASERS

In Chapter 2, a brief literature review of high-power fiber lasers is given and the limitation of high power capability is discussed. Some LMA fibers that could yield high output power are introduced. Among these LMA fibers, IAG fiber is attractive as its unique structure naturally induces differential modal loss between fundamental mode and higher-order modes. Chapter 3 will first focus on the theory of IAG planar waveguide lasers and following chapters will investigate IAG fiber lasers.

The outline of Chapter 3 is as follows. Section 3.1 introduces the general IAG structures, the important parameter of complex V number and the property of modal loss in IAG planar waveguides. In sections 3.2, we will investigate the propagation characteristics of gain-guided modes in IAG planar waveguide amplifiers. We show that the gain-guided mode has modal confinement proportional to the modal gain, and single-transverse mode propagation is very robust in such waveguides. The power evolution of the fundamental mode could be described analytically with very good accuracy. Limiting power and optimum length of the waveguide amplifiers could also be obtained analytically. In section 3.3, we will numerically analyze the output characteristics of IAG slab lasers with uniform side pumping. A model is proposed that describes a bidirectional homogeneously broadened IAG slab lasers with arbitrary single-pass gain and distributed losses. Maximum extraction efficiency and corresponding optimum output coupling are determined for various values of unsaturated gain and loss per pass.

It needs to note that all the previous analysis only considers fundamentally single mode, that is, assuming no existence of HOMs. In high-power fiber lasers, the robustness

of single-mode oscillation is also significant and there was already the observation of HOM oscillation in an IAG slab laser [20]. Thus, in section 3.4 we will provide a comprehensive analysis of single mode capability in uniformly side-pumped IAG slab lasers. Specifically, the oscillator model with transverse mode competition is introduced. The gain oscillation threshold of the first HOM will be calculated with a proposed semi-analytical method and the characteristics of the threshold will be analyzed. Moreover, the output characteristics of single fundamental mode (which means multimode lasers operate in FM only) will be completely investigated. The last section is a summary of IAG planar waveguide lasers.

3.1 Modal characteristics of index-antiguided planar waveguides

Traditional planar or fiber waveguides are index-guided (IG), that is, the refractive index of the core is higher than the cladding and the propagation modes are confined through the total internal reflection at the core-cladding interface. Index antiguiding, on the other way, has smaller refractive index in the core than the cladding, which results in waveguide loss during propagation. Figure 3-1 demonstrates a general IAG structure in which total internal reflection will not be satisfied and all propagation modes are lossy.

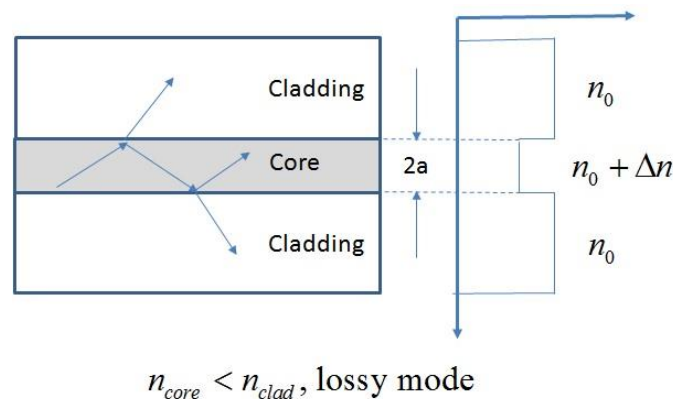


Figure 3-1 Structure and index profile of an index-antiguided waveguide

3.1.1 The complex \tilde{V}^2 number

In traditional IG planar or fiber waveguides, a dimensionless parameter V number is generally used to characterize the propagation modes, which could be expressed as

$$V^2 = k_0^2 a^2 \left[(n_0 + \Delta n)^2 - n_0^2 \right]. \quad (3.1)$$

here k_0 is the vacuum wavenumber, a is the core radius, $n_0 + \Delta n$ and n_0 are the refractive indices of core and cladding, respectively. In order to achieve single-mode operation, the V number should be smaller than $\pi/2$ in planar waveguides and smaller than 2.405 in fiber waveguides. Modes could propagate without loss (absorption is not considered) due to index guiding and no gain is needed to confine the modes.

In IAG waveguides, modes are lossy with a loss coefficient of α . Sufficient gain g_0 is needed ($\geq \alpha$) to confine the propagation modes. In order to characterize the propagation modes like in traditional IG waveguides, the same parameter \tilde{V} could be introduced except that \tilde{V}^2 is a complex number due to the gain. The expression of \tilde{V}^2 is

$$\tilde{V}^2 = k_0^2 a^2 \left[(n_0 + \Delta \tilde{n})^2 - n_0^2 \right] = k_0^2 a^2 \left[\left(n_0 + \Delta n + i \frac{g_0}{2k_0} \right)^2 - n_0^2 \right]. \quad (3.2)$$

Equation (3.2) could be further decomposed into real and imaginary parts

$$\tilde{V}^2 = k_0^2 a^2 \left[\left(n_0 + \Delta n + i \frac{g_0}{2k_0} \right)^2 - n_0^2 \right] \approx k_0^2 a^2 2n_0 \left(\Delta n + i \frac{g_0}{2k_0} \right) = \Delta N + iG. \quad (3.3)$$

where

$$\begin{aligned} \Delta N &= k_0^2 a^2 2n_0 \Delta n, \\ G &= k_0^2 a^2 2n_0 \frac{g_0}{2k_0}. \end{aligned} \quad (3.4)$$

here ΔN characterize the differential index between core and cladding, which is a negative value ($-\Delta N > 0$) for IAG waveguides. G is the parameter associated with the gain. In the next section, we will show that the propagation modes can be characterized with the two parameters ΔN and G .

3.1.2 Modal profile and waveguide loss

The expression of modal profiles in IAG planar waveguides are the same as in IG planar waveguides, except that the parameters \tilde{U} and \tilde{W} are complex. For fundamental slab mode with a core thickness of $2a$ in the direction of x , the modal profile could be expressed as

$$E(x, z) = \begin{cases} \cos(\tilde{U}x/a)e^{-i\tilde{\beta}z}, & (|x| \leq a) \\ \cos(\tilde{U}) \exp[-\tilde{W}(|x|/a - 1)]e^{-i\tilde{\beta}z}. & (|x| > a) \end{cases} \quad (3.5)$$

with

$$\begin{aligned} \tilde{V}^2 &= \tilde{U}^2 + \tilde{W}^2, \\ \tilde{\beta}^2 &= (n_{core}k_0a)^2 - \tilde{U}^2 = k_0^2a^2(n_0 + \Delta n + i\frac{g_0}{2k_0})^2 - \tilde{U}^2. \end{aligned} \quad (3.6)$$

here $\tilde{\beta}$ is the complex propagation constant. After applying the boundary conditions - the continuity of tangential fields E and H , the same characteristic equations could be obtained for IAG planar waveguides. For special case of FM and 1st HOM, the characteristic equations are

$$\begin{aligned} \tilde{W} &= \tilde{U} \tan \tilde{U}, & \text{symmetric modes} \\ \tilde{W} &= \frac{-\tilde{U}}{\tan \tilde{U}}, & \text{asymmetric modes} \end{aligned} \quad (3.7)$$

The above equation could be solved to show the propagation regions for different modes. Figure 3-2(a) plots the gain thresholds of FM (G_1^{th} , solid blue) and the 1st HOM (G_2^{th} , solid red) in IAG planar waveguides. In order to confine the FM and 1st HOM, the required gain G should be chosen above the solid blue and solid red lines, respectively. The propagation of only FM requires the gain G to be located within G_1^{th} and G_2^{th} . In addition, the threshold values could be simply estimated for large $-\Delta N$, which is derived as follows. At large $-\Delta N$, the modes nearly have zero field at the core-cladding interface. Therefore for FM there is $\tilde{U} \approx \pi/2$ and $\tan \tilde{U} = 1/\tan(\pi/2 - \tilde{U}) \approx 1/(\pi/2 - \tilde{U})$. Finally, the characteristic equation of FM in Eq. (3.7) could be modified to

$$\tilde{W} = \frac{\pi/2}{\pi/2 - \tilde{U}}. \quad (3.8)$$

For a confined mode, the fields in the cladding should have no exponential growth or decay, which means the real part of \tilde{W} is zero. Assume $\tilde{W} = W_r + iW_i$, substitute Eq. (3.8) to Eq. (3.3) and set $W_r = 0$, yielding

$$W_i \approx \sqrt{-\Delta N}. \quad (3.9)$$

and the threshold gain for the FM could be estimated

$$G_{1_est}^{th} = (\pi/2)^2 \sqrt{-4/\Delta N}. \quad (3.10)$$

Likewise, the threshold gain for the 1st HOM has a simple analytical expression at large $-\Delta N$

$$G_{2_est}^{th} = \pi^2 \sqrt{-4/\Delta N}. \quad (3.11)$$

The estimated thresholds from Eqs. (3.10) and (3.11) are plotted as the dashed lines in Figure 3-2(a). Excellent agreement could be seen for $-\Delta N \geq 100$.

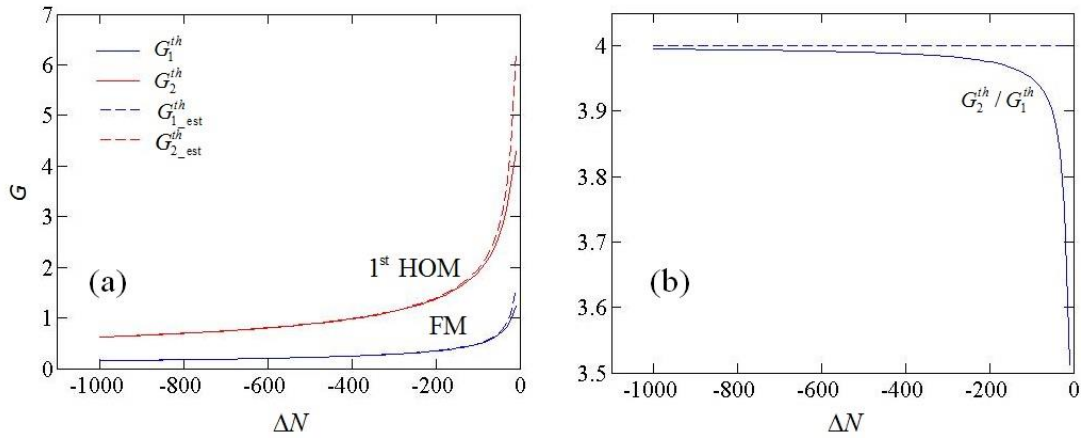


Figure 3-2 (a) Gain thresholds of FM (solid blue) and 1st HOM (solid red) in IAG planar waveguides, the dashed lines are the corresponding estimated gain threshold values from Eqs. (3.10) and (3.11). (b) The ratio of gain threshold G_2^{th} / G_1^{th} between FM and the 1st HOM, showing an asymptotic value of 4 at large $-\Delta N$.

Figure 3-2(b) demonstrates the gain threshold ratio (G_2^{th} / G_1^{th}) between FM and the 1st HOM. It is seen that at larger $-\Delta N$, the gain threshold ratio is

$$G_2^{th} / G_1^{th} \approx \frac{\pi^2 \sqrt{-4 / \Delta N}}{(\pi / 2)^2 \sqrt{-4 / \Delta N}} = 4. \quad \text{IAG planar} \quad (3.12)$$

The modal loss in IAG planar waveguide is very close to the gain threshold calculated in Figure 3-2. At large $-\Delta N$, the modal could be estimated as

$$\begin{aligned} \alpha_1 &\approx \frac{k_0}{(k_0 a)^2 n_0} G_1^{th} = \frac{\pi^2}{2k_0 a^2 n_0 \sqrt{-\Delta N}}, \\ \alpha_2 &\approx \frac{k_0}{(k_0 a)^2 n_0} G_2^{th} = 4\alpha_1. \end{aligned} \quad \text{IAG planar} \quad (3.13)$$

where α_1 and α_2 are the losses of FM and 1st HOM, respectively. It is seen that the loss ratio between FM and 1st HOM is 4 in IAG planar waveguides for large $-\Delta N$.

3.2 Index-antiguidded planar waveguide amplifiers with homogeneous broadening

The previous section illustrates the characteristics of propagation modes in IAG planar waveguides. In this section, we will present a thorough study of the characteristics of the fundamental mode in IAG planar waveguide amplifiers. A simplified analytical model for IAG planar waveguide amplifier will be introduced, which agrees well with the numerical result using finite-difference beam propagation method (FD-BPM). The property of power evolution with different $-\Delta n$ is analyzed, as well as the optimum length for the amplifier.

3.2.1 Model and numerical method

Consider an IAG planar waveguide with a core thickness of $2a$ in the x (*i.e.*, guided) direction that extends infinitely in the z propagation direction and has both a constant index step Δn ($\Delta n < 0$) with respect to the cladding and a uniform unsaturated power gain coefficient g_0 inside the core. The scalar complex electric field in the planar waveguide could be expressed as $\tilde{E} = \tilde{\psi}(x) \exp[i(\tilde{\beta}z - \omega t)]$, where $\tilde{\beta} = \beta_r + i\beta_i$ is the complex propagation constant and ω is the angular frequency. In the case of symmetric modes in a symmetric planar waveguide, the FM field amplitude has the following form

$$\tilde{\psi}(x) = \begin{cases} \cos(\tilde{U}x/a) & (|x| \leq a) \\ \cos(\tilde{U}) \exp[-\tilde{W}(|x|/a - 1)] & (|x| \geq a) \end{cases} \quad (3.14)$$

where $\tilde{U} = U_r + iU_i$ and $\tilde{W} = W_r + iW_i$ are the complex-valued mode parameters illustrated in Eq. (3.6).

For a gain medium that is homogeneously broadened, the complex refractive index profile $\tilde{n}(x, z)$ could be written as

$$\tilde{n}(x, z) = \begin{cases} n_0 + \Delta n - i \frac{n''}{1 + sI(x, z)} & (|x| \leq a) \\ n_0 & (|x| > a) \end{cases} \quad (3.15)$$

where $I(x, z) \propto |\tilde{\psi}(x, z)|^2$ is the light intensity, s is the saturation parameter defined as the inverse of the saturation intensity I_s , and n'' is related to g_0 by $g_0 = 2k_0 n''$. The evolution of the electric field is at first numerically calculated using a standard finite-difference beam propagation method (FD-BPM) with perfectly matched layers as boundary conditions [78, 79]. We solve for the envelope function $\tilde{\psi}(x, z)$ of the scalar electric field $\tilde{E} = \tilde{\psi}(x) \exp[i(\bar{k}z - \omega t)]$ where \bar{k} is the reference wavenumber which could be taken to be β_1 . The launch field is the unsaturated fundamental mode with peak amplitude equal to 0.01. A step size of 1 μm is used for both x and z directions. During the propagation, the index profile in Eq. (3.15) is updated using the intensity distribution of the previous z -step. In this work, we investigate an IAG planar waveguide with a core thickness $2a$ of 100 μm , and the dimensionless index parameter ΔN between 10 and 1000 by changing the refractive index of the core according to Eq. (3.4). We also consider Nd:YAG as a gain media [80, 81] with an operating wavelength $\lambda = 1.05 \mu\text{m}$, an unsaturated power gain coefficient $g_0 = 1.5 \text{ cm}^{-1}$ and a saturation intensity of 3 kW/cm^2 . The cladding index is assumed to be $n_0 = 1.82$, The simulation is carried out over a distance of 30 cm along the z direction in order to examine the saturation behavior.

3.2.2 Field Evolution

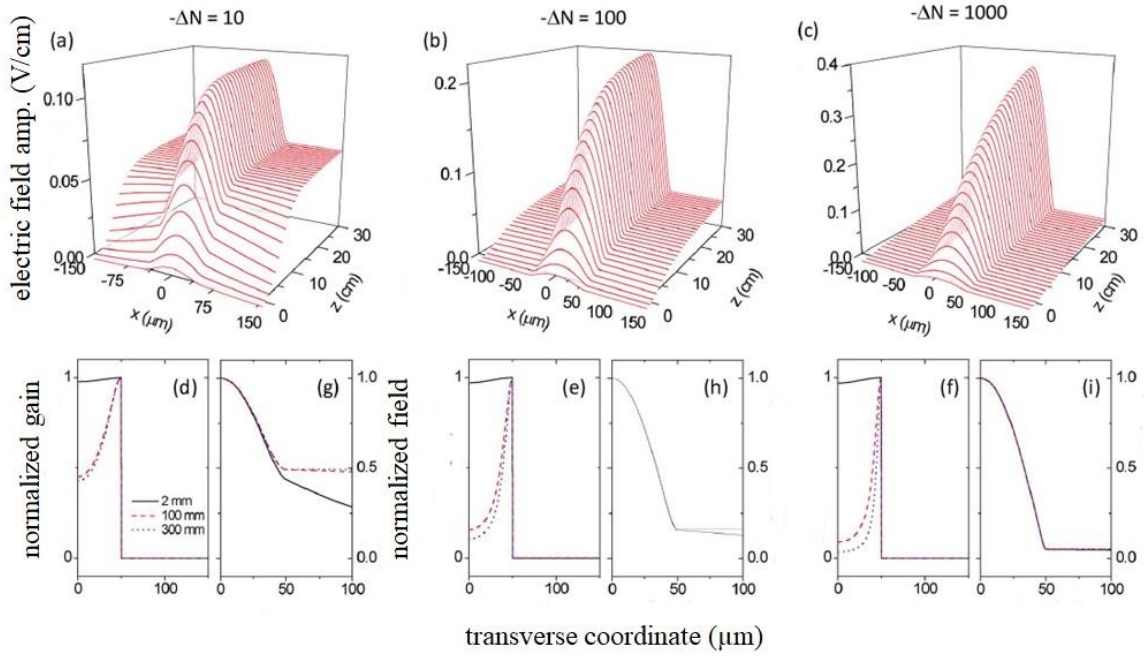


Figure 3-3 (a-c) Evolution of the electric field amplitude in IAG waveguide for $-\Delta N = 10$, 100, and 1000, respectively. (d-f) Gain profiles and (g-i) the corresponding normalized field amplitudes at several distances along the waveguide [24].

Figure 3-3(a-c) show the evolution of the field amplitude $|\psi(x, z)|$ along the z direction in a weak ($-\Delta N = 10$), medium ($-\Delta N = 100$), and strong ($-\Delta N = 1000$) IAG planar waveguide. For all cases under study, the field amplitudes grow initially and then saturate. This is confirmed in Figure 3-3(d-f) which show the transverse profiles of power gain coefficients at propagation distance of 2, 100 and 300 mm. The corresponding normalized mode profiles of the fundamental mode are shown in Figure 3-3(g-i). At short distance of 2 mm where the gain is nearly uniform across the core (solid black lines), the unsaturated field amplitudes follow Eq. (3.14) with different decay coefficients determined by the electromagnetic boundary conditions. At long distance where the gain saturation becomes most noticeable at the center of the mode, the field amplitudes in the cladding all become

cutoff-like extending infinitely in the transverse direction. For weak IAG ($-\Delta N = 10$), saturation occurs earlier in propagation with low limiting powers, and the mode shape changes substantially from highly confined to nearly cutoff (Figure 3-3(g)). For strong IAG ($-\Delta N = 1000$), saturation occurs at long distance with much larger limiting intensities, and the mode shape remains nearly identical during propagation (Figure 3-3(i)).

Figure 3-4 shows BPM simulation of co-propagation of the FM and 1st HOM in an IAG waveguide with $-\Delta N = 1000$. At short distance beating between these two modes due to different propagation constants is clearly observed. As distance increases the beating gradually disappears and the field pattern evolves into that of a pure FM. The diminishing HOM during the co-propagation with the FM is due to its higher propagation loss at the presence of gain saturation. Figure 3-4 clearly indicates that the single-transverse-mode operation is robust in IAG waveguides.

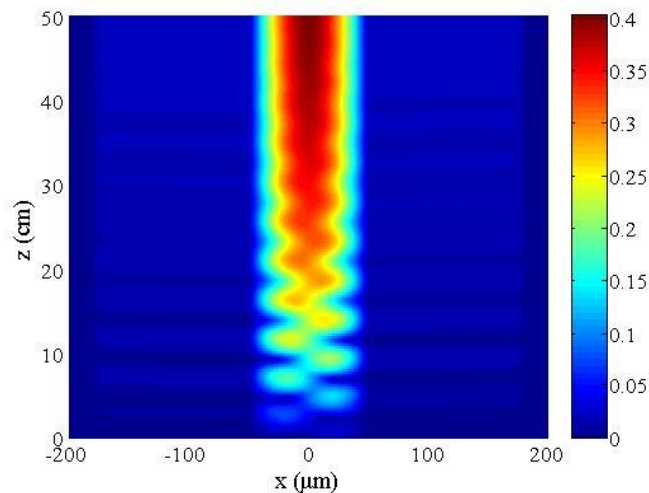


Figure 3-4 Co-propagation of the FM and 1st HOM in an IAG planar waveguide with $-\Delta N = 1000$. The vertical scale is the electric field amplitude (V/cm) [24].

3.2.3 Power evolution

Understanding power evolution in laser amplifiers is critical to extract information such as maximum output power and optimum device length. Since the fields of leaky modes cannot be normalized properly, here we are concerned with power in the core per unit length along the unguided (y) direction, defined by the integrated intensity in the core along the guided (x) direction, *i.e.*, $P_c(z) = \int_{-a}^a I(x, z) dx$. For a uniform plane wave propagating in a homogeneously broadened medium with a power loss coefficient α , the intensity saturates according to [82]

$$\frac{dI(z)}{dz} = \frac{g_0}{1 + sI(z)} I(z) - \alpha I(z). \quad (3.16)$$

For propagating modes with non-uniform spatial dependence which leads to transverse spatial hole burning in the gain profile, Casperson has shown that the total power could be determined if the mode profile is known along the propagation length [26]. This is the case for IAG waveguides, as illustrated in Figure 3-3(g-i) which shows the mode profiles inside the core stay nearly identical to those of the unsaturated mode. We therefore define a normalized intensity profile $f_c(x)$ inside the core by $\int_{-a}^a f_c(x) dx = 1$ such that the local intensity could be written as

$$I(x, z) = P_c(z) \cdot f_c(x). \quad (3.17)$$

If Eq. (3.17) is substituted into Eq. (3.16), the result could be integrated over the guided direction to yield a differential equation for the evolution of $P_c(z)$ along the propagation direction

$$\frac{dP_c(z)}{dz} = g_0 \int_{-a}^a \frac{f_c(x) P_c(z)}{[1 + s f_c(x) P_c(z)]} dx - \alpha P_c(z). \quad (3.18)$$

The net modal gain coefficient g_m could be written as

$$g_m = \frac{1}{P_c(z)} \frac{dP_c(z)}{dz} = g_0 \int_{-a}^a \frac{f_c(x)}{[1 + sf_c(x)P_c(z)]} dx - \alpha. \quad (3.19)$$

where the first term on the right-hand side is the effective net gain taking into account the transverse gain saturation, and the second term is the modal loss coefficient which has been shown equal to that of the corresponding passive IAG waveguides [83]. Recognizing that $P_c(z)/2a$ is equivalent to the core intensity averaged along the guided direction, we thereby define a dimensionless normalized average core intensity $I'_c(z) = sP_c(z)/2a$.

Equation (3.18) could then be re-written as

$$\frac{dI'_c(z)}{dz} = g_0 \int_{-a}^a \frac{f_c(x)I'_c(z)}{[1 + 2af_c(x)I'_c(z)]} dx - \alpha I'_c(z). \quad (3.20)$$

Equation (3.20) describes the evolution of the normalized average intensity in the core along the waveguide. By solving the modal characteristic equation in section 3.1, it could be easily shown that for $-\Delta N \geq 100$, U_r is very close to $\pi/2$ with negligible U_i (≤ 0.2). The normalized intensity profile $f_c(x)$ could then be approximated by a real cosine squared function to be $f_c(x) \approx \cos^2(U_r x/a)$. The integration in Eq. (3.20) could then be carried out analytically which yields

$$\frac{dI'_c}{dz} \approx g_0 \left(1 - \frac{\tan^{-1}\left(\tan U_r / \sqrt{1 + 2I'_c}\right)}{U_r \sqrt{1 + 2I'_c}} \right) - \alpha I'_c. \quad (3.21)$$

Furthermore, as U_r is very close to $\pi/2$ and I_c' is a finite number, the above equation could be simplified if one approximates $\tan^{-1}\left(\tan U_r / \sqrt{1+2I_c'}\right)$ by U_r , which leads to an ordinary differential equation for normalized average core intensity

$$\frac{dI_c'}{dz} \approx g_0 \left(1 - \frac{1}{\sqrt{1+2I_c'}}\right) - \alpha I_c' = g_0 I_c' \left[\frac{1}{I_c'} \left(1 - \frac{1}{\sqrt{1+2I_c'}}\right) \right] - \alpha I_c'. \quad (3.22)$$

Equation (3.22) provides a good description of the core power of the fundamental mode propagating along planar IAG waveguides. Its role in determining the propagation characteristics for the fundamental mode in IAG planar waveguides is as important as Eq. (3.16) is for plane waves in unbounded homogeneously broadened media [82]. For example, the net modal gain coefficient defined by Eq. (3.19) could be simplified to a pure analytic function as

$$g_m \approx \frac{g_o}{I_c'} \left(1 - \frac{1}{\sqrt{1+2I_c'}}\right) - \alpha. \quad (3.23)$$

At low intensity where $I_c' \ll 1$, Eq. (3.22) is reduced to

$$\frac{dI_c'}{dz} \approx (g_0 - \alpha) I_c'. \quad (3.24)$$

which indicates that the core power experiences a uniform gain, as expected. Furthermore, limiting normalized core intensity I_{lim}' could be obtained by imposing the condition of zero net modal gain in Eq. (3.23) which yields

$$I_{\text{lim}}' = \eta - (\sqrt{8\eta + 1} + 1) / 4. \quad (3.25)$$

where $\eta = g_0/\alpha$ is the ratio of the unsaturated gain coefficient to the loss coefficient.

Notice that the above equation could be re-written as $I'_{sat} = \eta - 1 - (\sqrt{8\eta + 1} - 3)/4$, where $\eta - 1$ is the well known saturated intensity of a plane wave.

The normalized intensity I'_c in Eq. (3.22) could be solved analytically by introducing another intermediate parameter $R = \sqrt{1 + 2I'_c}$. Rearrange Eq. (3.22) to

$$\frac{dz}{dR} \approx \frac{2R^2}{(R-1)[2g_0 - \alpha R(R+1)]} \quad (3.26)$$

Integrate Eq. (3.26) over R to obtain

$$z = \frac{(\alpha + 2g_0) \operatorname{atanh} \frac{\sqrt{\alpha}(1+2R)}{\sqrt{\alpha+8g_0}}}{\sqrt{\alpha(\alpha+8g_0)}(g_0-\alpha)} + \frac{2\alpha \ln(R-1) - (2g_0 - \alpha) \ln(\alpha R(R+1) - 2g_0)}{2\alpha(g_0 - \alpha)} + C. \quad (3.27)$$

where the constant C could be determined by the input $z(R_m) = 0$. The results of Eq. (3.27) for IAG waveguides with $-AN$ equal to 10, 100, and 1000 are shown as solid black lines in Figure 3-5. For comparison, the evolution of the core power obtained from BPM normalized to input power (*i.e.*, power gain) is also shown as open red circles. For all cases considered, the analytical results agree reasonably well with the simulation, which validates the initial assumption that the field profiles within the core of these IAG slabs remain invariant and could be approximated fairly accurate as $\cos(\pi x/2a)$. This result confirms that Eq. (3.22) provides a fairly accurate analytic description of the intensity evolution of the fundamental mode in IAG planar waveguides.

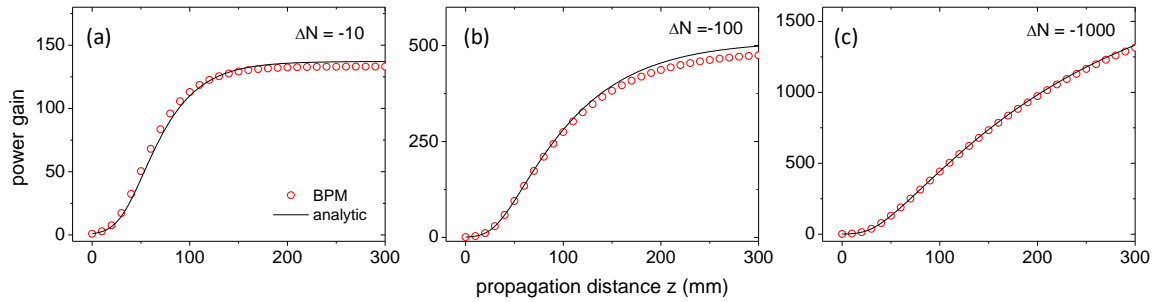


Figure 3-5 The evolution of the power in the core normalized to the input power along the propagation distance for different strengths of index antiguiding [24]. The solid circles are results obtained from the beam propagation method, and the black solid lines are the analytic results as discussed in the text.

3.2.4 Gain saturation and modal confinement

Figure 3-3 (g-i) indicates that the propagating modes become less and less confined as the gain diminishes upon gain saturation. In Figure 3-6 we compare the net modal gain coefficient g_m and cladding field decay coefficient W_r as a function of propagation distance, calculated both from BPM (open symbols) and from analytical results (lines) for different ΔN . The two calculations show very good agreement, especially for large IAG, validating the accuracy of Eq. (3.22). At short distance, the net modal gain coefficient g_m (red open circles) roughly equals g_0 , beyond which it starts to decrease until it settles into a single exponential decay at large distance. The weaker the IAG, the larger the decay coefficient is. This implies that the propagating modes in a weak IAG waveguide could only grow over a relatively shorter distance to have smaller amplitude before saturation, whereas modes in a strong IAG waveguide could grow over a longer distance to reach a much larger limiting intensity – an indication that is consistent with the observation in Figure 3-5. Such a trend could be understood by considering the decay coefficient γ of the net gain coefficient g_m , which is equal to the negative of the slope of the black solid lines in Figure 3-6. The decay coefficient γ could be derived from Eq. (3.22) to be

$$\gamma(z) = -\frac{1}{g_m(z)} \frac{dg_m}{dz} = g_0 \frac{(1+2R)(R^2-1)}{R^3(R^2+1)}. \quad (3.28)$$

At short distance with low intensity, $R \approx 1$ and γ is zero. At large distance where R approaches its limiting value $R_{\text{lim}} = \sqrt{1+I'_{c,\text{lim}}} = (\sqrt{1+8\eta}-1)/2$, γ is a monotonically decreasing function of R . This explains the faster gain saturation in IAG waveguides with small $-\Delta N$.

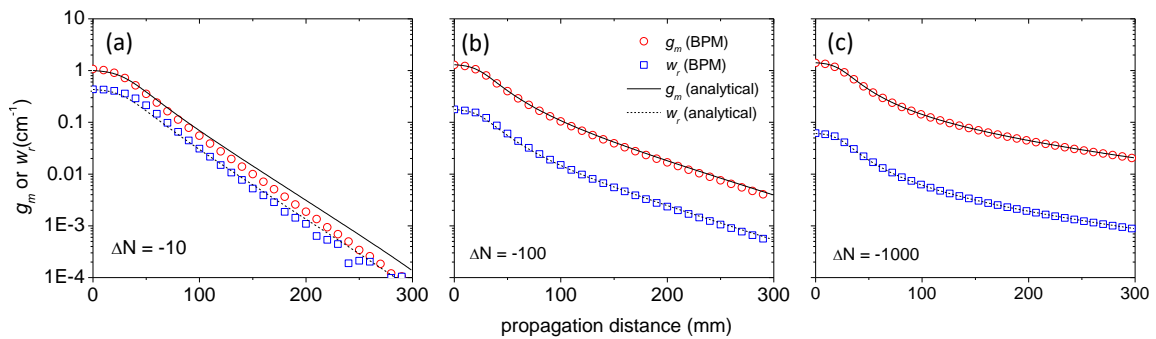


Figure 3-6 Modal gain coefficient g_m and decay coefficient w_r of the cladding field as a function of propagating distance for different strength of index antiguiding. Open symbols are obtained from BPM, and lines are obtained from analytical calculation [24].

Figure 3-6 also indicates that, over the entire distance of propagation, the cladding-field decay coefficient w_r (blue open squares) is linearly proportional to the net gain coefficient g_m (red open circles), as indicated by the constant offset in the log-linear plot. Such a linear proportionality ensures that, as gain saturation reduces the net gain, the field in the cladding becomes proportionally less confined, leading asymptotically towards a cut-off-like distribution as the net gain approaches zero. This linear correlation could be understood by examining the relationship between the complex modal parameter \tilde{W} and the complex effective propagation constant $\tilde{\beta}$ in the phase matching condition. From Eq. (3.6), we have $\tilde{W}/a = \sqrt{\tilde{\beta}^2 - k_0^2 n_0^2} = i\delta(1 - i2\beta_r\beta_i/\delta^2)^{1/2}$, where $\delta^2 = -\Delta N/a^2$ is

positive due to index antiguiding. For a large core waveguide, $\beta_r \beta_i / \delta^2 \sim \text{Im}(n_{\text{eff}}) / 2\Delta n$ is on the order of $10^{-5} / 10^{-3}$, which is very small compared to unity. w_r could then be approximated as

$$w_r \approx \frac{a^2 \beta_r \beta_i}{\sqrt{-\Delta N}} \approx \frac{k_0 a^2 n_0}{2\sqrt{-\Delta N}} g_m \quad (3.29)$$

This equation indicates that the decay coefficient of the field amplitude in the cladding is linearly proportional to the net gain coefficient, which is in good agreement with our BPM numerical result. We emphasize that such a behavior is a unique feature of gain-guided modes in IAG waveguides. For comparison, with a similar approach it could be shown without much effort that $w_r \approx \sqrt{\Delta N}$ for index-guided modes, indicating the field confinement is determined exclusively by the index contrast between core and cladding, irrespective of gain saturation. Our study shows that the modal confinement in IAG waveguides is fundamentally different from that in index-guided waveguides. For IAG waveguides, the modal confinement is intrinsically related to the modal gain and is self-limited: as gain saturates, the net gain approaches a limiting value just enough to compensate for the propagation loss, rendering a zero modal gain and the field becomes cut-off. Even though the field cannot be normalized, the core power is finite and the field remains stable. Equation (3.29) also indicates that the ratio g_m/w_r increases with stronger index antiguiding, which is consistent with the increasing offset in Figure 3-6. This explains, for large IAG waveguides, why the cladding field amplitude appears very flat throughout the propagation since its initial w_r is already very small due to its large $-\Delta N$.

3.2.5 Output intensity and optimized length

Equation (3.27) provides a good description of the power or intensity evolution in the core of IAG waveguides. By expressing the integration constant explicitly, Eq. (3.27) could be re-written as

$$z = \frac{1}{(\eta-1)\alpha} \left[\frac{(1+2\eta)}{2\sqrt{(1+8\eta)}} \log \left[\frac{(R_{sat}+1+R_{out})(R_{sat}-R_{in})}{(R_{sat}+1+R_{in})(R_{sat}-R_{out})} \right] + \ln \left(\frac{R_{out}-1}{R_{in}-1} \right) + \left(\frac{1}{2} - \eta \right) \ln \left(\frac{2\eta - R_{out}(R_{out}+1)}{2\eta - R_{in}(R_{in}+1)} \right) \right], \quad (3.30)$$

where $R_{out} = \sqrt{1+2I'_{out}}$ and $R_{in} = \sqrt{1+2I'_{in}}$ are the output and input R parameters, respectively. The first term in the above equation could be shown to be small compared to other terms and may be neglected. Equation (3.30) could be simplified, by defining a normalized length $z' = \alpha z$, as

$$z' \approx (\eta-1)^{-1} \left[\ln \left(\frac{R_{out}-1}{R_{in}-1} \right) + \left(\frac{1}{2} - \eta \right) \ln \left(\frac{2\eta - R_{out}(R_{out}+1)}{2\eta - R_{in}(R_{in}+1)} \right) \right]. \quad (3.31)$$

Equation (3.31) indicates that the normalized propagation distance is determined exclusively by the ratio η , the input and output normalized core intensities I'_{in} , I'_{out} . If we define the output normalized intensity I'_{out} to be 90% of the limiting intensity, *i.e.*, $I'_{out} = 90\% I'_{lim}$, the corresponding normalized output length z'_{out} could be calculated using Eq. (3.31). Figure 3-7 shows z'_{out} and its corresponding I'_{out} as a function of η for different values of input normalized intensity I'_{in} . Several features are notable. Firstly, the output intensity scales nearly linearly over a large range of the ratio η . Secondly, the output length z'_{out} is shorter for larger input intensity I'_{in} , which is consistent with the fact that saturation

takes place faster for larger input power than for lower power. Thirdly, for input intensity $I'_{in} < 2$, z'_{out} diverges very fast for $\eta < 5$ and is a strong function of input intensity I'_{in} , whereas for $\eta > 10$ it becomes a smooth function with a limiting value between 2 and 3. This suggests that it is advantageous to design IAG planar waveguide amplifiers with larger η to be less sensitive to the variation in the input condition. In particular, there exists a critical input intensity $I'_{critical} = 1$ near which the output distance z'_{out} becomes nearly constant over a very wide range of η . Above (below) this critical intensity, z'_{out} decays (rises) monotonically with increasing η . This indicates an interesting design configuration where the optimum length of the waveguides is nearly independent of the gain and therefore pumping condition. Also we would like to point out that Eq. (3.31) is similar in form to Eq. (5) in Rigrod's plane-wave analysis of gain saturation and output power of lasers [82], and is expected to be useful in designing IAG waveguide amplifiers.

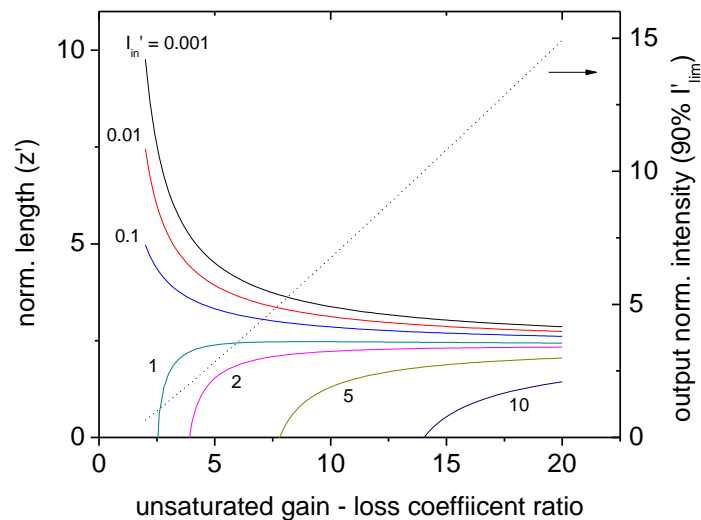


Figure 3-7 Normalized output length (solid colors, referred to the left axis) and output core intensity (dash black, referred to the right axis) as a function of the ratio of unsaturated gain coefficient to the loss coefficient, for different input intensities [24].

3.3 Index-antiguided planar waveguide lasers with uniform side pumping

Previous sections are investigating the characteristics of IAG planar waveguide amplifiers, including the effect of index-antiguiding on the field and power evolution, the amplifier model for the power evolution, and the optimized length for the amplifier. This section investigates the output power characteristics of fundamentally single mode (assume no HOMs) in uniformly side-pumped IAG slab lasers. The amplifier model in the previous section will be used to construct a bi-directional oscillator model. Based on the oscillator model, maximum extraction efficiency and corresponding optimum output coupling are determined for various values of unsaturated gain and loss per pass. A method is proposed to determine the intrinsic laser parameters from output power measurements.

The oscillator model could be derived as follows. Eq. (3.22) has been shown to be useful for finding the amplification and saturation of the propagating fundamental mode in a homogeneously-broadened (uniformly side-pumped) IAG planar waveguide amplifier. To generalize this one-directional amplifier equation to a bi-directional laser oscillator with the cavity extending from $z = 0$ to $z = L$, we modify only the form of the saturation factor to include saturation by both the forward and backward propagating waves. The forward and backward propagating intensities in a homogeneously-broadened IAG waveguide oscillator are thus governed by the following set of two coupled first-order nonlinear ordinary differential equations

$$\frac{dI_c'^+}{dz} = g_0 I_c'^+ \left\{ \frac{1}{I_c'^+ + I_c'^-} \left[1 - \frac{1}{[1 + 2(I_c'^+ + I_c'^-)]^{1/2}} \right] \right\} - \alpha I_c'^+, \quad (3.32)$$

$$\frac{dI_c'^-}{dz} = -g_0 I_c'^+ \left\{ \frac{1}{I_c'^+ + I_c'^-} \left[1 - \frac{1}{[1 + 2(I_c'^+ + I_c'^-)]^{1/2}} \right] \right\} + \alpha I_c'^-. \quad (3.33)$$

which subject to the boundary conditions imposed by the reflections at the oscillator ends

$$I_c'^+(0) = R_l I_c'^-(0), I_c'^-(L) = R_r I_c'^+(L). \quad (3.34)$$

where R_l and R_r are the mirror reflections at the left-hand ($z = 0$) and the right-hand ($z = L$) ends of the laser, respectively, and the plus and minus superscripts refer to the fields propagating toward the right and left ends respectively. It is seen from Eqs. (3.32) and (3.33) that the saturation equations for an IAG bi-directional laser are more complicated than the corresponding uniform-plane-wave results. On the other hand, for small values of the saturating intensities, the saturation factors in Eqs. (3.32) and (3.33) reduce to unity, and in this limit the saturation equations may be approximated by the plane-wave forms for an unsaturated laser

$$\frac{dI_c'^{\pm}(z)}{dz} = \pm(g_0 - \alpha) I_c'^{\pm}(z). \quad (3.35)$$

At threshold, Eq. (3.35) could be integrated subject to the boundary conditions at the laser mirrors to obtain the familiar result for the threshold gain g_{th} :

$$g_{th} = \alpha - \frac{1}{2L} \ln(R_l R_r). \quad (3.36)$$

For arbitrary levels of saturation, one has to solve Eqs. (3.32) - (3.34) self-consistently.

Notice that if the left-hand side of Eq. (3.32) is divided by $I_c'^+(z)$ and the left-hand side of Eq. (3.33) is divided by $I_c'^-(z)$, then the right-hand sides of these equations differ from each other only by a minus sign. The solution of this equation is known as the first integral:

$$I_c'^+(z) I_c'^-(z) = c. \quad (3.37)$$

where c is a constant to be determined, indicating that the product of the right and left propagating intensities is a constant over the length of the oscillator. With the boundary conditions given in Eq. (3.34), the left propagating intensities could be eliminated in Eq. (3.37), and the result could be written as

$$c = \frac{1}{R_l} \left(I_c'^+(0) \right)^2 = R_r \left(I_c'^+(L) \right)^2. \quad (3.38)$$

Substitute Eq. (3.37) into Eq. (3.32) to yield

$$\frac{dI_c'^+}{dz} = g_0 I_c'^+ \left\{ \frac{1}{I_c'^+ + \frac{c}{I_c'^+}} \left[1 - \frac{1}{\left[1 + 2 \left(I_c'^+ + \frac{c}{I_c'^+} \right) \right]^{1/2}} \right] \right\} - \alpha I_c'^+. \quad (3.39)$$

Equations (3.38) and (3.39) provide a complete set for solving the intensities of the forward and backward propagating waves anywhere inside the homogeneously broadened IAG-waveguide oscillators. Equation (3.39) is considerably more complicated than its plane-wave counterpart [84, 85], but could be solved numerically. For a common laser configuration where $R_l = 1$ at $z = 0$ (perfectly reflecting), the output normalized intensity I' outside of the output coupler could be calculated according to $I' = (1 - R_r) I_c'^+(L)$. From this result the extraction efficiency, which is one of the most important performance metrics of lasers, could be obtained by [85]

$$\eta = \frac{I'}{g_0 L}. \quad (3.40)$$

The denominator $g_0 L$ is the unsaturated gain per pass and represents the maximum normalized optical intensity available from the population inversion as a result of pumping.

Such a maximum value could be obtained in a plane-wave laser resonator exhibiting no distributed loss and nearly 100% output coupler reflectance [85].

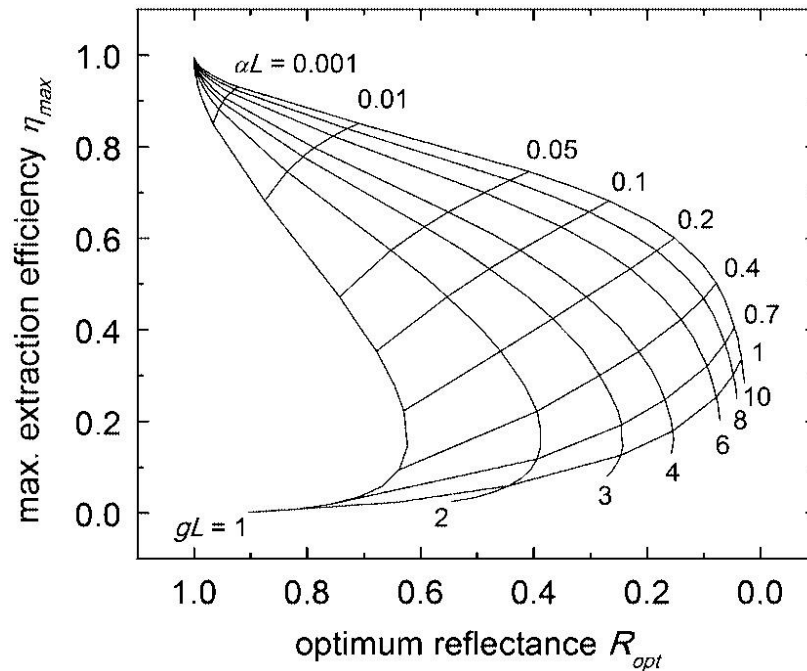


Figure 3-8 Maximum extraction efficiency versus optimum output coupler reflectance of homogeneously broadened IAG slab lasers for various values of g_0L and αL [25].

The theoretical model we have developed could be used to design and optimize IAG waveguide lasers. For this purpose it is convenient to solve Eq. (3.39) in terms of unsaturated gain per pass g_0L and loss per pass αL . For a given set of g_0L and αL , there exists an optimized output coupler reflectance R_{opt} that results in a maximum extraction efficiency η_{max} . Figure 3-8 shows the η_{max} versus its corresponding R_{opt} for various values of g_0L and αL . The optimum parameters for a given laser configuration are represented by the intersecting point of the two curves with the corresponding values of g_0L and αL . Very high extraction efficiency is only attainable with very low loss and nearly 100% output coupler reflectance. As loss increases, η_{max} decreases significantly. Figure 3-8 indicates that high gain and low loss are desirable for IAG oscillators because they lead to not only

higher η_{max} , but also more robust laser operation as η_{max} becomes less sensitive to variation of loss and mirror reflectance.

The above trend is qualitatively similar to that of a plane-wave oscillator [85] and one might be tempted to use the simpler plane-wave saturation model to design IAG oscillators. To compare their performance, we consider a plane-wave oscillator with a finite aperture equal to that of the IAG oscillator. Figure 3-9 shows the relative efficiency η_r , defined by the ratio of η_{max} of an IAG oscillator to the corresponding η_{max} of a plane-wave oscillator, as a function of g_0L between $g_{th}L$ to 10 for various values of αL . Note that η_r is always less than unity. Physically, this is due to the cosine-shaped mode field of the IAG slab waveguide, which leads to non-uniform gain saturation along the transverse dimension, whereas a plane-wave mode field saturates uniformly across the entire aperture. This, however, does not imply that an IAG oscillator operated in the fundamental mode is less efficient, as a plane-wave oscillator with a mode field filling a finite aperture cannot be realized in single-mode operation. Figure 3-9 shows that all curves have similar trends: η_r is low and rises sharply right above the threshold, after which it increases smoothly as gain increases. In addition, lower loss leads to higher η_r . These trends could be understood qualitatively by noting that, as gain increases or loss decreases, the transverse gain in the IAG oscillator becomes more uniformly saturated across the aperture, leading to higher η_r . In the theoretical limit of no loss, i.e., distributed loss = 0 and nearly 100% mirror reflectance where the IAG oscillator is nearly fully saturated transversely, η_{max} of an IAG oscillator approaches 100% (see Figure 3-8), which is comparable to that of a plane-wave oscillator [85]. Figure 3-9 shows that the prediction from a plane-wave saturation model is

too optimistic and is strongly dependent on gain or loss. Therefore, Eq. (3.39) will provide better results when designing and analyzing IAG oscillators.

Experimental determination of the three intrinsic laser parameters g_0 , α , and I_s would also be useful. Assume the slab laser has a mode size l along the unbounded dimension, which could be defined by the width of the optical or electrical pumping. The power extracted from a homogeneously broadened IAG slab laser is then

$$P = I_s \cdot d \cdot l \cdot I'(g_0, \alpha, R), \quad (3.41)$$

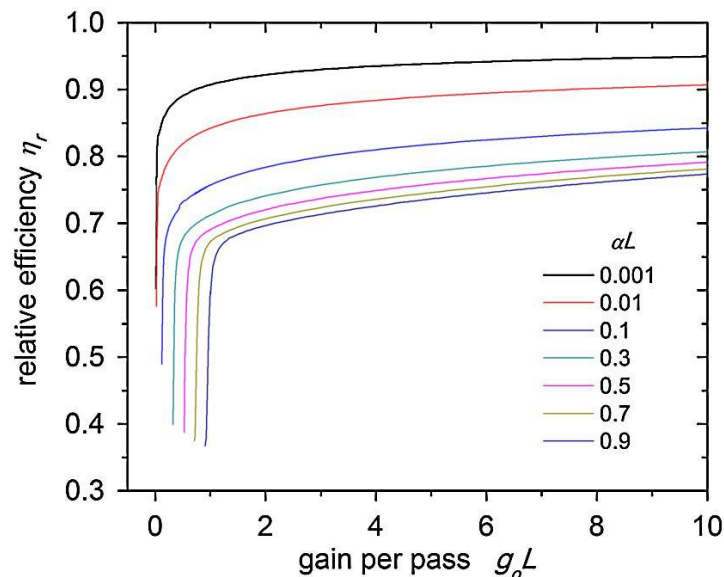


Figure 3-9 Dependence of the ratio η_r of η_{max} of IAG slab oscillators to that of plane-wave oscillators on g_0L for different αL [25].

The above equation has three unknowns (g_0 , α , I_s) if the mirror reflectance R is known and therefore requires three measurements to obtain its solution. Let the mirror reflectance and its corresponding output power of each measurement i be R_i and P_i , respectively, for $i = 1$ to 3. For each R_i , Eq. (3.41) indicates

$$\frac{I'_i(g_0, \alpha)}{P} = (I_s \cdot d \cdot l)^{-1}, \quad i = 1 \text{ to } 3. \quad (3.42)$$

For plane-wave oscillators, the solution to Eq. (3.42) could be obtained analytically [85], whereas for IAG oscillators this solution has to be obtained numerically. One potential approach is to define a function $z(x, y) = I'(x, y) / P$, where x and y are variables of gain and loss coefficients, respectively. For each i , z_i represents a curved surface in the three-dimensional space of (x, y, z) . These three surfaces could be obtained numerically by solving Eqs. (3.38) and (3.39) for each of the three pairs of R_i and P_i . Since the laser intrinsic parameters satisfy the three equations in Eq. (3.42) simultaneously, they could be obtained from the intersection point of the three curved surfaces z_i , whose coordinates are $(g_0, \alpha, (I_s \cdot d \cdot l)^{-1})$.

3.4 Transverse mode competition in uniformly side-pumped index-antiguided slab lasers

In the previous section, we have comprehensively analyzed the output efficiency of IAG planar waveguide lasers. However, the previous analysis only considers fundamentally single mode and does not include HOMs. As the robustness of single-mode operation is also significant to high-power lasers. This section will focus on the comprehensive analysis of single mode capability by considering transverse mode competition in uniformly side-pumped IAG slab lasers.

3.4.1 Introduction

It is well known that the output of a laser depends on many parameters in the resonator, such as pumping level and distribution, internal loss, mirror curvatures, output coupling, and cavity length, etc. [84, 85]. A comprehensive study of laser resonators is therefore essential for understanding these limitations and optimizing their performance. This is especially important for high-power lasers where large mode area (LMA) with

robust single fundamental mode is highly desired for high-brightness operation [86, 87]. These LMA lasers are mostly multimoded (MM) and require some level of mode discrimination to achieve single fundamental mode operation. Among various means to achieve this goal [76, 77, 87-89], index antiguiding is a relatively simple approach, where the negative index step between the core and the cladding imposes higher loss for higher order modes. Robust single fundamental mode oscillation has been reported both in IAG fibers with diameter up to 400 μm [13] and IAG planar waveguides with 200 μm core width [90]. In the previous section we have conducted the first theoretical analysis of output characteristics of fundamentally single-moded (i.e., HOMs can never oscillate) planar IAG lasers with arbitrary single-pass gain, single-pass internal loss and output coupling. However, recent observation of HOM oscillation in a 400 μm -core planar IAG laser [20] (as shown in Figure 3-10) indicates the necessity to include transverse mode competition due to transverse spatial hole burning [26] in such MM waveguide lasers. Although transverse mode competition in MM waveguide lasers has been investigated [91-94], these studies were conducted for specific values or narrow range of gain, loss, and output coupling. A comprehensive study of output characteristics in MM waveguide lasers, not only for IAG but also for LMA waveguide lasers in general, is still lacking. In this work, we conduct comprehensive analysis of output characteristics of single fundamental mode in planar multimoded IAG lasers with arbitrary gain and loss. We report a simple and efficient quasi-analytical method to calculate the threshold gain of the 1st HOM, which is very beneficial to this comprehensive study. We study numerically the extraction efficiency and optimal extraction conditions of the single fundamental mode (oscillation of only FM in a MM laser) for various combinations of single-pass gains and losses. We

present an analytic theory that predicts the absolute maximal extraction efficiency to be suppressed to 66.7% which is in excellent agreement with numerical modeling.

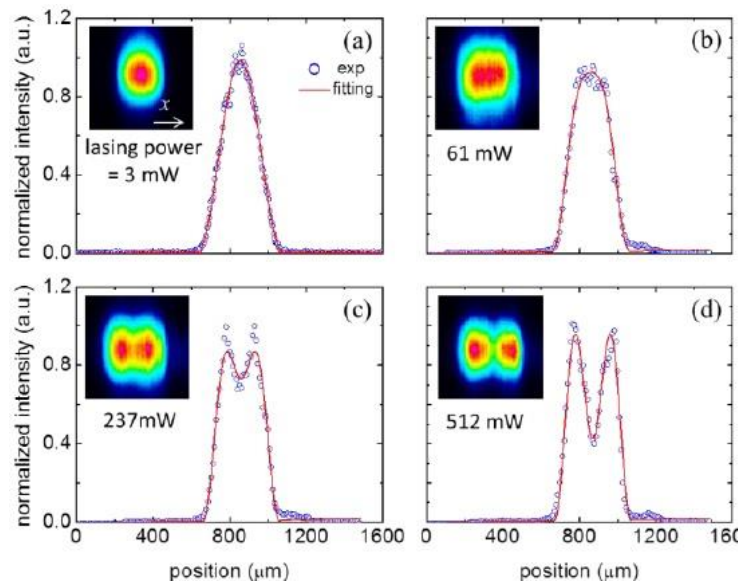


Figure 3-10 Near-field mode profiles at different lasing powers of (a) 3 mW, (b) 61 mW, (c) 237 mW and (d) 512 mW in a 400- μm IAG slab laser, showing clear HOM oscillation [20].

3.4.2 Oscillator model

We consider a generic planar IAG waveguide with a core width d and a length L , sandwiched between two flat mirrors with reflections R_l and R_r at the left-hand ($z = 0$) and the right-hand ($z = L$) ends of the resonator, respectively. The modal loss coefficient of the n^{th} mode is determined by the core width and the refractive indexes of the core and the cladding, and scales as square of the mode order n [20]. For simplicity, we assume the FM and HOM oscillate at the same frequency with a uniform small-signal gain coefficient in the core region. Previously in Section 3.3 we have developed a model to calculate the propagating intensities in a uniformly side-pumped planar IAG waveguide laser based on a zero-field approximation. In the situation of transverse mode competition, the forward-propagating average normalized intensities (I_n^{*+}) of the fundamental ($n=1$) and the first

higher-order mode (n=2) are governed by the following set of two coupled first-order nonlinear ordinary differential equations [17]

$$\frac{dI_n^+}{dz} = g_0 I_n^+ \int_{-d/2}^{d/2} \frac{f_n(x)}{[1 + d \sum_{i=1}^2 f_i(x)(I_i^+ + c_i / I_i^+)]} dx - \alpha_n I_n^+ \quad n = 1, 2 \quad (3.43)$$

where $c_n = [I_n^+(0)]^2 / R_l = R_r [I_n^+(L)]^2$ are mode-specific constants, and $f_1(x) = 2\cos^2(\pi x/d)/d$ and $f_2(x) = 2\sin^2(2\pi x/d)/d$ are the normalized intensity profiles across the waveguide core width satisfying $\int_{-d/2}^{d/2} f_n(x) dx = 1$. For arbitrary level of saturation, Eq.(3.43) needs to be solved self consistently to yield $I_n^+(z)$, from which a multitude of laser output parameters, such as threshold gain, slope efficiency, extraction efficiency, output power, etc., could be derived for individual modes.

3.4.3 The gain oscillation threshold of the first higher-order mode

It is important to firstly know the gain oscillation threshold of the 1st HOM (g_2^{th}). As the focus of this section is on the output characteristics of the single fundamental mode, there is no need to calculate I_2^+ if we already know its threshold g_2^{th} . This threshold could be calculated numerically by solving the two integro-differential equations in Eq. (3.43). However, it is computationally intensive to solve these two coupled equations. Below we present a simple method to obtain g_2^{th} quasi-analytically.

When the unsaturated gain coefficient g_0 equals threshold gain of the fundamental mode g_1^{th} , the FM just starts to oscillate ($I_1^+ \approx 0$) while I_2^+ is zero. At steady state where the round-trip gain equals the round-trip loss for the FM, Eq. (3.43) could be integrated to yield the well-known condition for g_1^{th} :

$$g_1^{th} L = \alpha_1 L - \frac{1}{2} \ln R_l R_r. \quad (3.44)$$

At intermediate gain $g_1^{th} < g_0 < g_2^{th}$, the FM oscillates and I_1^+ is governed by a single integro-differential equation:

$$\frac{dI_1^+}{dz} = g_0 I_1^+ \int_{-d/2}^{d/2} \frac{f_1(x)}{[1 + df_1(x)(I_1^+ + c_1 / I_1^+)]} dx - \alpha_1 I_1^+. \quad (3.45)$$

which is identical to Eq. (3.39) (after substituting $f_1(x)$), and could be solved much more efficiently than Eq. (3.43). At the same time, the 1st HOM is below the threshold and integrating Eq. (3.43) yields

$$g_0 \int_0^L \left(\int_{-d/2}^{d/2} \frac{f_2(x)}{[1 + df_1(x)(I_1^+ + I_1^-)]} dx \right) dz < \alpha_2 L - \frac{1}{2} \ln R_l R_r. \quad (3.46)$$

Finally, at $g_0 = g_2^{th}$, the HOM starts to oscillate ($I_2^+ \approx 0$) and Eq. (3.46) becomes

$$g_2^{th} \int_0^L \left(\int_{-d/2}^{d/2} \frac{f_2(x)}{[1 + df_1(x)(I_1^+ + I_1^-)]} dx \right) dz = \alpha_2 L - \frac{1}{2} \ln R_l R_r. \quad (3.47)$$

Equation (3.47) defines g_2^{th} , which could be determined fairly quickly by gradually increasing g_0 in Eq. (3.45) to obtain I_1^+ until a transition from Eq. (3.46) to Eq. (3.47) is obtained. We have applied this simplified method to Figure 1 and 3 of Ref. [20] and obtained excellent agreement.

3.4.4 Regions of single-fundamental-mode operation

Equations (3.44)-(3.47) are applied to study the oscillation threshold characteristics of IAG planar waveguide lasers. Consider a general laser configuration where $R_l = 1$ and $R_r = R_{oc}$ (the reflectance of the output coupler). With this notation, the output coupling loss is defined as $T = 1 - R_{oc}$, which approximates $-\ln R_{oc}$ when R_{oc} is close to unity. Figure 3-11(a)

shows the contour plot of the theoretical single-pass threshold gain $g_1^{th}L$ of the FM as a function of single-pass loss α_1L (logarithmic scale) and output coupler R_{oc} (linear scale).

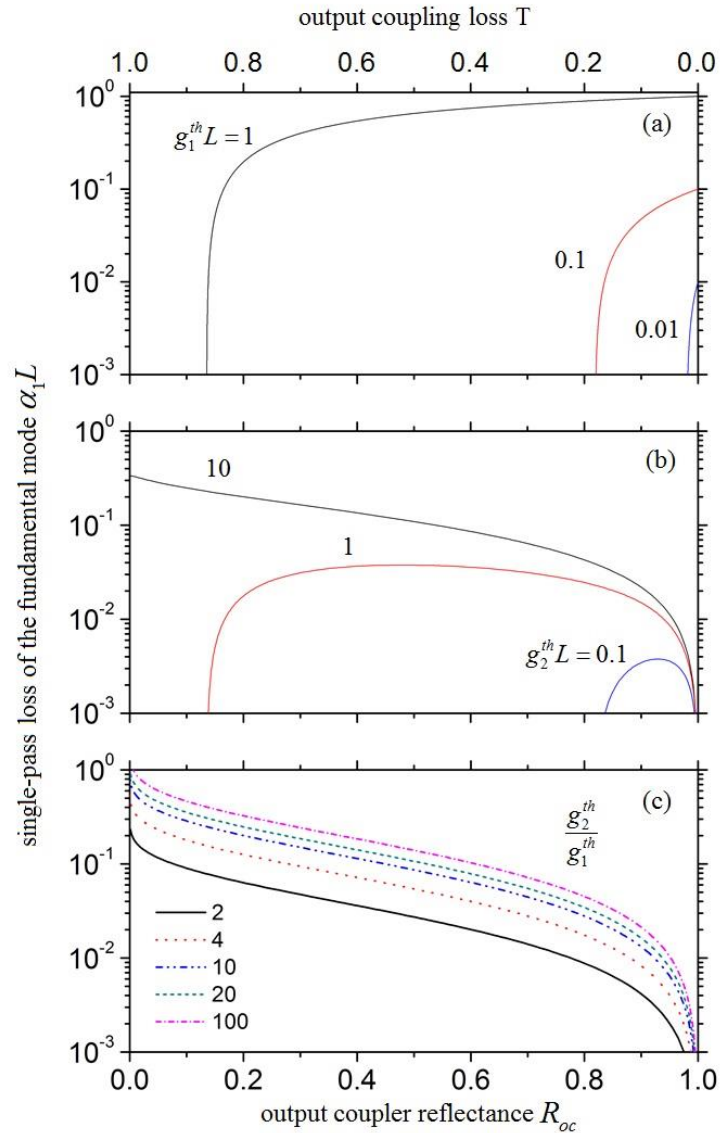


Figure 3-11 Contour plots of (a) single-pass threshold gain $g_1^{th}L$ of the fundamental mode, (b) single-pass threshold gain $g_2^{th}L$ of the 1st HOM, and (c) threshold gain contrast g_2^{th} / g_1^{th} , as a function of single-pass loss α_1L of the fundamental mode (logarithmic scale) and output coupler R_{oc} (linear scale) [17], in uniformly side-pumped IAG slab lasers.

As is apparent from Eq. (3.44), $g_1^{th}L$ decreases monotonically with decreasing distributive loss α_1L and output coupling loss T (or increasing R_{oc}). Figure 3-11(b) shows

a similar plot for the threshold gain $g_2^{th}L$ of the 1st HOM. In the lower-left region where the output coupling loss T dominates the distributive loss α_1L , there is little modal discrimination between the FM and 1st HOM such that the 1st HOM oscillates immediately after FM lases. The gain saturation term in Eq. (3.47) is negligible and $g_2^{th}L$ follows the trend of $g_1^{th}L$. This situation is completely different in upper-right region of the figure where $\alpha_1L \gg T$ and gain saturation by the FM effectively suppresses HOM oscillation. We define a robustness parameter $\xi = g_2^{th} / g_1^{th}$ to reflect the robustness of single fundamental mode operation. As shown in Figure 3-11(c), to have large ξ and therefore robust single FM operation, one needs to work in the upper-right region where the discriminating IAG loss ($\propto \alpha_1L$) dominates the non-discriminating output coupling loss T such that gain saturation by the FM effectively suppresses HOM oscillation. It is worth to point out that not all the points along the contour work equally effective in laser optimization. As for the case of plane-wave oscillators, large internal loss significantly reduces lasers' extraction efficiency [95]. This topic is the subject of the following sections.

3.4.5 Extraction efficiency of single fundamental mode

One of the most important performance metrics of lasers is their extraction efficiency which is defined in Eq. (3.40) for uniformly side-pumped lasers. For multimoded lasers, the extraction efficiency for the n^{th} mode is $\eta_n = I_n^+(L)(1-R_{oc}) / g_0L$. For given gain and loss coefficients, η_n is typically a strong function of the output coupling, and maximal extraction efficiency η_n^{max} exists at some optimal output coupler R_{opt} . For high-brightness operation, one is particularly interested in the maximal extraction

efficiency η_{SM}^{\max} of the single fundamental mode, which is defined by $\eta_{SM}^{\max} = \text{maximal } \eta_1$ when $\eta_2 = 0$. In principle η_{SM}^{\max} could be calculated by solving Eq. (3.43) to take into account of the transverse mode competition explicitly. With the knowledge of g_2^{th} , however, we propose a simpler method to calculate it and illustrate its principle below by considering an IAG waveguide with $\alpha_1 L = 0.1$. Firstly we assume a fundamentally single-mode laser by setting $I_2^{++} = 0$ and solve Eq. (3.45) to obtain η_1 as a function of R_{oc} for selected $g_0 L$, as shown in Figure 3-12(a). For each $g_0 L$, η_1^{\max} occurs at the critical point where the derivative $\eta_1'(R_{opt})$ equals zero and this defines the optimal output coupler R_{opt} . The red dash-dot-dot in Figure 3-12(a) denotes the locus of η_1^{\max} and its corresponding R_{opt} for different gains. Next, we allow HOM to oscillate (*i.e.*, I_2^{++} can be non-zero) and identify single FM region in Figure 3-12(a). To do so, we calculate $g_1^{\text{th}} L$ and $g_2^{\text{th}} L$ as a function of R_{oc} for $\alpha_1 L = 0.1$, which is displayed in Figure 3-12(b). The regions below the $g_1^{\text{th}} L$ curve, between $g_1^{\text{th}} L$ and $g_2^{\text{th}} L$ curves, and above the $g_2^{\text{th}} L$ curve, represent no oscillation, FM only, and multimode oscillation, respectively. While the $g_1^{\text{th}} L$ curve is monotonic, the $g_2^{\text{th}} L$ curve has a local minimum at $g_0^{\text{th}} L = 2.654$, below which the oscillation is single FM for all R_{oc} . For each $g_0^{\text{th}} L > 2.654$, the $g_2^{\text{th}} L$ curve defines two R_{oc} values separating the single FM from MM operation. The $g_2^{\text{th}} L$ curve in Figure 3-12(b) could then be mapped into Figure 3-12(a) as the blue dash-dot curve, which also represents η_1 at the threshold of the 1st HOM. Finally, we could define η_{SM}^{\max} as follows, which is represented by black circles in Figure 3-12(a): Below the $g_2^{\text{th}} L$ curve the laser is single

fundamental mode so $\eta_{SM}^{\max} = \eta_1^{\max}$; above it the laser is MM and η_{SM}^{\max} follows the $g_2^{th}L$ curve, as HOM kicks in before the laser reaches to η_1^{\max} . These two segments intersect at $g_0L = 4.235$ which defines a sharp kink. Figure 3-12(a) clearly shows that, as a result of transverse mode competition, η_{SM}^{\max} is suppressed in regions of high gain and the corresponding optimal output coupler R_{opt} increases.

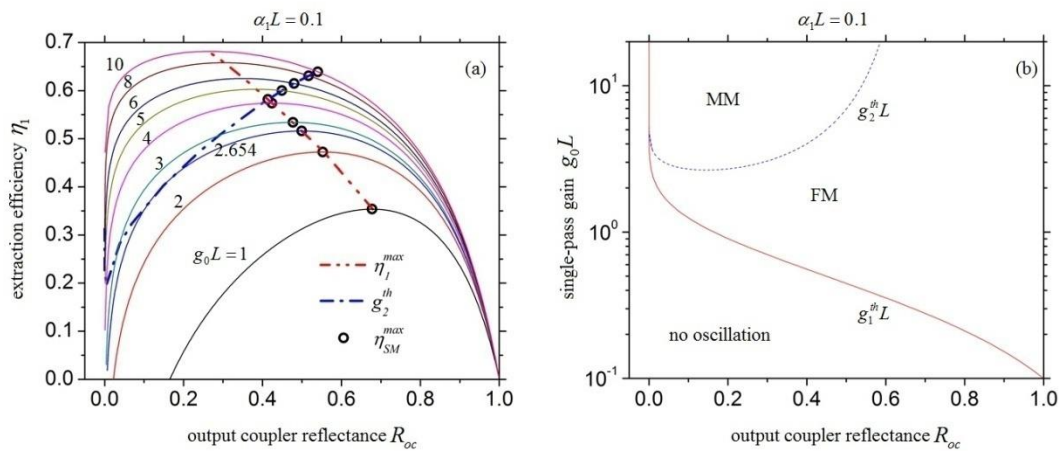


Figure 3-12 For $\alpha_1 L = 0.1$, (a) extraction efficiency of the fundamentally single mode vs. output coupling for selected fixed gains, and (b) threshold gain vs. output coupling for FM and 1st HOM in a MM IAG laser. In (a), red dash-dot-dot is the locus of maximal extraction efficiency of the FM, blue dash-dot is η_1 at the threshold of 1st HOM, and black circle is the maximal single-fundamental-mode extraction efficiency in a MM IAG laser [17].

Figure 3-12 (a) could be repeated to obtain η_{SM}^{\max} and R_{opt} for different values of $\alpha_1 L$. The result is summarized in Figure 3-13(a). For comparison, the same calculation for a fundamentally single-mode IAG laser is displayed in Figure 3-13(b). As shown, without the HOM competing with the FM, all curves of constant $g_0 L$ (solid line) or $\alpha_1 L$ (dash line) are smooth and η_1^{\max} approaches unity in the limit of low loss. With the HOM competing with the FM, the trend remains the same in high-loss regions while it is squeezed downwards in low-loss regions. The squeezing results in kinks in all curves of constant

gain or loss (notice that kinks in curves of very low gain or very high loss are not shown). Specifically, the dash curve with $\alpha_1 L = 0.1$ in Figure 3-13(a) is identical to the η_{SM}^{\max} curve in Figure 3-12(a). Figure 3-13 clearly indicates that η_{SM}^{\max} is suppressed and approaches an asymptotic value of 67%, which defines an absolute maximal extraction efficiency H_{SM}^{\max} of the laser under single-fundamental-mode operation (H stands for capital Greek letter η). The squeezing also makes η_{SM}^{\max} insensitive to (internal) distributive loss and (external) output coupling loss at high gain – a property that is also shared by plane-wave resonators [85].

The value of H_{SM}^{\max} could be derived analytically as follows. Referring to Figure 3-13(a), H_{SM}^{\max} equals η_{SM}^{\max} in the limit of low distributive loss, weak output coupling, and high gain. This point corresponds to the largest η_{SM}^{\max} in Figure 3-12(a), which occurs at the intersection of the $g_2^{\text{th}} L$ curve and the η_1 curve of the highest $g_0 L$. It therefore satisfies both Eq. (3.47) and

$$g_2^{\text{th}} \int_0^L \left(\int_{-d/2}^{d/2} \frac{f_1(x)}{[1 + df_1(x)(I_1^+ + I_1^-)]} dx \right) dz = \alpha_1 L - \frac{1}{2} \ln R_{oc}. \quad (3.48)$$

Here $R_l = 1$ and R_r is replaced by R_{oc} . Equation (3.48) states simply that round-trip gain equal to round-trip loss for the FM at g_2^{th} . Let $\alpha_2 = k\alpha_1$ where $k = 4$ for planar IAG waveguides. Multiplying Eq. (3.48) by k and subtracting Eq. (3.47) yields

$$g_2^{\text{th}} \int_0^L \int_{-d/2}^{d/2} \frac{kf_1(x) - f_2(x)}{[1 + df_1(x)(I_1^+ + I_1^-)]} dx dz = -\frac{(k-1)}{2} \ln R_{oc}. \quad (3.49)$$

At the limit of low loss $\alpha_1 L \rightarrow 0$ and weak coupling $R_{oc} \rightarrow 1$ where $I_1^+ \approx I_1^-$ and $-\ln R_{oc} \approx 1 - R_{oc}$, Eq. (3.49) is reduced

$$g_2^{th} L \int_{-d/2}^{d/2} \frac{kf_1(x) - f_2(x)}{[1 + df_1(x)2I_1^+]} dx \approx \frac{(k-1)}{2} (1 - R_{oc}). \quad (3.50)$$

Since the right-hand side of Eq. (3.50) is close to zero, we have $df_1(x)2I_1^+ \gg 1$ and Eq.

(3.50) becomes

$$\frac{g_2^{th} L}{2I_1^+} (k-2) = \frac{(k-1)}{2} (1 - R_{oc}). \quad (3.51)$$

The absolute maximal extraction efficiency H_{SM}^{\max} of single fundamental mode is therefore

$$H_{SM}^{\max} = \frac{I_1^+ (1 - R_{oc})}{g_2^{th} L} = \frac{k-2}{k-1}. \quad (3.52)$$

With $k = 4$ for planar IAG lasers, $H_{SM}^{\max} = 2/3 \sim 0.67$, which agrees well with the numerical result shown in Figure 3-13(a). It needs to be noted that the absolute maximal extraction efficiency is not only dependent on the loss ratio k , but also the ratio of modal profiles $f_2(x)/f_1(x)$, as shown in the left-hand side of Eq. (3.50).

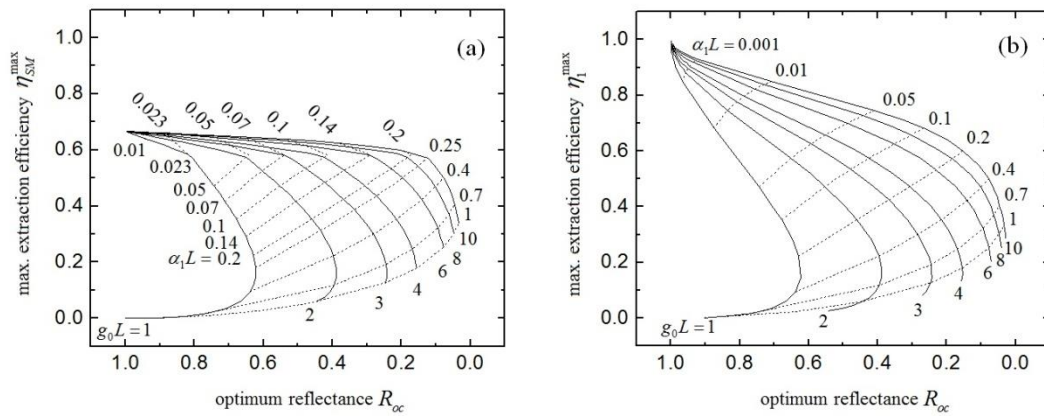


Figure 3-13 (a) Maximal extraction efficiency of the single fundamental mode in a multimoded IAG slab laser (η_{SM}^{\max}) and optimal output coupler reflectance R_{opt} , for various single-pass gains (solid lines) and distributive losses (dash lines). (b) Same as (a) except maximal extraction efficiency of a fundamentally single-moded laser (η_1^{\max}) [17].

Besides the unique feature that demonstrates a 2/3 maximal extraction efficiency for IAG slab lasers with transverse mode competition, another interesting feature from Figure 3-13 is where the kinks occur. Below are some derivations showing that the kink occurs at $\eta_{SM}^{\max} \approx 0.58$, $g_0 / \alpha_1 \approx 42$ and $-\ln R_{opt} / \alpha_1 L \approx 8.8$, under small output coupling condition (R_r is close to 1).

Since the kink points are the intersections of η_1^{\max} profiles (red dash-dot-dot) and $g_2^{\text{th}} L$ profiles (blue dash-dot), as shown in Figure 3-12(a). It has to satisfy Eq. (3.47) and another equation relating to η_1^{\max} . Below demonstrates an analytical derivation of η_1^{\max} at the condition of small output coupling. Let us start from Eqs. (3.32) and (3.33), under small coupling condition with R_r closed to 1, we could assume $I^+ \approx I^- \approx I$ and Eq. (3.32) is changed to

$$\frac{dI^+}{dz} = \left\{ g_0 \left(\frac{1}{2I} \left[1 - \frac{1}{\sqrt{1+4I}} \right] \right) - \alpha_1 \right\} I^+. \quad (3.53)$$

The solution of Eq. (3.53) is

$$\frac{I^+(L)}{I^+(0)} = \exp \left(\left\{ g_0 \left(\frac{1}{2I} \left[1 - \frac{1}{\sqrt{1+4I}} \right] \right) - \alpha_1 \right\} L \right). \quad (3.54)$$

where L is waveguide length. If we consider the left-hand reflection $R_l = 1$ and steady state condition, it is further derived from Eq. (3.54) that

$$g_0 L \frac{1}{2I} \left(1 - \frac{1}{\sqrt{1+4I}} \right) = \alpha_1 L - \frac{1}{2} \ln R_r. \quad (3.55)$$

The optical extraction efficiency is defined as

$$\eta_1 = \frac{I^+(1-R_r)}{g_0 L} \approx \frac{I(1-R_r)}{g_0 L}. \quad (3.56)$$

Substitute Eq. (3.55) into Eq. (3.56), the extraction efficiency could be analytically expressed as

$$\eta_1 = \frac{(1-R_r)}{4g_0L} \left[2g_0L / (\alpha_1L - \frac{1}{2} \ln R_r) - \frac{1 + \sqrt{1 + 8g_0L / (\alpha_1L - \frac{1}{2} \ln R_r)}}{2} \right] \quad (3.57)$$

$$\approx -\frac{\ln R_r}{4g_0L} \left[2g_0L / (\alpha_1L - \frac{1}{2} \ln R_r) - \frac{1 + \sqrt{1 + 8g_0L / (\alpha_1L - \frac{1}{2} \ln R_r)}}{2} \right].$$

The optimum output coupler R_{opt} could then be calculated by taking the derivative of Eq. (3.57) to R_r and set it to zero ($d\eta_1 / dR_r = 0$), that is

$$\left(2g_0L / (\alpha_1L - \frac{1}{2} \ln R_{opt}) - \frac{1 + \sqrt{1 + 8g_0L / (\alpha_1L - \frac{1}{2} \ln R_{opt})}}{2} \right) + \frac{g_0L \ln R_{opt}}{(\alpha_1L - \frac{1}{2} \ln R_{opt})^2} (1 - (1 + 8g_0L / (\alpha_1L - \frac{1}{2} \ln R_{opt}))^{-0.5}) = 0. \quad (3.58)$$

Now we could combine Eq. (3.58) and Eq. (3.47) to obtain the solution of the kink points. Here I would like to state that the solution of kink points satisfies a scaling law, which means that if $(\alpha_1L^*, g_0L^*, -\ln R_{opt}^*)$ is a solution, $(k\alpha_1L^*, kg_0L^*, -k \ln R_{opt}^*)$ is also a solution, where k is a random positive constant.

At first let us prove Eq. (3.58) satisfies the scaling law. It is simple to rewrite Eq. (3.58) as a function F_1

$$\begin{aligned}
F_1(\alpha_1 L, g_0 L, -\ln R_{opt}) &= \left(2 \frac{g_0 L}{\alpha_1 L} / \left(1 - \frac{1}{2} \frac{\ln R_{opt}}{\alpha_1 L}\right) - \frac{1 + \sqrt{1 + 8 \frac{g_0 L}{\alpha_1 L} / \left(1 - \frac{1}{2} \frac{\ln R_{opt}}{\alpha_1 L}\right)}}{2}\right) + \\
&\frac{g_0 L}{\alpha_1 L} \frac{\ln R_{opt}}{\alpha_1 L} \frac{1}{\left(1 - \frac{1}{2} \frac{\ln R_{opt}}{\alpha_1 L}\right)^2} \left(1 - \left(1 + 8 \frac{g_0 L}{\alpha_1 L} / \left(1 - \frac{1}{2} \frac{\ln R_{opt}}{\alpha_1 L}\right)\right)^{-0.5}\right) = 0.
\end{aligned} \tag{3.59}$$

Then it is straightforward to show that

$$F_1(k\alpha_1 L^*, kg_0 L^*, -k \ln R_{opt}^*) = F_1(\alpha_1 L^*, g_0 L^*, -\ln R_{opt}^*) = 0. \tag{3.60}$$

Therefore $(k\alpha_1 L^*, kg_0 L^*, -k \ln R_{opt}^*)$ is also a solution of the kink points.

The next step is to prove that Eq. (3.47) satisfies the scaling law. Rewrite Eq. (3.47)

as another function F_2

$$\begin{aligned}
F_2(\alpha_1 L, g_0 L, -\ln R_{opt}) &= \frac{g_0}{\alpha_2 L} \int_0^L \left(\int_{-d/2}^{d/2} \frac{f_2(x)}{[1 + df_1(x)(I_1^+ + I_1^-)]} dx \right) dz + \frac{1}{2} \frac{\ln R_r}{\alpha_2 L} - 1 \\
&= \frac{g_0 L}{4\alpha_1 L} \int_0^1 \left(\int_{-d/2}^{d/2} \frac{f_2(x)}{[1 + df_1(x)(I_1^+ + I_1^-)]} dx \right) dz' + \frac{1}{2} \frac{\ln R_r}{4\alpha_1 L} - 1 = 0.
\end{aligned} \tag{3.61}$$

Here in Eq. (3.61) we replace $z = Lz'$ and $\alpha_2 = 4\alpha_1$ (for planar IAG). Therefore it is obtained from Eq. (3.61) that

$$F_2(k\alpha_1 L^*, kg_0 L^*, -k \ln R_{opt}^*) = F_2(\alpha_1 L^*, g_0 L^*, -\ln R_{opt}^*) = 0. \tag{3.62}$$

and $(k\alpha_1 L^*, kg_0 L^*, -k \ln R_{opt}^*)$ is also a solution of the kink points.

Now since we have shown that the solution of the kink points satisfies the scaling law under weak coupling condition, it is only necessary to calculate one solution and derive the others. Table 3-1 shows the solution of the kink points. It is seen that the scaling law is satisfied for weak coupling, with a nearly fixed g_0 / α_1 value of ~ 42 and $-\ln R_{opt} / \alpha_1 L$ value of ~ 8.8 . Moreover, the optimum extraction efficiencies of the single mode at the

kink points are nearly the same, with a value of ~ 0.58 . In addition, the scaling law is not well satisfied when the coupling is strong (small R_r).

Table 3-1 Solution of the kink points that satisfy the scaling law

$\alpha_1 L$	$g_0 L$	R_{opt}	η_{SM}^{\max}	g_0/α_1	$-\ln(R_{opt})/\alpha_1 L$
0.01	0.42	0.92	0.58	42.36	8.82
0.02	0.97	0.82	0.58	42.31	8.83
0.05	2.12	0.64	0.58	42.31	8.83
0.07	2.96	0.54	0.58	42.32	8.83
0.10	4.24	0.41	0.58	42.35	8.83
0.14	5.95	0.29	0.58	42.48	8.81
0.20	8.59	0.17	0.58	42.94	8.77

3.5 Summary

This chapter provides the theory of IAG planar waveguide lasers. It starts from the waveguide properties, showing that IAG planar waveguides will intrinsically introduce a waveguide loss ratio of 4 between the FM and 1st HOM for large $-\Delta N$. This differential loss is believed to favor the large single-mode operation and high power capability. After that, an amplifier model for uniformly side-pumped IAG planar waveguides is given, which is shown to have a simple analytical solution for the power evolution of fundamental mode. The gain-guided mode has modal confinement proportional to the modal gain, and single-transverse-mode propagation is very robust in such waveguides. In addition, it is seen that for strong IAG (large $-\Delta N$), saturation occurs at long distance with much larger limiting intensities, and the mode shape remains nearly identical during the propagation. Based on the amplifier model, the laser model of fundamentally single mode in uniformly

side-pumped IAG slab lasers is also provided. Maximum extraction efficiency of fundamentally single mode and corresponding optimum output coupling are calculated for various values of unsaturated gains and losses per pass, showing similar property as for plane-wave oscillators. Very high extraction efficiency is only achievable with very low loss and nearly 100% output coupler reflectance, with the value approaching to unity at the limit. The capability of single-mode operation in IAG slab lasers is also comprehensively investigated. The oscillator model including transverse mode competition is proposed for uniformly side-pumped IAG slab lasers. Based on the oscillator model, a simple quasi-analytical method is proposed to calculate the gain oscillation thresholds of HOMs. It is shown that single-mode operation is favored for large distributive loss of FM and small output coupling loss (or large output coupler reflectivity). The output efficiency of the single fundamental mode (only FM oscillates in MM lasers) is numerically investigated under the condition of transverse mode competition and compared to the result without considering transverse mode competition. It is shown that due to transverse mode competition the maximal extraction efficiency is suppressed when the small signal gain is large and distributive loss is small, or roughly at $g_0/\alpha_1 > 42$. At the limit of $\alpha_1 L \rightarrow 0$ and $R_{oc} \rightarrow 1$, the maximal extraction efficiency asymptotically approaches the maximal value of 66.7%, or more generally, $(k-2/k-1)$ with k the distributive loss ratio between the 1st HOM and FM (for IAG slab waveguides, $k = 4$). In fact, this absolute maximal value is shown to be related to both the ratio of modal loss and the ratio of HOM and FM profiles.

CHAPTER 4 OUTPUT CHARACTERISTICS OF INDEX-ANTIGUIDED FIBER LASERS IN FUNDAMENTALLY SINGLE MODE REGIME

Previous chapter focuses on the theory of IAG planar waveguide lasers. The property of IAG waveguide loss, output characteristics of fundamentally single mode and transverse mode competition in uniformly side-pumped IAG slab lasers are comprehensively analyzed. This chapter, along with the following chapters will focus on the property of IAG fiber lasers.

The structure of this chapter is as follows. Section 4.1 will provide the background of waveguide properties in IAG fibers, showing a loss ratio of 2.54 between FM and first HOM for large index antiguiding, which differs from IAG planar waveguides with a loss ratio of 4. Section 4.2 discusses the general pumping schemes for IAG fiber lasers. Both side and end pumping techniques are investigated. Moreover, the efficiency of end pumping is further investigated and compared between core and cladding pumping. Some improvement methods on end pumping scheme are also analyzed. Section 4.3 will investigate the output characteristics of fundamentally single mode in uniformly side-pumped IAG fiber lasers. Section 4.4 will investigate the output characteristics of fundamentally single mode in core-pumped IAG fiber lasers. The oscillator model will be provided and the parameters affecting the output efficiency will be carefully analyzed. The reason for the low output efficiency in the published experiment [21] will be indicated. Based on the analysis, a design guideline to yield high output efficiency will be provided for core-pumped IAG fiber lasers.

4.1 Modal characteristics of index-antiguided fiber lasers

In IAG fiber waveguides, the modes in z direction could be expressed as

$$E_z = \begin{cases} J_m(\tilde{U}r/a)e^{im\phi}e^{-i\tilde{\beta}z}, & (r \leq a) \\ [J_m(\tilde{U})/K_m(\tilde{W})]K_m(\tilde{W}r/a)e^{im\phi}e^{-i\tilde{\beta}z}. & (r > a) \end{cases} \quad (4.1)$$

with

$$\begin{aligned} \tilde{W}^2 &= \tilde{U}^2 + \tilde{V}^2, \\ \tilde{\beta}^2 &= (n_{core}k_0a)^2 - \tilde{U}^2 = k_0^2a^2(n_0 + \Delta n + i\frac{g_0}{2k_0})^2 - \tilde{U}^2. \end{aligned} \quad (4.2)$$

here J_m and K_m are the m^{th} -order Bessel J and K functions, respectively. $\tilde{\beta}$ is the complex propagation constant. The characteristic equations could be obtained after applying the boundary conditions - the continuity of tangential fields E and H . For special case of LP_{01} and LP_{11} modes, the expressions are

$$\begin{aligned} \frac{\tilde{U}J_1(\tilde{U})}{J_0(\tilde{U})} &= \frac{\tilde{W}K_1(\tilde{W})}{K_0(\tilde{W})}, & LP_{01} \\ \frac{\tilde{U}J_0(\tilde{U})}{J_1(\tilde{U})} &= -\frac{\tilde{W}K_0(\tilde{W})}{K_1(\tilde{W})}, & LP_{11} \end{aligned} \quad (4.3)$$

The above equation could be solved to show the propagation regions for different modes in IAG fibers. Similar to Figure 3-2(a) for planar waveguides, Figure 4-1(a) shows the gain thresholds of LP_{01} (solid blue) and LP_{11} (solid red) modes in IAG fiber waveguides. The single-mode operation requires G staying within G_1^{th} and G_2^{th} . Like planar waveguides, at large $-\Delta N$ the threshold gains could be simply estimated as

$$\begin{aligned} G_{1_est}^{\text{th}} &= j_{01}^2 \sqrt{-4/\Delta N}, \\ G_{2_est}^{\text{th}} &= j_{11}^2 \sqrt{-4/\Delta N}. \end{aligned} \quad (4.4)$$

where $j_{01} = 2.405$ and $j_{11} = 3.832$.

Figure 4-1(b) plots the gain threshold ratio between LP₀₁ and LP₁₁. It is seen that at larger $-\Delta N$, the gain threshold ratio is

$$G_2^{th} / G_1^{th} \approx (j_{11} / j_{01})^2 = 2.54. \quad \text{IAG fibers} \quad (4.5)$$

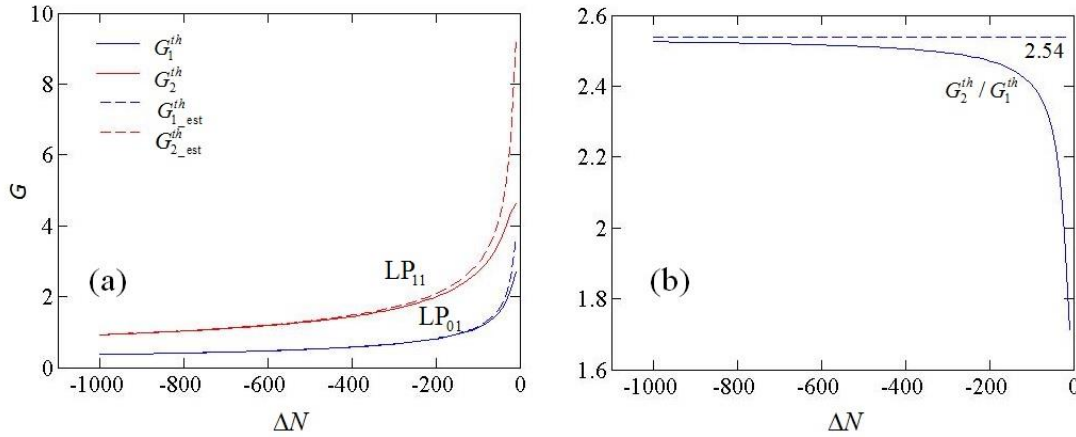


Figure 4-1 (a) Gain thresholds of LP₀₁ (solid blue) and LP₁₁ (solid red) in IAG fiber waveguides, the dashed lines are the corresponding estimated gain threshold values from Eq. (4.4). (b) The ratio of gain threshold G_2^{th} / G_1^{th} between FM and the 1st HOM, showing an asymptotic value of 2.54 at large $-\Delta N$.

The modal loss in IAG fiber waveguide is very close to the gain threshold calculated in Figure 4-1. At large $-\Delta N$, the modal losses in IAG fiber waveguides could be estimated as

$$\alpha_1 \approx \frac{2j_{01}^2}{k_0 a^2 n_0 \sqrt{-\Delta N}}, \quad \text{IAG fibers} \quad (4.6)$$

$$\alpha_2 \approx \frac{2j_{11}^2}{k_0 a^2 n_0 \sqrt{-\Delta N}} = 2.54\alpha_1.$$

where α_1 and α_2 are the losses of FM and 1st HOM, respectively. It is seen that the loss ratio between FM and 1st HOM is 2.54 in IAG fiber waveguides, compared to 4 in IAG planar waveguides.

4.2 Pumping schemes

High-efficiency pumping is significant to high-power fiber lasers. This section discusses the possibility of the most two common optically pumping schemes – side and end pumping, for IAG fiber lasers.

4.2.1 Side pumping

Side pumping is a general optically pumping technique, which is usually to pump a gain medium by coupling the pump light into the core in a perpendicular direction from the side. Figure 4-2 demonstrates a typical side pumping scheme for IAG fiber lasers. The large core of IAG waveguides will favor the side pumping as more pump light could be coupled into the large core. Moreover, most of the IAG waveguides have short lengths [19, 96] which make the side pumping technique applicable. The first demonstration of lasing in IAG fiber laser with side pumping scheme was in 2006 using a Xe flashlamp to pump a 100 μm -core, 10 cm long Nd-doped phosphate fiber [19]. Up until now, nearly all of the IAG waveguide lasers utilize side pumping technique [13, 19, 20, 23, 96]. Although none of them experimentally demonstrated the exact coupling efficiency using side pumping technique, the reported highest slope efficiency is $\sim 30\%$ by an IAG planar waveguide laser from our group [23]. The reflections of the air-cladding and core-cladding interfaces, as well as the core size [96] will contribute to the loss of coupling. Moreover, the non-uniformity of the pumping along the whole length of fiber will also affect the pump efficiency. In addition, the side pumping technique is not applicable for long fibers which might be desired for high power performance.

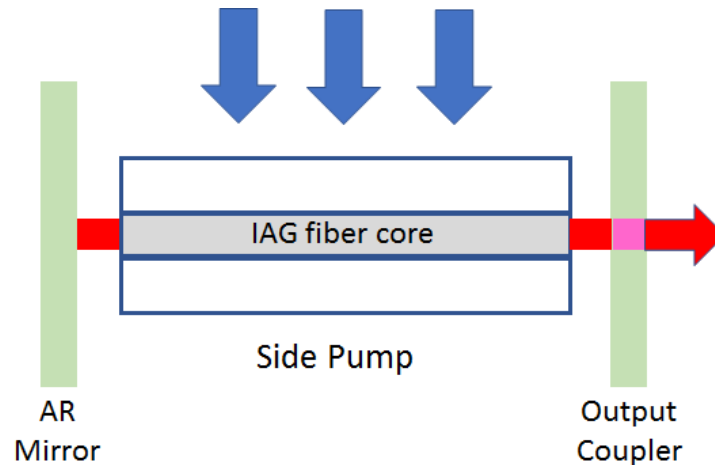


Figure 4-2 Side pumping scheme for IAG fiber lasers

4.2.2 End pumping

For end pumping technique, usually a lens is used to couple the pump light directly into the facet of the fibers, as shown in Figure 4-3. The pump light could be coupled either to the core or the cladding of the fibers. End pumping technique has high efficiency in traditional index-guided waveguide lasers. The invention of cladding pumping technique has significantly increased the threshold of launched pump power and the coupling efficiency due to the acceptance of large area of input as well as large NA . Therefore almost all of the high-power fiber lasers adopt cladding pumping technique. A double-clad fiber is generally used for cladding pumping, for which the pump beam is launched into the inner cladding of the fiber and confined within it by the outer cladding. The confined pump light is then progressively passing through the core and absorbed during its propagation along the fiber. As the cladding area is much larger than the core, more power could be launched into the inner cladding which greatly reduces the thermal and nonlinear effects and increases the output power.

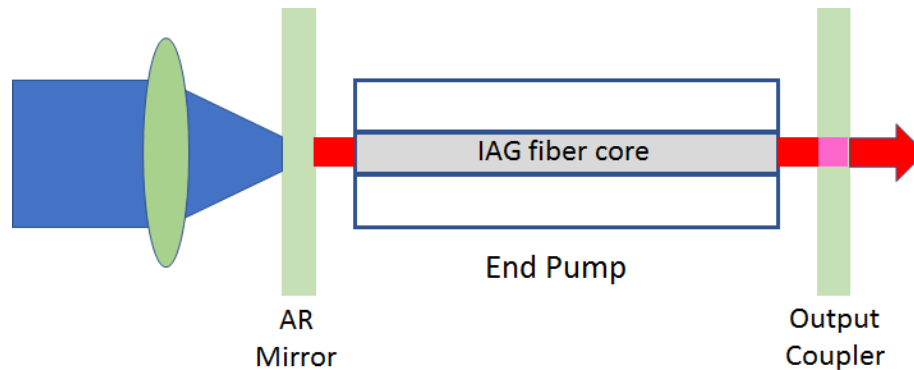


Figure 4-3 End pumping scheme for IAG fiber lasers (the above figure is an example of core pumping)

Although it is very successful to implement end pumping technique in traditional index-guided fiber lasers, it might not be efficient in IAG fiber lasers. The first reported slope efficiency in IAG fiber laser with cladding pumping was only less than 1% [21]. The author assumed that the low efficiency was due to index-antiguinding effect, which will prevent the pump power in the cladding passing into the core, and also introduce waveguide loss of the pump in the core. Therefore the author considered that end pumping was not applicable in IAG fiber lasers. After our analysis, we believe that the low efficiency of the cladding pumping is partly but not mainly due to index-antiguinding effect (the detailed analysis will be provided in Section 4.4). End pumping is still possible in IAG fiber lasers. In the following part of this section, we will numerically analyze the end pumping efficiency and compare between core and cladding pumping schemes.

Finite-difference beam propagation method (FD-BPM) could be used to simulate the pump and signal evolutions along the propagation direction, for either core or cladding pumping schemes. Let us take the parameters from [21] as an example to show the efficiency difference between core and cladding pump. The simulated fiber has a core diameter of 200 μm and inner cladding diameter of 340 μm with the corresponding

refractive indices of ~ 1.5689 and 1.5734 , respectively. In the case of cladding pumping, let us assume there exists another outer cladding with a diameter of $400 \mu\text{m}$ and an index of 1 (air cladding). The pump wavelength in the simulation is $\sim 803 \text{ nm}$ and the fiber length is 26 mm . There is a $1\% \text{ Nd}^{3+}$ doping in the core, corresponding to a pump absorption coefficient of $\sim 277 \text{ m}^{-1}$ [96]. As we are only interested in the pump evolution, for simplicity let us use a fixed complex core index $1.5689 - i \times 1.7721 \times 10^{-5}$ with its imaginary part representing the pump absorption. In the simulation, the initial pump field has a significant effect to the pump evolution profile. For a flat-top pump with multimode input, the exact input field is difficult to obtain. However, a noisy input could be used to simulate the spatial incoherence [97] of the input pump field, with the expression of

$$E_0(x, y) = U(x, y)(1 + N_a A(x, y))e^{2\pi i N_p B(x, y)}. \quad (4.7)$$

where $U(x, y)$ represents the profile of coherent input beam, $A(x, y)$ and $B(x, y)$ are the normalized spatial distributions of the amplitude and phase noises. N_a and N_p are the amplitudes of amplitude noise and phase noise, respectively. In flat-top pumping, assume $U(x, y) = 1$ and there only exists the phase noise with a spatial distribution $B(x, y)$. Thus, input field is simplified to $E_0(x, y) = e^{2\pi i N_p B(x, y)}$. Moreover, let us assume the phase noise is random across the whole transverse section, such that B satisfies a random distribution in the interval $[0, 1]$. The value of N_p determines the degree of coherence (spatial frequency) of the input beam. For $N_p = 0$, the input beam has uniform transverse spatial phase. For the worst situation of $N_p = 1$, the spatial frequency content of the beam is greatly varied [97] leading to poor spatial coherence, where most of the incident rays could leave the fiber without being confined. This worst spatial coherence usually does not occur in the real

situation. In [97] $N_p = 0.2$ was used in the simulation. In our simulation, we consider more different choices of $N_p = 0, 0.4$ and 1 .

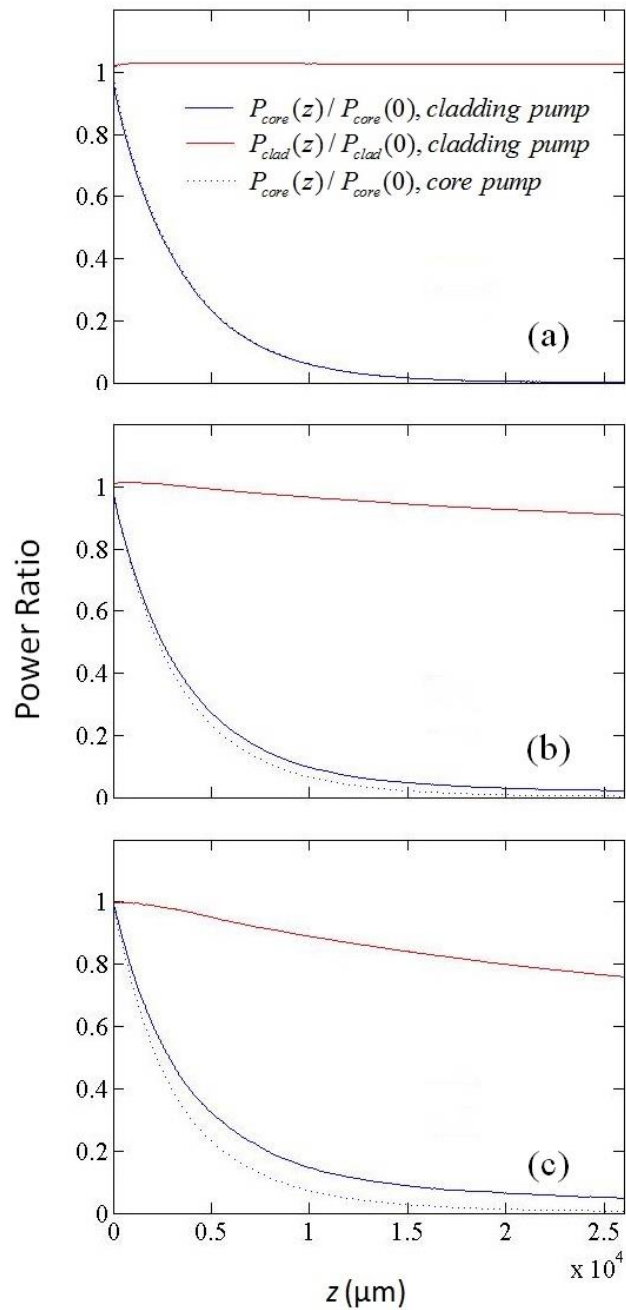


Figure 4-4 Power evolution profiles in the core (solid blue) and cladding (solid red) in case of cladding pump for the initial pump field with phase noise amplitudes of (a) $N_p = 0$, (b) $N_p = 0.4$ and (c) $N_p = 1$. Corresponding absorption coefficients of the core power are 279 , 233 and 193 m^{-1} , respectively. As a comparison, the power evolution profiles in the core for core pumping (dotted blue) are also plotted, with the absorption coefficient of 278 m^{-1} .

Figure 4-4 illustrates pump power evolutions for different phase noise amplitudes of (a) $N_p = 0$, (b) $N_p = 0.4$ and (c) $N_p = 1$, where in each figure the solid blue and red lines represent the power evolutions in the core and cladding for cladding pump, while the dotted blue line represents pump power evolution in the core for the core pumping scheme. From Figure 4-4(a) it is seen that for cladding pump with uniform phase input ($N_p = 0$), the cladding power is almost trapped in the cladding and unable to effectively pass through the core. The power evolutions in the core are nearly the same for cladding and core pumping. Corresponding absorption coefficient of the core power is 279 m^{-1} , which is very close to the core pumping with an absorption coefficient of 278 m^{-1} . In Figure 4-4(b) with some phase perturbation ($N_p = 0.4$), the cladding power is slightly coupled into the core ($\sim 10\%$), resulting slight increase of the core power (seen from the solid and dotted blue lines). Corresponding absorption coefficient of the core power is 233 m^{-1} , which is close to the value in the situation of core pumping. Even in the worst situation of $N_p = 1$, only small fraction of cladding power ($\sim 20\%$) is coupled into the core, as seen from Figure 4-4(c). Corresponding absorption coefficient of the core power is 193 m^{-1} , which reduces the absorption coefficient to 70% compared to core pumping. However, this value (70%) is still far away compared to the ideal situation where the effective absorption coefficient is reduced to $A_{co}/A_{cl} = 34.6\%$, with A_{co} and A_{cl} the core and cladding areas, respectively. The reason why more cladding power is leaked into the core at $N_p = 1$ is because more beams with high spatial frequencies (large beam angles) are able to pass through the core-cladding interface. However, as previously stated, it is usually not desired to have a pump with $N_p = 1$ from pump efficiency perspective. Thus, it is seen from Figure 4-4 that cladding pumping barely improves the pump efficiency compared to core pumping in IAG fibers.

Although Figure 4-4 shows that core and cladding pumping schemes have similar efficiency in IAG fiber lasers for the flat-top pump with input phase noise having some degree of correlation, it does not explain whether the low efficiency of cladding pump is due to index antiguiding effect. Figure 4-5 illustrates pump power evolution profiles in core and cladding in IAG and IG fibers at input phase noise amplitudes of (a) $N_p = 0$ and (b) $N_p = 0.4$ (the worst situation of $N_p = 1$ is not considered in the simulation), for the same simulation parameters in Figure 4-4, except the core and cladding indexes are switched such that the core index is higher than the cladding (IG waveguide). The blue and red solid lines represent the power evolution in the core and cladding in IAG fibers, while the blue and red dashed lines are for IG fiber lasers. It is clearly seen from Figure 4-5 that IG is more beneficial to improve the pump efficiency as more cladding power ($\sim 18\%$ for $N_p = 0$ and $\sim 20\%$ for $N_p = 0.4$) is coupled into the core. Therefore, index antiguiding truly affects the cladding pump efficiency. However, it is still seen that even index-guiding could not effectively increase the pump efficiency. One possible reason is that the round cladding shape is not effective compared to other like D-shape and rectangle-shape claddings [98]. Another reason is that the core size of the IAG fiber is usually very large ($> 100 \mu\text{m}$) such that the overlap between doping area and cladding modes is relatively small. This could be verified by Figure 4-6 which demonstrates the simulated pump power evolutions for IAG and IG fiber lasers with smaller core diameter of $40 \mu\text{m}$ and inner cladding of $125 \mu\text{m}$. Other simulation parameters are maintained unchanged. It is observed from Figure 4-6 that for different input fields ($N_p = 0$ and 0.4) and IG, the cladding power could more efficiently pass into the core and assist the pump efficiency. However, for IAG fibers, most of the cladding power is still trapped in the cladding, yielding low pump efficiency.

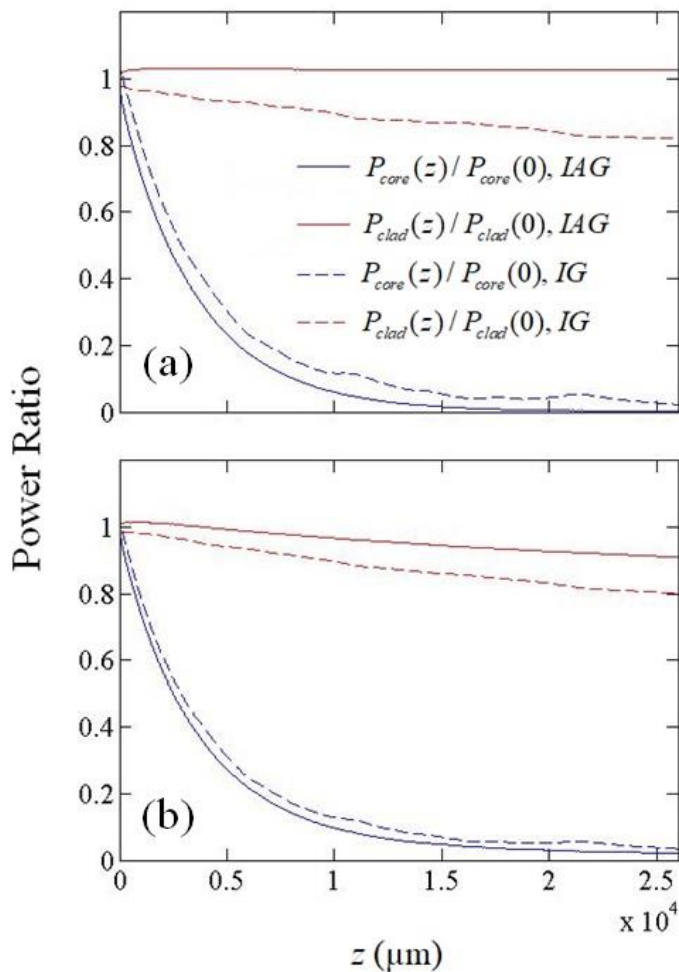


Figure 4-5 Power evolutions in core and cladding for flat-top cladding pump in IAG and IG fibers at input phase noise amplitudes of (a) $N_p = 0$ and (b) $N_p = 0.4$.

Thus, from both Figure 4-5 and Figure 4-6 it is seen that cladding pump is not efficient in IAG fiber lasers due to both index antiguiding effect and large core size. Core pumping will be more suitable for IAG fiber lasers. Moreover, the large core size (usually $> 100 \mu\text{m}$) in IAG fibers is comparable to the inner cladding size of most double-clad fibers, which favors the core pumping scheme from coupling efficiency perspective. Another reason for core pumping is that the fiber length is usually preferred not to long for high output efficiency (which will be explained in Section 4.4). Therefore cladding pumping is

generally not appropriate since it is usually accompanied with long fiber length for the low effective pump absorption coefficient.

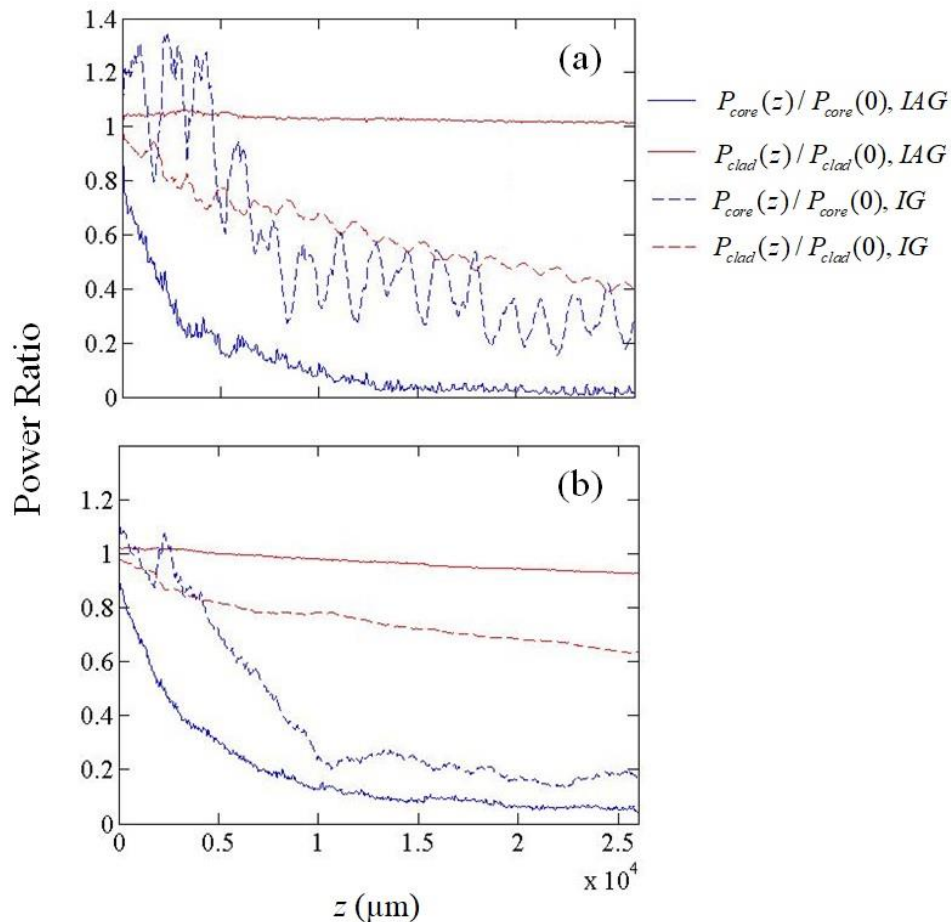


Figure 4-6 Power evolutions in core and cladding for flat-top cladding pump in IAG and IG fiber lasers with small core diameter of $40 \mu\text{m}$ and inner cladding of $125 \mu\text{m}$, at input phase noise amplitudes of (a) $N_p = 0$ and (b) $N_p = 0.4$.

4.2.3 Some improvements for end pumping scheme

Prior to my discussion in the previous section, it was believed that end pumping technique was not efficient in IAG waveguide lasers due to index-antiguinding effect, which results in the loss of pump power in the core and the difficulty of cladding power coupling into the core. Some alternatives were proposed to ensure index guiding at the pump

wavelength while maintaining index antiguiding at the signal wavelength. One method is to consider adding Bragg layers between core and cladding to confine the pump light while ensuring that the lasing signal is index-antiguided [99], as shown in Figure 4-7. The Bragg fiber is composed of concentric layers of alternating high- and low-index materials (Bragg cladding) surrounding a core, followed by a uniform outer cladding. The width and index of each layer need to be appropriately designed to ensure the index guiding condition of the pump light, while the signal is in the region of index antiguiding. The schematic of the propagation of pump and signal in Bragg IAG fibers is shown in Figure 4-7(c).

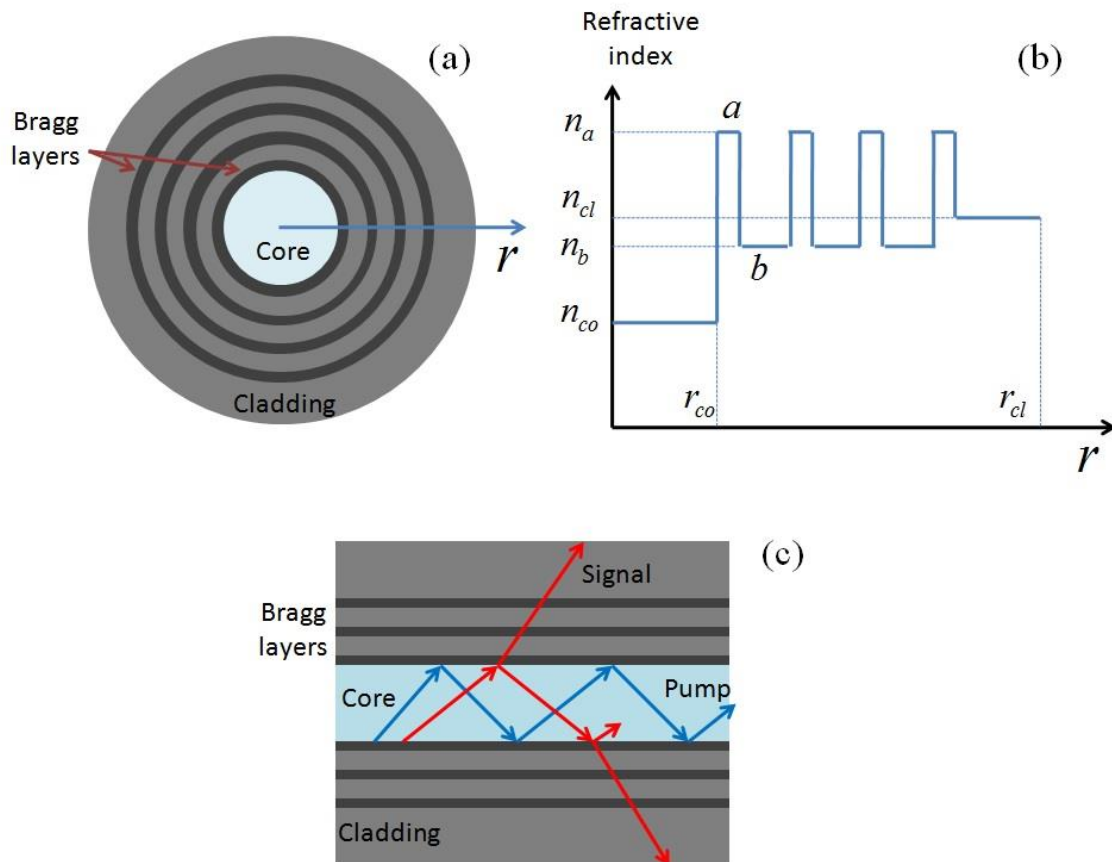


Figure 4-7 (a) Schematic of Bragg IAG fiber, (b) Radial index profile and (c) Schematic of pump and signal propagation in Bragg IAG fibers.

Although this method seems promising, there are several drawbacks. The first and biggest issue is the difficulty to fabricate Bragg layers. The later one is that this design only works for core-pumped systems, in which the waveguide loss of the pump is generally negligible compared to the pump absorption. Therefore it might be futile to reduce the waveguide loss of the pump. More details will be discussed in Section 4.4.

Besides using photonic bandgap to confine the pump light, another method was proposed to use the dispersion to control the index and therefore confine the pump light [100, 101]. As shown in Figure 4-8, the index of the core after dispersion control is higher than the cladding at the pump wavelength, and lower than the cladding at the signal wavelength. This fiber is called index crossover gain-guided index-antiguided fiber. In this structure, the pump light propagates in an IG waveguide while the signal light propagates in an IAG waveguide. However, one issue of this method is the difficulty to manufacture the required index profile. Another issue is that even IG waveguide will be inefficient for cladding pump if the core size is very large, as seen from Figure 4-5.

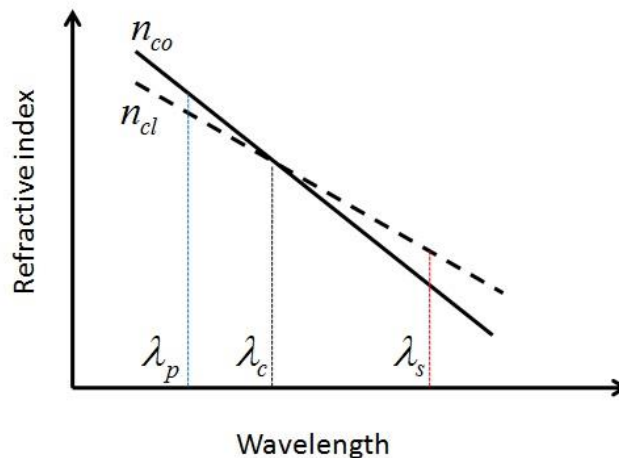


Figure 4-8 Schematic of using dispersion to control the indices of core and cladding

4.3 Output characteristics of uniformly side-pumped index-antiguidded fiber lasers

In Chapter 3, both amplifier and laser models are provided and the output characteristics of fundamentally single mode in uniformly side-pumped IAG planar waveguide lasers are investigated. For IAG fibers, similar amplifier and laser models can be obtained and the output characteristics of fundamentally single mode can be investigated.

The amplifier model for IAG fibers could be derived from Eq. (3.16), with intensity expressed as

$$I(r, \theta, z) = P(z) \cdot f(r, \theta). \quad (4.8)$$

where $P(z)$ is the transverse power in the core at distance z and $f(r, \theta)$ is the normalized intensity profile of FM (Eq. (4.1)) in the core satisfying

$$\int_0^{2\pi} \int_0^a f(r, \theta) r dr d\theta = 2\pi \int_0^a f(r, \theta) r dr = 1. \quad (4.9)$$

Substitute Eq. (4.8) into Eq. (3.16) and integrate both sides over the core area, yielding

$$\frac{dP(z)}{dz} \int_0^a f(r, \theta) r dr = g_0 P(z) \int_0^a \frac{f(r, \theta) r}{1 + sP(z) f(r, \theta)} dr - \alpha P(z) \int_0^a f(r, \theta) r dr. \quad (4.10)$$

Or further simplified to

$$\frac{dP(z)}{dz} = g_0 P(z) \cdot 2\pi \int_0^a \frac{f(r, \theta) r}{1 + sP(z) f(r, \theta)} dr - \alpha P(z). \quad (4.11)$$

Here the modal gain coefficient is

$$g_m = 2\pi g_0 \int_0^a \frac{f(r, \theta) r}{1 + sP(z) f(r, \theta)} dr. \quad (4.12)$$

Remove the saturation factor s and use the same parameter of averaged intensity

$I'(z) = sP(z) / (\pi a^2)$ will further modify Eq. (4.11) to

$$\frac{dI'(z)}{dz} = g_0 I'(z) \int_0^a \frac{2\pi f(r, \theta) r}{1 + \pi a^2 I'(z) f(r, \theta)} dr - \alpha I'(z). \quad (4.13)$$

It is seen that the amplifier model for fiber waveguide is similar to the model for planar waveguide in Eq. (3.20).

The oscillator model could then be derived from Eqs. (4.13) and (3.37), with the following expression

$$\frac{dI^{++}(z)}{dz} = g_0 I^{++}(z) \int_0^a \frac{2\pi f(r, \theta) r}{1 + \pi a^2 (I^{++}(z) + c / I^{++}(z)) f(r, \theta)} dr - \alpha I^{++}(z). \quad (4.14)$$

which subjects to the boundary conditions

$$c = \frac{1}{R_r} (I^{++}(0))^2 = R_r (I^{++}(L))^2. \quad (4.15)$$

here $I^{++}(z)$ is the normalized forward-propagating intensity. Based on Eqs. (4.14) and (4.15), the output normalized intensity could be calculated for different cavity parameters. Figure 4-9 shows the maximum extraction efficiency η_{\max} as a function of optimum output coupler R_{opt} for different combination of unsaturated single-pass gains and internal losses. From which it is seen that η_{\max} in IAG fiber lasers behaves similar to IAG slab lasers (Figure 3-8) as well as plane-wave oscillators. Very high extraction efficiency is only attainable with very low loss and nearly 100% output coupler reflectance. As loss increases, η_{\max} decreases significantly.

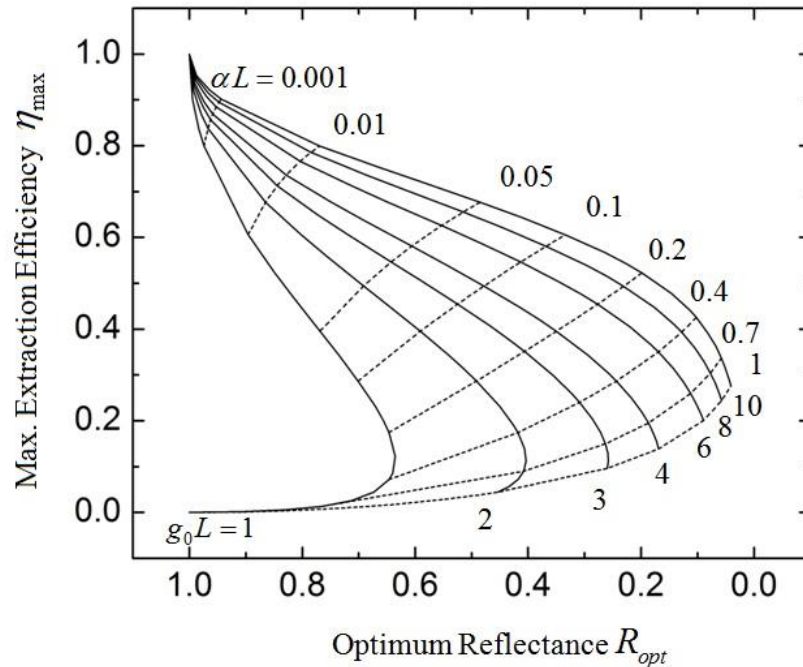


Figure 4-9 Maximum extraction efficiency versus optimum output coupler reflectance in uniformly side-pumped IAG fiber lasers for various values of g_0L and αL (fundamentally-single-mode operation is assumed).

4.4 Output characteristics of core-pumped index-antiguided fiber lasers

In the previous section, we have demonstrated the output efficiency of fundamentally single mode in uniformly side-pumped IAG fiber lasers. The behavior of output efficiency is similar to plane-wave lasers. Maximum optical extraction efficiency could approach to unity when the internal loss (includes IAG waveguide loss, mirror gap loss, scattering loss, etc.) is very small and output coupler is close to one. Some experiments demonstrated less than 30% of slope efficiency [22, 23] using side pumping scheme. The low output efficiency might due to the low pump efficiency, large internal loss and non-optimized output coupler.

End pumping is more attractive than side pumping due to high coupling efficiency and easy handling. In Section 4.2.2 we have discussed the possibility of end pumping in IAG fiber lasers. We have shown that cladding pumping is not effective since most of the cladding power is trapped in the inner cladding due to both index-antiguinding effect and large core size. Core pumping should be used in IAG lasers. Experimental result [21] demonstrated a very low output efficiency using cladding pumping technique. The low efficiency is partly due to the cladding pumping method, which is proved to be inefficient in Section 4.2.2. However, there are some other factors that mainly affect the output efficiency.

In this section, we will analyze the output efficiency of fundamentally single mode in core-pumped IAG fiber lasers and indicate which factors have impact on slope efficiency, and further explain why experimental result [21] demonstrated low efficient.

4.4.1 Oscillator model for core-pumped index-antiguinded fiber lasers

The construction of the oscillator model needs to know the rate equations for energy band diagram. There are many different energy band diagrams for different doping materials and pump wavelengths. However, we could generalize the four-level, three-level and quasi-three-level systems into one group of simple two-level system, which shares similar rate equations [102]. For instance, Figure 4-10(a) demonstrates the general four-level systems such as 1060 nm Nd^{3+} -doped fibers. N_0 , N_1 , N_2 and N_3 are the population densities at level 0, 1, 2 and 3, respectively. τ_{32} and τ_{10} are the non-radiative decay lifetimes from level 3 to level 2, and level 1 to level 0, respectively. τ_{21} and τ_{20} are the decay lifetimes (including spontaneous and non-radiative transitions) from level 2 to level 1, and level 2 to level 0, respectively. σ_{ap} , σ_{ep} are the stimulated absorption and emission cross-sections at

the pump wavelength, while σ_{as} , σ_{es} are the stimulated absorption and emission cross-sections at the signal wavelength.

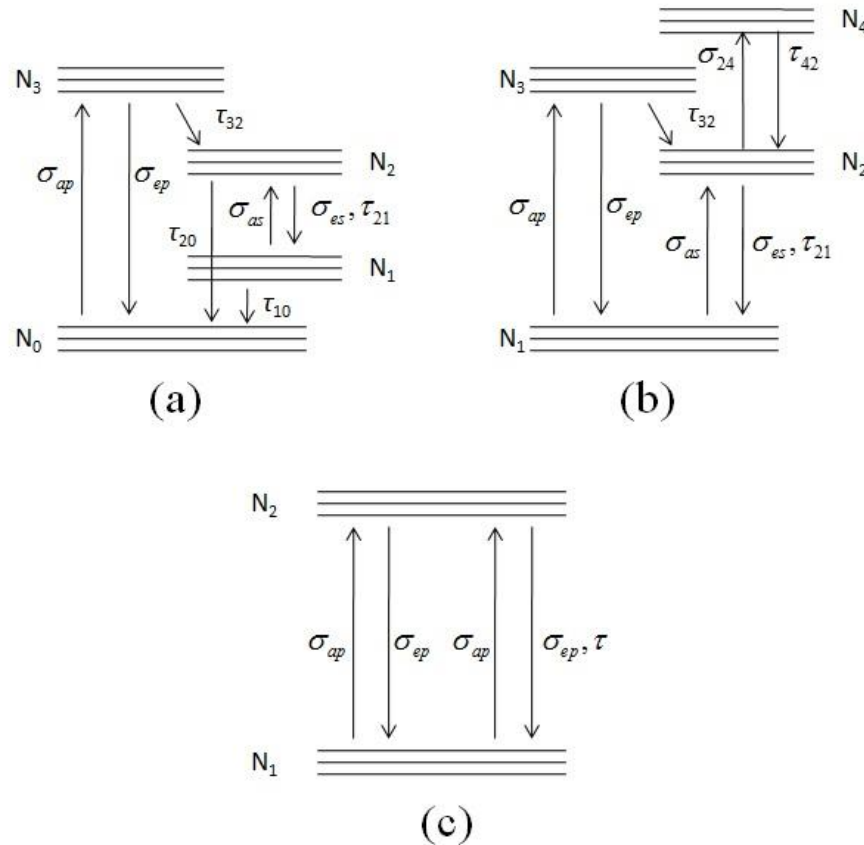


Figure 4-10 (a) General four-level system such as 1060 nm Nd^{3+} , (b) general three-level system like Er^{3+} , and (c) generalized two-level system.

Usually the non-radiative decay rates from level 3 to level 2, and from level 1 to level 0 are very fast (τ_{32} , $\tau_{10} \approx 0$), such that N_1 , $N_3 \approx 0$. Therefore the four-level band could be reduced to a two-level band, as shown in Figure 4-10(c). For a general three-level system in Figure 4-10(b), it is also reasonable to assume that the non-radiative decays, either interband or intraband, are very fast and could be ignored (τ_{32} , τ_{42} , $\tau_{10} \approx 0$). If we do not consider the excited state absorption ($\sigma_{24} \approx 0$), the general three-level system could also be reduced to a two-level system in Figure 4-10(c). For other quasi-three level systems such as Yb^{3+} , they could also reduce to the generalized two-level system shown in Figure 4-10(c).

Thus, we could construct the rate equations for the generalized two-level system which could simulate the general four-level, three-level and quasi three-level systems. From Figure 4-10(c), the generalized rate equations are

$$\frac{dN_2(r, \theta)}{dt} = N_1(r, \theta)(W_{12}(\lambda_p) + W_{12}(\lambda_s)) - N_2(r, \theta)(W_{21}(\lambda_p) + W_{21}(\lambda_s)) - N_2(r, \theta) / \tau, \quad (4.16)$$

$$N_1(r, \theta) + N_2(r, \theta) \approx N(r, \theta) = N.$$

where N is the total population density and assumed to be constant, W_{12} and W_{21} are the stimulated absorption and emission rates between the two levels, which relate to the absorption and emission cross-sections as

$$W_{12}(\lambda_p) = \sigma_{ap} \frac{I_p(r, \theta, z)}{h\nu_p} = \frac{\sigma_{ap}}{h\nu_p} \Gamma_p(r, \theta)(P_p^+(z) + P_p^-(z)),$$

$$W_{21}(\lambda_p) = \sigma_{ep} \frac{I_p(r, \theta, z)}{h\nu_p} = \frac{\sigma_{ep}}{h\nu_p} \Gamma_p(r, \theta)(P_p^+(z) + P_p^-(z)), \quad (4.17)$$

$$W_{12}(\lambda_s) = \sigma_{as} \frac{I_s(r, \theta, z)}{h\nu_s} = \frac{\sigma_{as}}{h\nu_s} \Gamma_s(r, \theta)(P_s^+(z) + P_s^-(z)),$$

$$W_{21}(\lambda_s) = \sigma_{es} \frac{I_s(r, \theta, z)}{h\nu_s} = \frac{\sigma_{es}}{h\nu_s} \Gamma_s(r, \theta)(P_s^+(z) + P_s^-(z)).$$

In the above equations, h is the Planck constant, ν_p and ν_s are the pump and signal frequencies. I_p and I_s are the pump and signal intensities, respectively. P_p^+ and P_p^- are the forward and backward powers of transverse pump mode, P_s^+ and P_s^- are the forward and backward powers of the transverse signal mode. $\Gamma_p(r, \theta)$ and $\Gamma_s(r, \theta)$ are the power filling distributions (or normalized intensity profiles) for pump and signal, with expressions of

$$\begin{aligned}\Gamma_p(r, \theta) &= \frac{I_p(r, \theta)}{\int_0^{2\pi} \int_0^\infty I_p(r, \theta) r dr d\theta}, & \int_0^{2\pi} \int_0^a \Gamma_p(r, \theta) r dr d\theta &= \frac{P_p^{core}}{P_p^{core} + P_p^{clad}}. \\ \Gamma_s(r, \theta) &= \frac{I_s(r, \theta)}{\int_0^{2\pi} \int_0^\infty I_s(r, \theta) r dr d\theta}, & \int_0^{2\pi} \int_0^a \Gamma_s(r, \theta) r dr d\theta &= \frac{P_s^{core}}{P_s^{core} + P_s^{clad}}.\end{aligned}\quad (4.18)$$

where A_{core} is the area of the core, A_{clad} is the area of the cladding, a is the core radius, P_p^{core} and P_p^{clad} are the pump powers in the core and cladding, respectively. For the situation of core pumping, we assume $P_p^{clad} = 0$. P_s^{core} and P_s^{clad} are the signal powers in the core and cladding. For IAG fibers with large core size, most of the modal power is occupied in the core and we could assume $P_s^{clad} = 0$. From Eqs. (4.16), (4.17) and the steady-state condition ($dN_2/dt = 0$), we could obtain

$$\frac{N_2(r, \theta, z)}{N} \approx \frac{\frac{(P_p^+(z) + P_p^-(z))\sigma_{ap}\Gamma_p(r, \theta)}{h\nu_p} + \frac{(P_s^+(z) + P_s^-(z))\sigma_{as}\Gamma_s(r, \theta)}{h\nu_s}}{\frac{(P_p^+(z) + P_p^-(z))(\sigma_{ap} + \sigma_{ep})\Gamma_p(r, \theta)}{h\nu_p} + \frac{1}{\tau} + \frac{(P_s^+(z) + P_s^-(z))(\sigma_{as} + \sigma_{es})\Gamma_s(r, \theta)}{h\nu_s}}. \quad (4.19)$$

Equation (4.19) is then coupled with the following equations relating the evolution of pump and signal powers to form the complete governing equations for oscillator model,

$$\pm \frac{dP_p^\pm(z)}{dz} = \left\{ \int_0^{2\pi} \int_0^a [(\sigma_{ap} + \sigma_{ep})N_2(r, \theta, z) - \sigma_{ap}N(r, \theta, z)] \Gamma_p(r, \theta) r dr d\theta \right\} P_p^\pm(z) - \alpha_p P_p^\pm(z), \quad (4.20)$$

$$\pm \frac{dP_s^\pm(z)}{dz} = \left\{ \int_0^{2\pi} \int_0^a [(\sigma_{as} + \sigma_{es})N_2(r, \theta, z) - \sigma_{as}N(r, \theta, z)] \Gamma_s(r, \theta) r dr d\theta \right\} P_s^\pm(z) - \alpha_s P_s^\pm(z). \quad (4.21)$$

where α_p and α_s are the internal losses of pump and signal modes. The validity of Eqs. (4.19) - (4.21) includes several assumptions: (1) The energy band diagrams should be either general four- or three-level systems which could be generalized into a quasi two-level system. (2) A narrow-band signal is considered such that $P_s^\pm(z, \lambda) \approx P_s^\pm(z)\delta(\lambda - \lambda_s)$. (3) There is only one pump mode, and also one signal mode (fundamentally single mode).

Before solving the above coupled equations, an auxiliary equation is needed for Eq. (4.21), which is expressed as

$$\begin{aligned} \frac{dP_s^+(z)}{P_s^+(z)dz} + \frac{dP_s^-(z)}{P_s^-(z)dz} &= 0, \\ P_s^+(z)P_s^-(z) &= c. \end{aligned} \quad (4.22)$$

where c is a constant. Assume the cavity length is L , and R_l and R_r are the left- and right-hand reflectivities at $z = 0$ and $z = L$ for the signal light. The boundary equations are $P_s^+(0) = R_l P_s^-(0)$, $P_s^-(L) = R_r P_s^+(L)$, or expressed as

$$c = P_s^+(0)^2 / R_l = R_r P_s^+(L)^2. \quad (4.23)$$

The above coupled equations could be further reduced to simpler forms. Let us consider the pump light is injected from the left end and no pump light is reflected or injected from the right end, the term P_p^- in Eqs. (4.19) and (4.20) could be neglected. Moreover, it is reasonable to assume that the upper-level population density is very small compared to the total population density ($N_2 \ll N$) [102]. Eq. (4.20) could be reduced to

$$\frac{dP_p^+(z)}{dz} = -\sigma_{ap} N P_p^+(z) \int_0^{2\pi} \int_0^a \Gamma_p(r, \theta) r dr d\theta - \alpha_p P_p^+(z) = -\sigma_{ap} N P_p^+(z) - \alpha_p P_p^+(z). \quad (4.24)$$

Thus, the pump power could be analytically expressed as

$$P_p^+(z) = P_p^+(0) \exp[-(\sigma_{ap} N + \alpha_p)z]. \quad (4.25)$$

which is a simple exponential decay profile. In addition, usually we have $\sigma_{ep} \ll \sigma_{ap}$ and $\sigma_{as} \ll \sigma_{es}$. Since $N_2 \ll N$, it is derived from Eq. (4.19) that

$$\begin{aligned} \frac{P_p^+(z) \sigma_{ap} \Gamma_p(r, \theta)}{h\nu_p} &\approx \frac{P_p^+(z) (\sigma_{ap} + \sigma_{ep}) \Gamma_p(r, \theta)}{h\nu_p} \\ &\ll \frac{1}{\tau} + \frac{(P_s^+(z) + P_s^-(z)) (\sigma_{as} + \sigma_{es}) \Gamma_s(r, \theta)}{h\nu_s}. \end{aligned} \quad (4.26)$$

Therefore Eq. (4.19) could be rewritten to

$$\begin{aligned} \frac{N_2(r, \theta, z)}{N} &\approx \frac{\frac{P_p^+(z)\sigma_{ap}\Gamma_p(r, \theta)}{h\nu_p} + \frac{(P_s^+(z) + P_s^-(z))\sigma_{as}\Gamma_s(r, \theta)}{h\nu_s}}{\frac{1}{\tau} + \frac{(P_s^+(z) + P_s^-(z))(\sigma_{as} + \sigma_{es})\Gamma_s(r, \theta)}{h\nu_s}} \\ &= \frac{\frac{P_p^+(z)\sigma_{ap}\bar{\Gamma}_p(r, \theta)}{h\nu_p} + \frac{(P_s^+(z) + P_s^-(z))\sigma_{as}\bar{\Gamma}_s(r, \theta)}{h\nu_s}}{1 + \frac{(P_s^+(z) + P_s^-(z))(\sigma_{as} + \sigma_{es})\bar{\Gamma}_s(r, \theta)}{h\nu_s}}. \end{aligned} \quad (4.27)$$

If we define the saturated power as

$$P_{sat} = \frac{h\nu_s A_{core}}{(\sigma_{as} + \sigma_{es})\tau}. \quad (4.28)$$

Eq. (4.27) is further reduced to

$$\frac{N_2(r, \theta, z)}{N} = \frac{\frac{P_p^+(z)\sigma_{ap}\bar{\Gamma}_p(r, \theta)}{h\nu_p} - \frac{\sigma_{as}}{\sigma_{as} + \sigma_{es}}}{1 + \frac{P_s^+(z) + P_s^-(z)}{P_{sat}}\Gamma_s(r, \theta)A_{core}} + \frac{\sigma_{as}}{\sigma_{as} + \sigma_{es}}. \quad (4.29)$$

Define the signal gain in Eq. (4.21) as

$$g_s(z) = \left\{ \int_0^{2\pi} \int_0^a [(\sigma_{as} + \sigma_{es})N_2(r, \theta, z) - \sigma_{as}N(r, \theta, z)]\Gamma_s(r, \theta)rdrd\theta \right\}. \quad (4.30)$$

If we assume a uniform pump across the transverse section, such that $\Gamma_p(r, \theta) = \Gamma_p$.

Substitute Eq. (4.29) into Eq. (4.30), yielding

$$\begin{aligned} g_s(z) &= N \int_0^{2\pi} \int_0^a \left[\frac{\frac{P_p^+(z)\sigma_{ap}\bar{\Gamma}_p(r, \theta)}{h\nu_p} (\sigma_{as} + \sigma_{es}) - \sigma_{as}}{1 + \frac{P_s^+(z) + P_s^-(z)}{P_{sat}}\Gamma_s(r, \theta)A_{core}} \right] \Gamma_s(r, \theta)rdrd\theta \\ &= \int_0^{2\pi} \int_0^a \left[\frac{g_0(z)}{1 + \Gamma_s(r, \theta)A_{core}(P_s^+(z) + P_s^-(z))/P_{sat}} \right] \Gamma_s(r, \theta)rdrd\theta. \end{aligned} \quad (4.31)$$

where the unsaturated signal gain coefficient is

$$\begin{aligned}
g_0(z) &= N \left[\frac{P_p^+(z) \sigma_{ap} \bar{\Gamma}_p}{h\nu_p} (\sigma_{as} + \sigma_{es}) - \sigma_{as} \right] \\
&= N \left[\frac{P_p^+(0) \exp[-(\sigma_{ap} N + \alpha_p)z]}{h\nu_p} \sigma_{ap} \bar{\Gamma}_p (\sigma_{as} + \sigma_{es}) - \sigma_{as} \right].
\end{aligned} \tag{4.32}$$

Equation (4.21) will reduce to a final form,

$$\frac{dP_s^+(z)}{dz} = \left[\int_0^{2\pi} \int_0^a \left[\frac{g_0(z)}{1 + \Gamma_s(r, \theta) A_{core} (P_s^+(z) + c / P_s^+(z)) / P_{sat}} \right] \Gamma_s(r, \theta) r dr d\theta \right] P_s^+(z) - \alpha_s P_s^+(z). \tag{4.33}$$

If we assume normalized intensity by $I^\pm(z) = P_s^\pm(z) / P_{sat}$ and change the constant c in Eq. (4.33) to $c P_{sat}^2$. We find that Eq. (4.33) has the similar expression as Eq. (4.14) for uniform side pumping. The only difference between end pumping and uniform side pumping is that the gain in end pumping is z -dependent, while in uniform side pumping is a constant ($g_0(z) = g_0$). We could define a single-pass unsaturated gain for both uniform side pumping and end pumping systems, which is expressed as

$$\begin{aligned}
\int_0^L g_0(z) dz &= \int_0^L N \left[\frac{P_p^+(0) \exp[-(\sigma_{ap} N + \alpha_p)z]}{h\nu_p} \sigma_{ap} \bar{\Gamma}_p (\sigma_{as} + \sigma_{es}) - \sigma_{as} \right] dz \\
&= N \left[\frac{P_p^+(0) \sigma_{ap} \bar{\Gamma}_p (\sigma_{as} + \sigma_{es})}{h\nu_p (\sigma_{ap} N + \alpha_p)} (1 - \exp[-(\sigma_{ap} N + \alpha_p)L]) - \sigma_{as} L \right].
\end{aligned} \tag{4.34}$$

The unsaturated single-pass gain is an important parameter to characterize the effective gain that will be used in the next section. The threshold power of the fundamental mode could be obtained by Eqs. (4.34) and (3.36), with the final expression of

$$P_p^+(0)^{th} = \frac{\sigma_{as} NL + \alpha_s L - \frac{1}{2} \ln R_l R_r}{(\sigma_{as} + \sigma_{es}) N} \frac{h\nu_p (\sigma_{ap} N + \alpha_p)}{\sigma_{ap} \Gamma_p \tau (1 - \exp[-(\sigma_{ap} N + \alpha_p)L])}. \tag{4.35}$$

After the above derivations, the original model from Eqs. (4.19) -(4.21) could be greatly simplified to Eq. (4.33) with the boundary condition of Eq. (4.23).

Note that Eq. (4.31) only considers one pump core-mode. In the situation of multimoded pumping from one end, Eqs. (4.24) and (4.25) are changed to

$$\frac{dP_{pj}^+(z)}{dz} = -\sigma_{ap}NP_{pj}^+(z) - \alpha_{pj}P_{pj}^+(z), \quad j = 1, \dots, m \quad (4.36)$$

$$P_{pj}^+(z) = P_{pj}^+(0) \exp[-(\sigma_{ap}N + \alpha_{pj})z]. \quad (4.37)$$

where m is the number of propagating pump modes, P_{pj}^+ is the forward-propagating pump power in j^{th} mode and α_{pj} is the corresponding distributive loss. Note that the above equations do not consider the coupling between pump modes. The effect of multimoded pumping only changes the signal gain in Eq. (4.31) to

$$g_s(z) = N \int_0^{2\pi} \int_0^a \left[\frac{\sigma_{ap}\tau \sum_{j=1}^m P_{pj}^+(z) \Gamma_{pj}(r, \theta)}{h\nu_p} (\sigma_{as} + \sigma_{es}) - \sigma_{as} \right] \Gamma_s(r, \theta) r dr d\theta \quad (4.38)$$

$$= \int_0^{2\pi} \int_0^a \left[\frac{g_0(r, \theta, z)}{1 + \Gamma_s(r, \theta) A_{core} (P_s^+(z) + P_s^-(z)) / P_{sat}} \right] \Gamma_s(r, \theta) r dr d\theta.$$

where the unsaturated gain is

$$g_0(r, \theta, z) = N \left[\frac{\sigma_{ap}\tau \exp(-\sigma_{ap}Nz) \sum_{j=1}^m P_{pj}^+(0) \exp(-\alpha_{pj}z) \Gamma_{pj}(r, \theta)}{h\nu_p} (\sigma_{as} + \sigma_{es}) - \sigma_{as} \right]. \quad (4.39)$$

4.4.2 Improve output efficiency in core-pumped index-antiguide fiber lasers

It is interesting to see that except IAG fiber lasers, all other LMA fiber lasers were demonstrated to yield high slope efficiency of $> 60\%$ [6, 8, 10, 88, 103, 104] with long

fiber length (\sim several meters) and end pumping scheme. From the loss perspective, we can see that the confinement losses of fundamental mode in those LMA fibers were usually designed to be negligible or smaller than 0.2 dB/m. However, this loss value is typically very large in IAG fibers (1.74/m in Ref. [21]). It is important to investigate how to achieve high output efficiency in IAG fiber lasers with large confinement loss.

The structure of this section is as follows. In Section 4.4.2.1 I will first introduce the background of slope efficiency in a low-loss resonator, giving an implication of what parameters will affect the output efficiency. Detailed analysis of those parameters will be covered in Sections 4.4.2.2 - 4.4.2.5 and the requirements of those parameters for high efficiency will be given.

4.4.2.1 Background: slope efficiency in a low-loss resonator

In order to understand which parameters affect the output efficiency in core-pumped IAG fiber lasers, let us first start the analysis from a simple case of homogeneous plane-wave oscillator. In a homogeneous plane-wave oscillator, the forward and backward propagating waves can be described by the following coupled equations [95]

$$\begin{aligned}\frac{dI^+}{dz} &= \frac{g_0}{1+(I^+ + I^-)/I_s} I^+ - \alpha_0 I^+, \\ \frac{dI^-}{dz} &= -\frac{g_0}{1+(I^+ + I^-)/I_s} I^- + \alpha_0 I^-. \end{aligned} \quad (4.40)$$

For a low-loss resonator, the forward and backward circulating intensities are nearly constant and the same along the cavity

$$I^+ \approx I^- \approx I. \quad (4.41)$$

From the steady-state condition requiring the roundtrip gain equals the roundtrip loss, it has

$$\oint \frac{g_0}{1 + 2I/I_{sat}} dz = 2\alpha_0 L - \ln R_l R_r = \delta_i + \delta_e. \quad (4.42)$$

$$I = \left(\frac{\oint g_0 dz}{\delta_i + \delta_e} - 1 \right) \frac{I_{sat}}{2} = \left(\frac{2g_0 L}{\delta_i + \delta_e} - 1 \right) \frac{I_{sat}}{2}. \quad (4.43)$$

The output intensity is then expressed as

$$I_{out} \approx \delta_e I = \delta_e \left[\frac{2g_0 L}{\delta_i + \delta_e} - 1 \right] \frac{I_{sat}}{2}. \quad (4.44)$$

where δ_e represents the round-trip external loss due to mirror reflections, or the total external coupling. δ_i is the round-trip internal loss which includes all other losses besides the external loss, such as waveguide loss, attenuation loss, scattering loss and coupling loss due to the mirror gap. In IAG fiber lasers, the round-trip external loss can be expressed as $\delta_e = -\ln R_l R_r$. Assume the left mirror has 100% reflectivity and $R_{oc} = R_r$, then $\delta_e = -\ln R_{oc}$. If we neglect the attenuation loss, scattering loss and mirror gap loss, the round-trip internal loss can be simplified as $\delta_i = 2\alpha_s L$. Here L is the cavity length and $2g_0 L$ is the round-trip unsaturated gain. I_{sat} is the saturated intensity and I_{out} is the output intensity. From Eq. (4.44) it is seen that the slope efficiency η_{slope} for a low-loss homogeneous plane-wave laser is

$$\eta_{slope} = \frac{dI_{out}}{d(g_0 L \cdot I_{sat})} = \frac{\delta_e}{\delta_i + \delta_e} = \frac{1}{\delta_i / \delta_e + 1} = \frac{1}{\delta_r + 1}. \quad (4.45)$$

which shows that the slope efficiency is only dependent on the internal to external loss ratio δ_r . The slope efficiency will be reduced if δ_r is large. Note that Eq. (4.45) is valid for plane-wave oscillator with uniform gain. In the situation of end pumping the unsaturated gain roughly exponentially decays with the expression demonstrated in Eq. (4.32) (assume one-side pumping), and Eq. (4.43) is changed to

$$\begin{aligned}
I &= \left(\frac{\oint g_0 dz}{\delta_i + \delta_e} - 1 \right) \frac{I_{sat}}{2} \\
&= \left(\frac{2N \left[\frac{P_p^+(0) \sigma_{ap} \Gamma_p (\sigma_{as} + \sigma_{es})}{h\nu_p (\sigma_{ap} N + \alpha_p)} (1 - \exp[-(\sigma_{ap} N + \alpha_p)L]) - \sigma_{as} L \right]}{\delta_i + \delta_e} - 1 \right) \frac{I_{sat}}{2}. \tag{4.46}
\end{aligned}$$

The slope efficiency is then expressed as

$$\begin{aligned}
\eta_{slope} &= \frac{d(I_{out} \cdot A_{core})}{dP_p^+(0)} \\
&= \frac{\delta_e}{\delta_i + \delta_e} 2N \left(\frac{\sigma_{ap} \Gamma_p (\sigma_{as} + \sigma_{es})}{h\nu_p (\sigma_{ap} N + \alpha_p)} (1 - \exp[-(\sigma_{ap} N + \alpha_p)L]) \right) \frac{I_{sat} \cdot A_{core}}{2} \\
&= \frac{\delta_e}{\delta_i + \delta_e} N \left(\frac{\sigma_{ap} \Gamma_p (\sigma_{as} + \sigma_{es})}{h\nu_p (\sigma_{ap} N + \alpha_p)} (1 - \exp[-(\sigma_{ap} N + \alpha_p)L]) \right) P_{sat} \\
&= \frac{\lambda_p}{\lambda_s} \cdot \frac{1}{\delta_r + 1} \cdot \frac{1 - \exp[-(\sigma_{ap} N + \alpha_p)L]}{1 + \alpha_p / \sigma_{ap} N}. \tag{4.47}
\end{aligned}$$

Here Eq. (4.47) uses the saturation power P_{sat} that is defined in Eq. (4.28). Compared to plane-wave oscillator with uniform gain (Eq. (4.45)), the slope efficiency for end pumping depends not only on δ_r but also gain. Here the gain is dependent on pump absorption coefficient $\sigma_{ap}N$, pump waveguide loss α_p and fiber length L .

Although Eq. (4.47) is only valid for low-loss resonator, it can provide the implication of how gain and δ_r affect the slope efficiency in core-pumped IAG fiber lasers. For more accurate numerical analysis, we will use the previous oscillator model in Section 4.4.1 to simulate the output power efficiency in core-pumped IAG fiber lasers.

In order to further analyze how laser parameters affect the output efficiency, let us first pull out all the related laser parameters as shown in Figure 4-11. Within these parameters, the gain is only dependent on fiber length L , pump absorption $\sigma_{ap}N$ and pump IAG loss α_p , while δ_r is only dependent on fiber length L , output coupler R_{oc} and signal

IAG loss α_s . We can first analyze the effect of gain to the output efficiency by studying the gain-related parameters L , $\sigma_{ap}N$ and α_p , which will be covered in Section 4.4.2.2. Then we can analyze the effect of δ_r to the output efficiency by studying the δ_r -related parameters L , R_{oc} and α_s , which will be covered in Section 4.4.2.3. Note that the fiber length L determines both gain and δ_r , therefore we need to finally combine both gain and δ_r effects to determine the requirement of fiber length to yield high efficiency, as shown in Section 4.4.2.4. Note that here we only consider slope efficiency and neglect the threshold power. Therefore in Section 4.4.2.5, both slope efficiency and threshold power are considered and the appropriate range of output coupler is discussed.

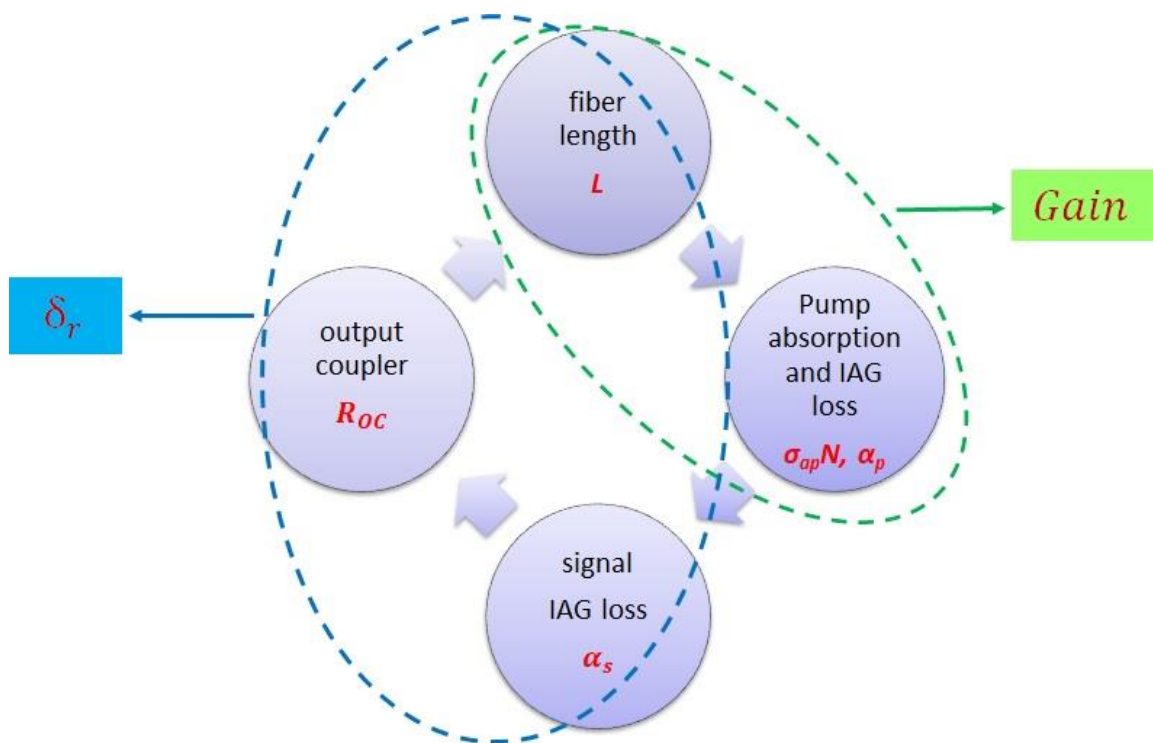


Figure 4-11 Laser parameters that relate to the output efficiency. Here the gain is only dependent on fiber length L , pump absorption $\sigma_{ap}N$ and pump IAG loss α_p , while δ_r is only dependent on fiber length L , output coupler R_{oc} and signal IAG loss α_s .

4.4.2.2 Requirements of gain – related parameters for high efficiency

Assume one-side pump, from Eq. (4.47) it is seen that

$$\eta_{slope} \propto \frac{1 - \exp[-(\sigma_{ap} N + \alpha_p)L]}{1 + \alpha_p / \sigma_{ap} N}. \quad (4.48)$$

Thus, to achieve sufficient gain and increase the output efficiency, the pump absorption coefficient needs to be much larger than the pump waveguide loss as seen from the denominator of Eq. (4.48), that is

$$\sigma_{ap} N \gg \alpha_p. \quad (4.49)$$

The physics of Eq. (4.49) is easy to interpret because only the pump absorption contributes to the gain while the pump waveguide loss adds pure loss to the gain. Usually pump IAG waveguide loss is negligible to the pump absorption coefficient in core-pumped IAG fibers and Eq. (4.49) is satisfied. For instance, the pump absorption coefficient for 1% Nd³⁺ doping (Kigre Q100) is as large as $\sim 278 \text{ m}^{-1}$ [96], while the calculated average waveguide loss for flat-top pump in Ref. [21] is up to 23 m^{-1} for the worst case with the input field totally spatial incoherent ($N_p = 1$).

Figure 4-12 demonstrates the negligible effect of pump waveguide loss to the output efficiency, in which the solid line is the simulated output power as a function of input power for the pump waveguide loss of 1.01 m^{-1} (the situation of Ref. [21]), and the dashed line shows the result when the pump waveguide loss is increased by a factor of 10. Other simulation parameters are chosen based on Ref. [21] and shown below in Table 4-1 for 1% Nd³⁺-doped Kigre Q100 laser glass. It is clearly seen that the slope efficiency has slight change even when the pump loss is increased by a factor of 10, as the ratio of pump absorption to pump waveguide loss is still very large (~ 28). Thus, generally for core-

pumped IAG fiber lasers with relatively large pump absorption coefficient ($> 10\alpha_p$), the waveguide loss of the pump has trivial impact on the output efficiency.

Table 4-1 Simulation parameters

Parameter	Value	Parameter	Value
λ_p	803 (nm)	σ_{ap}	1.4×10^{-20} (cm ⁻²)
λ_s	1054 (nm)	σ_{ep}	3.76×10^{-22} (cm ⁻²)
N	1.98×10^{-20} (cm ⁻³)	σ_{as}	7.82×10^{-22} (cm ⁻²)
R_l	1	σ_{es}	4.4×10^{-20} (cm ⁻²)
R_r (R_{oc})	0.98	α_p	1.01 m ⁻¹
L	2.6 (cm)	α_s	1.74 m ⁻¹
a	100 (μm)	τ	190 (μs)

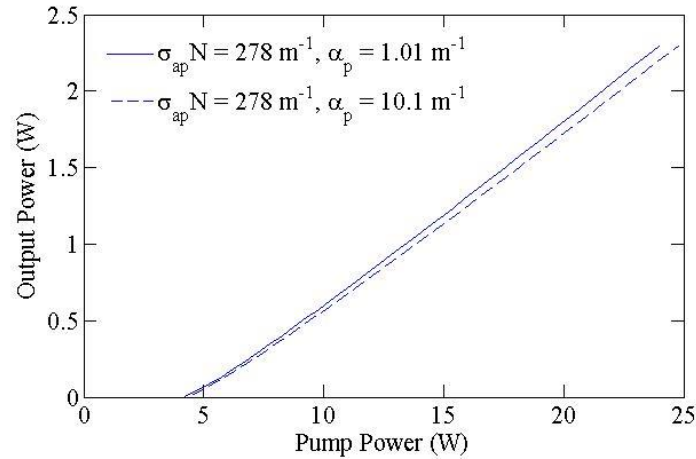


Figure 4-12 Output power as a function of input pump power for different pump waveguide losses of 1.01 m⁻¹ and 10.1 m⁻¹, while the absorption coefficient is maintained at 278 m⁻¹.

Besides Eq. (4.49), another criterion to yield high slope efficiency in Eq. (4.48) is that the fiber length should satisfy

$$L \geq L_{gain} = \frac{1}{\sigma_{ap}N + \alpha_p} \approx \frac{1}{\sigma_{ap}N}. \quad (4.50)$$

Here L_{gain} is defined as the propagation distance where pump power or gain reduces to $1/e$, or the length when the integrated gain increases to 63% of the limiting value, as shown in Figure 4-13. When fiber length is below L_{gain} , the integrated gain increases evidently with the increase of fiber length. However, when the fiber length is over L_{gain} , the integrated gain increases slowly with the increase of fiber length because the gain is almost depleted at further distance, as seen from Figure 4-13(a). Usually the fiber length should be greater than, but in the order of L_{gain} .

In summary, to achieve sufficient gain and increase the output efficiency, both Eqs. (4.49) and (4.50) need to be satisfied.

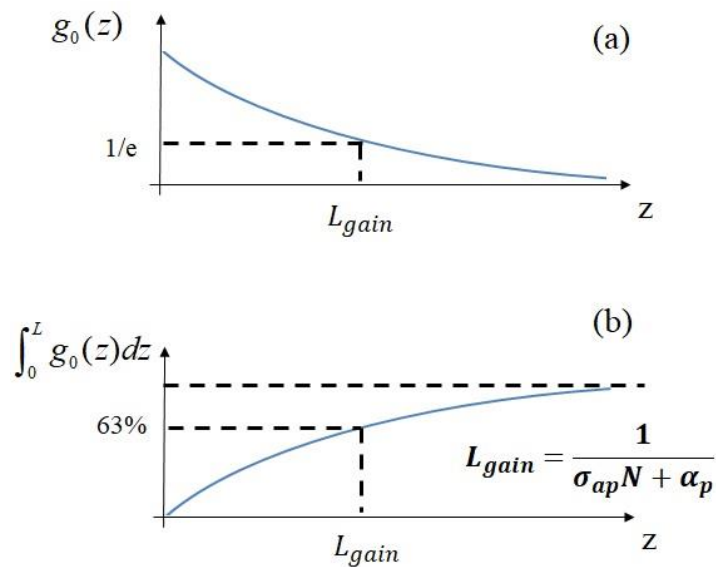


Figure 4-13 (a) Gain and (b) integrated gain evolutions along the propagation. Here L_{gain} is the defined length corresponding to $1/e$ of the gain.

4.4.2.3 Requirements of δ_r – related parameters for high efficiency

Equation (4.47) illustrates that the slope efficiency is dependent on δ_r in plane-wave lasers, and a very small δ_r ($\delta_r \ll 1$) is needed for high efficiency. This conclusion is also

valid for the core-pumped IAG fiber lasers, as demonstrated by the following simulation results.

Figure 4-14 demonstrates the effect of δ_r to the output efficiency in a core-pumped IAG fiber laser. The solid line represents the output power as a function of input pump power for the same parameters used in Ref. [21] (Table 4-1) with $\delta_i = 2\alpha_s L = 0.09$, $\delta_e = 0.02$ (for an output coupler R_{oc} of 98%), and $\delta_r = 4.5$. The calculated slope efficiency is 11% and the threshold power is 4.2 W. The dashed line is the output for the same simulation except that the signal waveguide loss is increased by a factor of 10 ($\delta_i = 0.9$) such that $\delta_r = 45$. It is seen that the slope efficiency is dramatically decreased to 1.3%, and the threshold power is increased to 8.2 W. The dotted line shows the result when the output coupler is changed to 4%, corresponding to an external mirror loss of $\delta_e = 3.22$ and $\delta_r = 0.028$. It is clearly seen that the slope efficiency is greatly increased to 61.4% which is closed to the theoretical maximal slope efficiency of $\lambda_p/\lambda_s = 76.2\%$. As a compromise, the threshold power is also increased to 18 W due to large external loss. From Figure 4-14 it is seen that large slope efficiency is achieved for δ_r much smaller than 1, which requires

$$\delta_r = \frac{\delta_i}{\delta_e} = \frac{2\alpha_s L}{-\ln R_{oc}} \ll 1. \quad (4.51)$$

Equation (4.51) limits the fiber length to

$$L \ll \frac{-\ln R_{oc}}{2\alpha_s} = L_{decay}. \quad (4.52)$$

Here the decay length L_{decay} is defined as the length at which the internal loss equals the external loss ($\delta_i = \delta_e$), or the slope efficiency is reduced to half (because $\delta_r = 1$).

For most traditional LMA fiber lasers, the signal waveguide loss is < 0.2 dB/m and the decay length is very long $L_{decay} \sim 35$ m for a 4% R_{oc} (reflection at air-glass interface).

Usually the fiber length is less than few meters such that Eq. (4.52) is satisfied. This is why most previously mentioned LMA fiber lasers could report a slope efficiency $> 60\%$. However, in IAG fiber lasers the signal waveguide loss is usually very large, such as $\alpha_s = 1.7385 \text{ m}^{-1}$ in Ref. [21] and the decay length is very small $L_{decay} < 1\text{m}$ for a 4% R_{oc} . Thus, to achieve high slope efficiency and satisfy Eq. (4.52), the fiber length in IAG fiber lasers is usually limited to much smaller than 1 m due to large signal loss. In order to have large decay length, R_{oc} needs to be small (like 4%) to increase the external loss in IAG fiber lasers. The choice of 98% R_{oc} in Ref. [21] is definitely inappropriate because the decay length is only 5.8 mm, and the 26 mm fiber length used in the experiment was too long such that Eq. (4.52) is not satisfied. This is one of the reason for the low slope efficiency in Ref. [21].

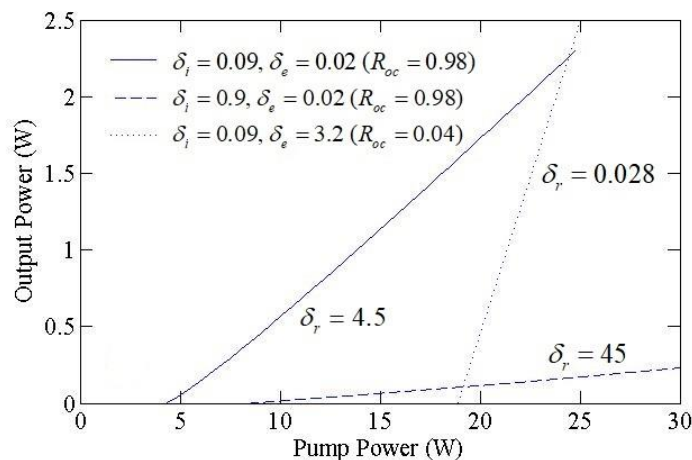


Figure 4-14 Output power as a function of input pump power at different δ_r of 4.5 (solid line), 45 (dashed line) and 0.028 (dotted line).

4.4.2.4 Requirement of fiber length after considering both gain and δ_r effects

The previous two sections separately analyze the gain- and δ_r – related parameters to increase the output efficiency. Note that the fiber length is the only one parameter that

affects both gain and δ_r . In order to achieve sufficient gain, the fiber length needs to satisfy Eq. (4.50). Meanwhile, to achieve small δ_r , the fiber length needs to satisfy Eq. (4.52). Therefore, the fiber length is limited by

$$\frac{1}{\sigma_{ap} N} \approx L_{gain} \leq L \ll L_{decay} = \frac{-\ln R_{oc}}{2\alpha_s}. \quad (4.53)$$

It is seen from Eq. (4.53) that a hidden relation is required,

$$\sigma_{ap} N \gg \frac{2\alpha_s}{-\ln R_{oc}}. \quad (4.54)$$

Here I want to emphasize an interesting finding that if Eq. (4.54) is satisfied, Eq. (4.49) is automatically satisfied when $R_{oc} \geq 0.04$ (which is usually true) as shown in the following equation

$$\sigma_{ap} N \gg \frac{2\alpha_s}{-\ln R_{oc}} = \frac{2\lambda_s^2 / \lambda_p^2 \cdot \alpha_p}{-\ln R_{oc}} \geq \alpha_p. \quad (4.55)$$

So to achieve high output efficiency, two rules need to be followed. Firstly, the laser parameters should be chosen such that Eq. (4.54) is satisfied. Secondly, the fiber length needs to satisfy Eq. (4.53). Based on these two rules, let us further analyze the low experimental efficiency issue in Ref. [21].

Figure 4-15 demonstrates the calculated slope efficiency as a function of fiber length for the parameters used in Ref. [21] (as shown in Table 4-1), except that the fiber length is varied. One feature that can be observed from Figure 4-15 is that there is an optimal fiber length $L_{opt} = 4$ mm which yields the maximal slope efficiency of 26%. This optimal fiber length should be close or in the order of L_{gain} because the gain is almost depleted for fiber length that is over L_{gain} , as illustrated previously. For small fiber length L below the optimal fiber length, the slope efficiency is increased when the fiber length is increased. This is because at small fiber length the unsaturated single-pass gain in Figure

4-13(b) increases significantly as fiber length increases, while the single-pass internal loss $\alpha_s L$ is still very small for small L such that δ_r is small. Therefore, the gain dominates the δ_r effect and the slope efficiency is increased with the increase of L . However, after the fiber length is over L_{opt} , the gain is very weak at longer distance such that the unsaturated single-pass gain in Figure 4-13(b) barely (slightly) increases (which was previously claimed in Ref. [105]). Meanwhile, the internal loss is linearly increased when L is increased and δ_r becomes very large and dominant compared to the gain. Therefore the slope efficiency is then reduced when fiber length is increased.

The red-dot in Figure 4-15 shows the simulated efficiency of the experiment in Ref. [21], with the fiber length of 26 mm. It is clearly seen that the 26 mm fiber length used in the experiment was too long such that the output efficiency was reduced. If the fiber was using an optimal length of 4 mm, the slope efficiency could be increased to 26%. However, it is found that even at the optimal fiber length the output efficiency is still very small. The reason for that is because the laser parameters ($\sigma_{ap}N$, α_s and R_{oc}) were not chosen properly in the experiment such that the L_{gain} is very close to L_{decay} , as shown by the dashed lines in Figure 4-15 with L_{gain} of 3.6 mm and L_{decay} of only 5.8 mm. Thus, Eq. (4.53) is not satisfied and the output efficiency is small.

In summary, the low efficiency of the experiment in Ref. [21] is due to the following reasons:

1. Improper choice of laser parameters (mainly because of 98% R_{oc}) such that Eq. (4.54) is not satisfied. It is usually desired to choose small R_{oc} because of large signal waveguide loss.
2. The fiber length was too long and not optimized such that Eq. (4.53) is not satisfied.

3. The use of cladding pumping is not efficient in IAG fiber laser, as demonstrated in Section 4.2.2. Core pumping should be used instead.

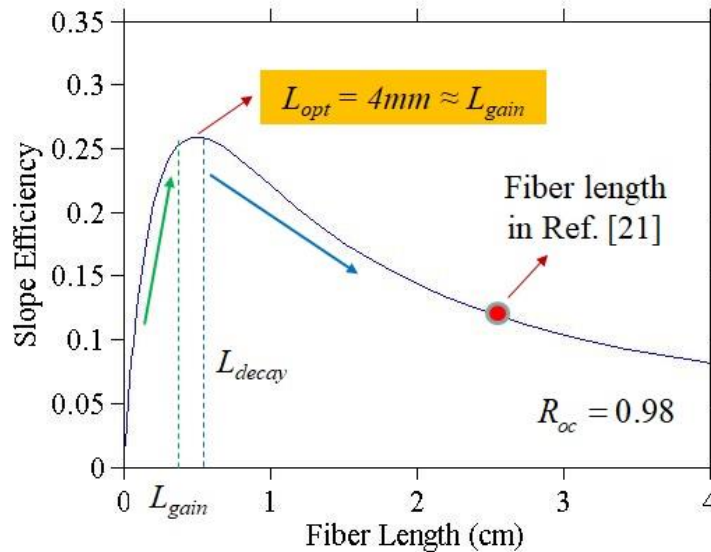


Figure 4-15 Slope efficiency as a function of fiber length for the output coupler of 98%. The simulation parameters are from Table 4-1 (Ref. [21]) except the fiber length is varied.

4.4.2.5 The requirement of output coupler for both high efficiency and low threshold power

As discussed in the last section, high slope efficiency can be achieved when the laser parameters satisfy Eq. (4.53). However, all the previous analysis does not consider the power threshold which is also important for the laser design. This section will focus on the requirement of output coupler that yields both high slope efficiency and low threshold power.

Figure 4-16(a) shows the slope efficiency as a function of fiber length L for different output couplers R_{oc} , using the simulation parameters in Table 4-1 except the fiber length is varied. Several features can be observed from Figure 4-16(a). The first feature is that for each R_{oc} , there is an optimal fiber length L_{opt} corresponding to the maximum slope

efficiency η_{max} , and this L_{opt} is close or in the order of L_{gain} , which was explained previously in Section 4.4.2.4. The second feature is that the slope efficiency is reduced when R_{oc} is increased, which was explained in the previous section as δ_r is increased when R_{oc} is larger. The third feature seen from Figure 4-16(a) is that the optimal fiber length L_{opt} shifts to larger value when the output coupler R_{oc} is decreased. This is because δ_r is very small for small output coupler. To make δ_r start to dominate the gain effect (which corresponds to the turn point of the slope efficiency, or maximal slope efficiency), a longer fiber length is required to ensure large δ_r and therefore L_{opt} is larger. The relationship between L_{opt} and R_{oc} is illustrated as the dashed line in Figure 4-16(c). The solid line in Figure 4-16(c) illustrates the maximum slope efficiency as a function of R_{oc} . It is seen that for $R_{oc} = 0.04$, the slope efficiency can be as high as 61.4% with an optimal fiber length of 1.83 cm.

Figure 4-16(b) plots the corresponding threshold powers as a function of fiber length for different R_{oc} . Several features can be observed from Figure 4-16(b). At first, there is an optimal fiber length L_{2_opt} which minimizes the threshold power. For a fiber length below L_{2_opt} , the threshold power is decreased with an increased fiber length, which can be seen by Eq. (4.35). An explanation is that the unsaturated single-pass gain in Eq. (4.34) increases more effectively compared to the internal loss for short fiber length. For longer fiber length, the unsaturated single-pass gain does not increase further as the pump is almost depleted at longer distance, while the increase of internal loss becomes more dominant when L is increased. As a result, more pump power is needed to compensate the roundtrip loss. The second feature seen from Figure 4-16(b) is that the threshold power is decreased for increased R_{oc} , which is evident as the external loss is reduced. Figure 4-16(d) illustrates the minimum threshold power as a function of R_{oc} (solid line). Another feature

seen from Figure 4-16(b) is that L_{2_opt} is increased when R_{oc} becomes smaller, with the plot shown as the dashed line in Figure 4-16(d). This can be explained in the same way as for the slope efficiency in Figure 4-16(a), or by the following expression of L_{2_opt} that is derived from Eq. (4.35) by setting $dP_p^+(0)^{th} / dL = 0$

$$\frac{\exp\left[(\sigma_{ap}N + \alpha_p)L_{2_opt}\right] - 1}{\sigma_{ap}N + \alpha_p} - L_{2_opt} = -\frac{\frac{1}{2} \ln R_l R_r}{\sigma_{as}N + \alpha_s}. \quad (4.56)$$

Another interesting observation from Figure 4-16(c) is that the maximum slope efficiency dramatically increases when the output coupler is decreased from 0.98 to 0.7, while the threshold power does not increase too much, as seen from Figure 4-16(b). For the output coupler smaller than 0.3, the maximum slope efficiency only slightly increases with reduced R_{oc} , while the threshold power, on the other way, increases significantly with reduced R_{oc} . This provides us the guideline to choose an appropriate output coupler that is within 0.3 – 0.7 to satisfy both high output efficiency and low threshold power.

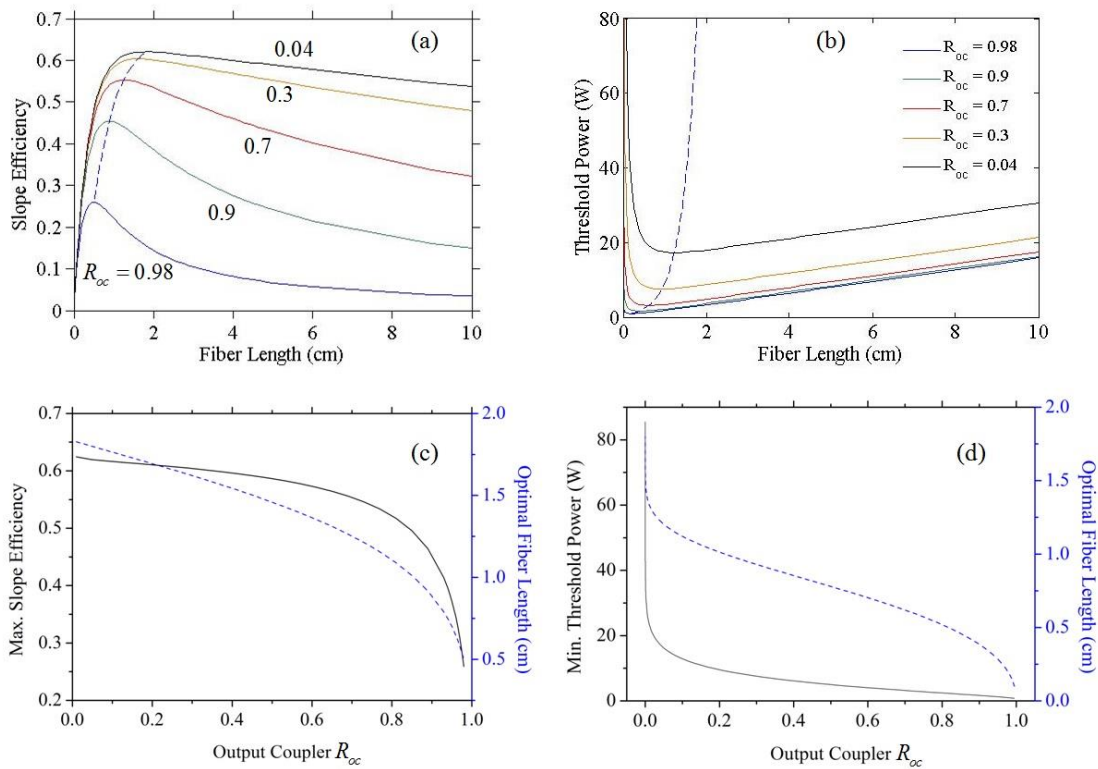


Figure 4-16 (a) Slope efficiency and (b) corresponding threshold power as a function of fiber length for different output couplers (solid lines), while the dashed lines represents the locus of optimal output couplers. (c) Maximum slope efficiency (solid line) and corresponding optimal fiber length L_{opt} (dashed line) as a function of output coupler R_{oc} . (d) Minimum threshold power (solid line) and corresponding optimal fiber length L_{2_opt} (dashed line) as a function of output coupler R_{oc} .

4.4.3 Design guidelines to improve the output efficiency in core-pumped index-antiguided fiber lasers

Based on the analysis from the previous section, we can create design guidelines to improve laser output efficiency in core-pumped IAG fiber lasers. The overall goal is to satisfy Eq. (4.53), or separately satisfy Eqs. (4.52) and (4.50), with the design details illustrated below.

For a core-pumped IAG fiber laser system with a fixed signal waveguide loss α_s , the design should first satisfy Eq. (4.52). As a long fiber length is desired for large output

power, it is preferred to choose a small R_{oc} such that L_{decay} is very large. For a small 4% coupler with external loss of $\delta_e = 3.22$, the decay length is $L_{decay} = 1.6/\alpha_s$. In order to design meter-scale fiber lasers, the signal IAG loss should be maintained much smaller than 1/m, which can be achieved by increasing the core size or index difference as illustrated by Eq. (4.6). After we obtain L_{decay} , we can pre-determine the fiber length L to satisfy $L \ll L_{decay}$. It is known that if we choose $L = L_{decay}$, the slope efficiency drops to half as $\delta_r = 1$. For a decent efficiency of 80% (here the real slope efficiency should be further reduced to $80\% \cdot \lambda_p/\lambda_s$ as shown in (4.47)), δ_r should be as small as 0.25 and the fiber length is limited to $L = 0.25L_{decay} = 0.4/\alpha_s$.

Based on the pre-determined L we can choose a proper doping density N and pump absorption cross-section σ_{ap} such that the pump absorption satisfies Eq. (4.50). The pump absorption can be chosen close or in the order of $1/L$ (usually $2/L - 4/L$ as demonstrated in Figure 4-16(c)). Meanwhile, the pump absorption should be automatically much larger than the pump IAG loss, as illustrated by Eq. (4.55).

After pump absorption coefficient is determined, an optimal fiber length can be calculated to yield the maximal efficiency, as shown in Figure 4-16(a). Up until now, large output efficiency can be achieved if following the above design guidelines.

Note that the threshold power also needs to be considered during the design. A proper tuning of the output coupler (like 0.3 – 0.7 in Figure 4-16(c)) is necessary to maintain both high efficiency and low threshold power.

4.5 Power limit

It is essential to understand what is the power limit for IAG fiber lasers. From Section 2.3 we have introduced the power thresholds to induce nonlinear, thermal and surface damage effects. Now let us roughly estimate what is the power limit for IAG fiber lasers based on Section 2.3. Take the Nd³⁺-doped fiber from Ref. [21] as an example. The core and cladding diameters are 200 and 340 μm, respectively. Let us first consider power threshold from thermal perspective. From Eq. (2.6) it is seen that the threshold of heat load per unit length is

$$q_{fracture} = \frac{4\pi R_m}{1 - \frac{a^2}{2b^2}} \approx 15R_m. \quad (4.57)$$

For normal silica with $R_m > 2500$ W/m, the above limit is ~ 37500 W/m. For Kigre Q-100 glass used in the reference, the heat load limit is > 10000 W/m [106], which is a very large value compared to other thermal effects (as shown in the following paragraphs). Thus, the heat-induced mechanical damage is usually not considered in high-power IAG fiber lasers.

The heat load limit for thermal lens effect can be calculated from Eq. (2.4), which shows that

$$q_{lens} = \frac{\pi\kappa\lambda_s^2}{2a^2 dn/dT} < 100 \text{ W/m}, \quad \text{for } a > 50\mu\text{m}. \quad (4.58)$$

Thus, the effect of thermal lensing is obvious for IAG fiber lasers due to large core size. Fortunately, the Kigre Q-100 laser glass is athermal, which is achieved by designing appropriate positive thermal expansion coefficient to compensate the negative thermo-optic coefficient of $dn/dT = -4.6 \times 10^{-6} / \text{C}$ [106].

The heat load limit for the melting of core and damage of polymer coating can be calculated from Eq. (2.16). Figure 4-17(a) plots the highest polymer temperature (referred

to the coolant temperature T_c) at the cladding-coating interface $r = b$, as a function of total heat transfer coefficient (including both convective and radiative heat transfer coefficients) for different heat load of 10, 50, 100, 200 and 500 W/m. During the simulation, the thermal conductivity of the core and cladding is 0.82 W/m/K [106] and the thermal conductivity of the polymer coating is assumed to be 0.2 W/m/K [52]. The dashed line indicates 150 C which is roughly the limit temperature for most of the polymers. Heat load should be chosen such that the polymer temperature is below the dashed line. As the Q-100 Kigre glass has a very low melting temperature of 432 C [106], the highest temperature in the core (at $r = 0$) needs to be considered, which is plotted in Figure 4-17(b). It is seen from Figure 4-17 that the heat load limit for core melting is always higher than the heat load for polymer damage. Thus, we only need to consider the heat load limit for polymer damage. It is seen from Figure 4-17 that in order to push the heat load over 100 W/m, the heat transfer coefficient needs to be over 600 W/m²/K. For the heat load of 500 W/m, the heat transfer coefficient needs to be greater than 4000 W/m²/K. For a forced liquid cooling with $h = 10000$ W/m²/K, the limit of heat load is ~ 850 W/m, which is very promising to push the IAG fiber lasers to kW scale for meter-scale fiber length.

For a fixed core size, the polymer temperature is also dependent on cladding diameter and coating thickness. Figure 4-18(a) illustrates the polymer temperature (referred to the coolant temperature T_c) as a function of total heat transfer coefficient for different cladding diameter of 340, 400 and 500 μm . Figure 4-18(b) illustrates the polymer temperature as a function of total heat transfer coefficient for different coating thickness of 20, 50 and 70 μm . From Figure 4-18 it is seen that larger cladding and smaller coating thickness is preferred to increase the heat load.

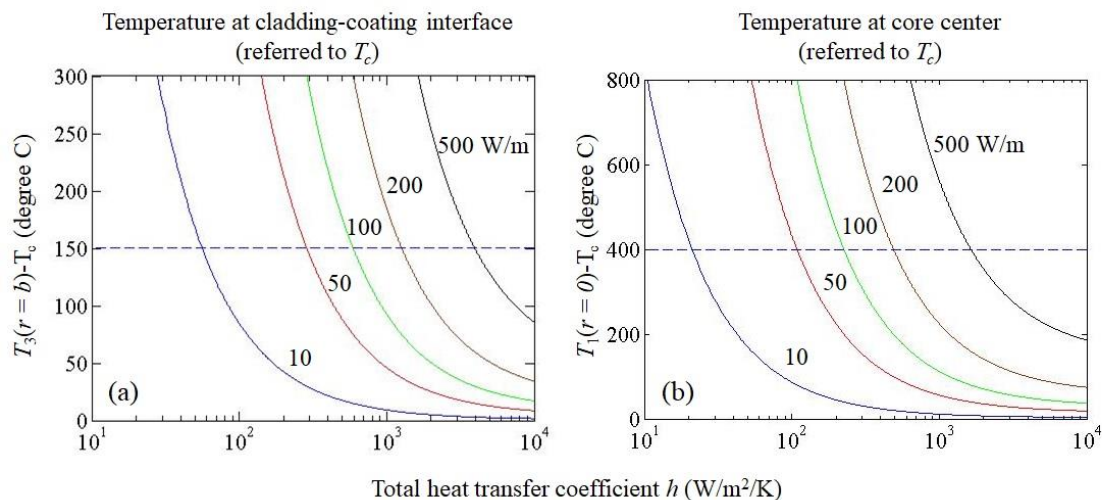


Figure 4-17 (a) Polymer temperature (referred to coolant temperature T_c) and (b) Temperature at core center (referred to coolant temperature T_c) as a function of total heat transfer coefficient h , for different heat load of 10, 50, 100, 200 and 500 W/m. The core and cladding diameters are 200 and 340 μm , respectively. The coating thickness is 20 μm .

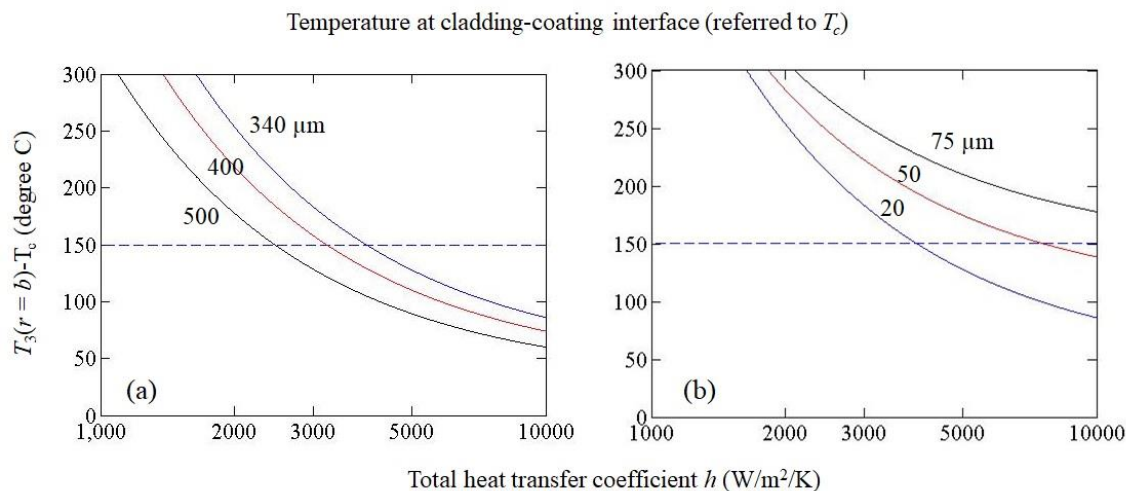


Figure 4-18 Polymer temperature (referred to coolant temperature T_c) as a function of total heat transfer coefficient h for (a) different cladding diameter of 340, 400 and 500 μm (with core diameter is 200 μm and the coating thickness is 20 μm) and (b) different coating thickness of 20, 50 and 75 μm (with core and cladding diameters of 200 and 340 μm).

From the previous analysis we see that a heat load of ~ 850 W/m can be achieved if using a forced liquid cooling with $h = 10000$ W/m²/K. Given a conservative estimation, let us assume there is a heat load limit of 500 W/m for IAG fiber lasers. The maximum input pump power for one-side core-pumped IAG fiber lasers could be calculated from

$$P_p(0) = \frac{q(0)}{\eta_{heat}\alpha}. \quad (4.59)$$

Here $P_p(0)$ and $q(0)$ are the pump power and heat load at the input end. η_{heat} is the heat deposition efficiency. α denotes the pump decay coefficient which is the combination of pump absorption coefficient, pump waveguide loss coefficient and scattering loss coefficient. For core-pumped IAG fiber lasers, the largest heat load is usually at the input end and the limit of input pump power could then be obtained from the limit of heat load.

As the extracted power per unit length is proportional to the heat load per unit length, long fiber (meter scale) is preferred to yield large output power. Usually a fiber length of > 0.5 m is required. However, from Section 4.4.3 it is seen that the fiber length needs to be chosen such that $L < 0.4/\alpha_s$ for an output coupler of 4%. Due to the large signal IAG loss (like 1.74 m⁻¹ in Ref. [21]), the fiber length is usually limited within 1 m in IAG fiber lasers. Suppose the fiber length is 0.5 m, the corresponding pump absorption coefficient should be $\alpha \sim 2$ m⁻¹. Here we assume the pump absorption coefficient is larger than other pump waveguide loss and scattering loss. The calculated limit of pump power is $P_p(0) \sim 1$ kW, which limits the output power under kW scale. In fact, from Chapter 5 it is seen that the maximum extraction efficiency of single fundamental mode in IAG fiber lasers is $\sim 50\%$ (the quantum defect of λ_p/λ_s is not included). Thus, the real output power will be less than $P_p(0)*50%*\lambda_p/\lambda_s \sim 380$ W, for a heat load of 500 W/m and $\alpha \sim 2$ m⁻¹.

In addition to thermal effects, surface damage will also limit the input pump power. However, the estimated damage power is very high ($> 7 \times 10^5$ W for a core size of 100 μm and intensity threshold of 10 $\text{W}/\mu\text{m}^2$ [49]) for IAG fiber lasers with large core size. Thus, surface damage effect could be neglected in IAG fiber lasers.

Besides above analysis of power limit induced by thermal effects and surface damage, the input pump power also needs to be chosen such that the SBS and SRS nonlinear effects will not occur. The SBS threshold power could be estimated from Eq. (2.1), which is > 3 kW for the worst situation of 1 m effective fiber length, small core size of 100 μm and no inclusion of pump linewidth. The SRS threshold power could be estimated from (2.3), which is usually $> 10^6$ W. Compared to the limit of pump power by thermal effects (~ 1 kW), the SBS and SRS effects are not evident for large-core IAG fiber lasers.

In conclusion, after considering the thermal, nonlinear and surface damage effects, the estimated maximal pump power using Kigre Q-100 Nd^{3+} -doped fiber is ~ 1 kW for a pump absorption coefficient of 2 m^{-1} , which corresponds to an output power (single fundamental mode) < 380 W. The pump power is limited by the short fiber length, as high output efficiency requires shorter length for high-loss fiber lasers. A higher power might be achieved if better cooling is used or the coating is removed such that higher heat load is allowed.

4.6 Summary

IAG fibers intrinsically introduce a waveguide loss ratio of 2.54 between FM and 1st HOM for large index-antiguiding, which is different from IAG planar waveguides that provide a loss ratio of 4. Due to the specialty of IAG waveguides, different pumping schemes need to be analyzed. Side pumping technique was widely used in most of the experimental work because it is not limited by the waveguide loss and low pump efficiency (due to index-antiguiding effect) as in end pumping scheme. However, side pumping is not efficient as it will suffer reflection loss at the waveguide interfaces. Moreover, it requires complicated setup and straight fibers, which makes it difficult to implement for real products. End pumping should yield higher efficiency than side pumping. However, it was believed that the waveguide loss and index-antiguiding effect will greatly affect the pump efficiency. In this section, the output efficiency between two common end pumping techniques – core and cladding pumping is numerically analyzed, which shows that core pumping will be appropriate for IAG lasers since in cladding pumping, most of the cladding power will be trapped and unable to effectively pass through the core due to both index-antiguiding effect and large core size. Therefore it is always recommended to use core pumping instead of cladding pumping for IAG fiber lasers. Moreover, the large core size is beneficial for pump coupling, making core pumping applicable in IAG fiber lasers.

Maximum extraction efficiency of fundamentally single mode in uniformly side-pumped IAG fiber lasers are calculated for different single-pass gains and losses, showing similar property as for homogeneous plane-wave lasers. Very high extraction efficiency is achievable with very low internal loss and large output coupler, with the maximal value approaching to unity at the limit. The output characteristics of fundamentally single mode

in core-pumped IAG fibers is also investigated, and the parameters affecting the output efficiency are carefully analyzed. To achieve high output efficiency, the gain length $L_{gain} = 1/\sigma_{ap}N$ should be much smaller than the decay length $L_{decay} = -\ln R_{oc}/2\alpha_s$, and the fiber length should be chosen such that $L_{gain} \leq L \ll L_{decay}$. The reason for the low efficiency in the published Ref. [21] is due to the failure of satisfying the above conditions. A detailed design procedure for core-pumped IAG fiber lasers is also provided to improve the output efficiency.

In addition, the power limit of IAG fiber lasers is investigated for the specific Kigre Q-100 Nd³⁺-doped fiber laser, showing that the nonlinear and surface damage effects are insignificant compared to thermal effects. Within the thermal effects, thermal lens effect is the main limit to the output power due to the large core size. Thus, athermal laser glass is desired to reduce this effect, and fortunately Kigre laser glass is designed to be athermal. As a result, the main limit to the power is due to the melting of polymer coating. Due to the short fiber length (< 1 m) in general IAG fiber lasers, the maximal calculated allowed pump power (to avoid the polymer melting) is ~ 1 kW for a pump absorption coefficient of 2 m⁻¹. Corresponding output power is limited less than 380 W.

CHAPTER 5 TRANSVERSE MODE COMPETITION IN INDEX-ANTIGUIDED FIBER LASERS

In the previous chapter we have comprehensively analyzed the output efficiency of fundamentally single mode in both uniformly side-pumped and core-pumped IAG fiber lasers. However, the previous analysis only considers FM operation and does not include HOMs oscillation. Due to the experimental observation of HOM oscillation in an IAG slab laser, the robustness of single-mode needs to be studied. In this chapter we will provide a thorough analysis of single mode capability in both uniformly side-pumped and core-pumped IAG fiber lasers. Specifically, the oscillator models with transverse mode competition are given for both pumping schemes. The gain oscillation threshold of the first HOM will be calculated with a semi-analytical method, along with the characteristics of the threshold analyzed. Moreover, the calculated HOM threshold in uniformly side-pumped IAG fiber lasers will be applied to one published experimental work to validate the numerical model. In addition, the output characteristics of single fundamental mode (only FM oscillates in multimode lasers) will be completely investigated.

5.1 Transverse mode competition in uniformly side-pumped index-antiguided fiber lasers

In this section, we will at first provide theoretical model and comprehensive analysis of transverse mode competition in uniformly side-pumped IAG fiber lasers. Both the characteristics of the 1st HOM threshold and the output of the single fundamental mode are investigated. The more complicated model for core-pumped index-antiguided fiber lasers will be discussed in Section 5.3.

5.1.1 Oscillator model

For uniformly side-pumped IAG fiber lasers, the oscillator model is slightly changed from Eq. (3.43) by replacing the planar modal profiles $f_i(x)$ to fiber modal profiles $f_i(r, \theta)$. These modal profiles are sometimes called power filling distributions, which are used to relate the whole transverse power to local intensities. If we still consider two-mode competition (LP₀₁ and LP₁₁), the governing equations for the oscillator model of IAG fiber laser are

$$\frac{dI_n^+}{dz} = g_0 I_n^+ \int_0^{2\pi} \int_0^a \frac{f_n(r, \theta)}{1 + A_{core} \sum_{i=1}^2 f_i(r, \theta) (I_i^+ + c_i / I_i^+)} r dr d\theta - \alpha_n I_n^+. \quad n=1, 2 \quad (5.1)$$

where I_n^+ is the forward-propagating normalized intensity of n^{th} mode. A_{core} is the area of the core with a radius of a . $c_n = [I_n^+(0)]^2 / R_l = R_r [I_n^+(L)]^2$ are mode-specific constants, and the normalized modal profiles are

$$f_1(r, \theta) = f_1(r) = \frac{|E_{01}(r)|^2}{\int_0^{2\pi} \int_0^\infty |E_{01}(r)|^2 r dr d\theta} = \frac{|E_{01}(r)|^2}{2\pi \int_0^\infty |E_{01}(r)|^2 r dr}, \quad (5.2)$$

$$f_2(r, \theta) = \frac{|E_{11}(r)|^2}{2\pi \int_0^\infty |E_{11}(r)|^2 r dr}.$$

with

$$E_{01}(r) = \begin{cases} J_0(\tilde{u}_{01} r / a), & r \leq a \\ \frac{J_0(\tilde{u}_{01})}{K_0(\tilde{w}_{01})} K_0(\tilde{w}_{01} r / a), & r > a \end{cases} \quad (5.3)$$

$$E_{11}(r) = \begin{cases} J_1(\tilde{u}_{11} r / a), & r \leq a \\ \frac{J_1(\tilde{u}_{11})}{K_1(\tilde{w}_{11})} K_1(\tilde{w}_{11} r / a), & r > a \end{cases}$$

For IAG waveguides that generally have large ΔN , we could approximate $\tilde{u}_{01} \approx j_{01} = 2.4048$ and $\tilde{u}_{11} \approx j_{11} = 3.8317$, and the distributive losses could be estimated from Eq. (4.6) with the loss ratio of $\alpha_2 / \alpha_1 \approx 2.54$.

5.1.2 Regions of single-fundamental-mode operation

Like Eq. (3.47), the gain oscillation threshold of LP₁₁ mode could be solved from the following equation

$$g_2^{th} \int_0^L \left(\int_0^{2\pi} \int_0^a \frac{f_2(r, \theta)}{1 + A_{core} f_1(r, \theta) (I_1^{'+} + c_1 / I_1^{'+})} r dr d\theta \right) dz = \alpha_2 L - \frac{1}{2} \ln R_t R_r. \quad (5.4)$$

Figure 5-1 demonstrates the gain threshold ratio g_2^{th} / g_1^{th} of LP₁₁ to LP₀₁ mode as a function of single-pass distributed loss (of FM) and output coupler. Similar to IAG planar waveguides shown in Figure 3-11, the gain threshold ratio becomes large in the top-right region where the output coupling loss T is small or the distributed loss of FM is large.

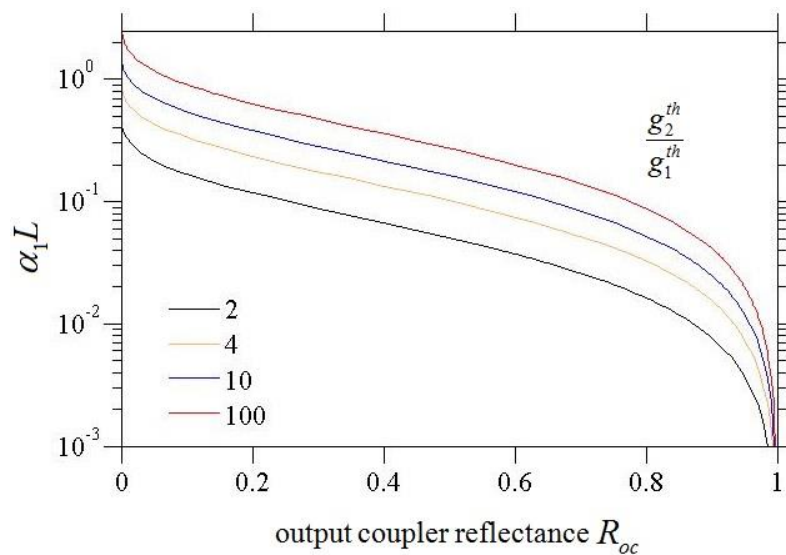


Figure 5-1 Contour plot of gain threshold ratio g_2^{th} / g_1^{th} , as a function of single-pass loss $\alpha_1 L$ of the fundamental mode (logarithmic scale) and output coupler R_{oc} (linear scale), in uniformly side-pumped IAG fiber lasers.

5.1.3 Extraction efficiency of single fundamental mode

After obtaining the 1st HOM gain threshold, the maximal extraction efficiency of single fundamental mode η_{SM}^{\max} as a function of R_{opt} could be calculated for different pairs of single-pass gains and losses, which is shown in Figure 5-2. Similar to IAG planar waveguide (Figure 3-13(a)), the maximal extraction efficiency of single fundamental mode in IAG fiber waveguide is also suppressed due to transverse mode competition for large value of g_0 / α_1 . Moreover, the calculated absolute maximal extraction efficiency H_{SM}^{\max} is 0.499 for IAG fiber waveguides, compared to 0.67 for IAG planar waveguides. The derivation for H_{SM}^{\max} in IAG fiber lasers is the same as in IAG planar waveguide lasers, which is shown as follows. Similar to Eq. (3.49), the equation for fiber waveguides is

$$g_2^{th} \int_0^L \left(\int_0^{2\pi} \int_0^a \frac{kf_1(r, \theta) - f_2(r, \theta)}{1 + A_{core} f_1(r, \theta) (I_1^+ + c_1 / I_1^+)} r dr d\theta \right) dz = -\frac{(k-1)}{2} \ln R_l R_r = -\frac{(k-1)}{2} \ln R_{oc}. \quad (5.5)$$

At the limit of low loss $\alpha_1 L \rightarrow 0$ and weak coupling $R_r \rightarrow 1$ where $I_1^+ \approx I_1^-$ and $-\ln R_{oc} \approx 1 - R_{oc}$, the above equation is further reduced to

$$g_2^{th} L \int_0^{2\pi} \int_0^a \frac{kf_1(r, \theta) - f_2(r, \theta)}{1 + 2A_{core} f_1(r, \theta) I_1^+} r dr d\theta = \frac{(k-1)}{2} (1 - R_{oc}). \quad (5.6)$$

Since the right-hand side of Eq. (5.6) is close to 0, we have $2A_{core} f_1(r, \theta) I_1^+ \gg 1$ and Eq.

(5.6) is modified to

$$\frac{g_2^{th} L}{2I_1^+} \int_0^{2\pi} \int_0^a \frac{kf_1(r, \theta) - f_2(r, \theta)}{A_{core} f_1(r, \theta)} r dr d\theta = \frac{g_2^{th} L}{2I_1^+} (k - 1.7714) = \frac{(k-1)}{2} (1 - R_{oc}). \quad (5.7)$$

From which the absolute maximal extraction efficiency is expressed as

$$H_{SM}^{\max} = \frac{I_1^+ (1 - R_{oc})}{g_2^{th} L} = \frac{k - 1.7714}{k - 1}. \quad (5.8)$$

For IAG fibers with $k = 2.54$, H_{SM}^{\max} is 0.499.

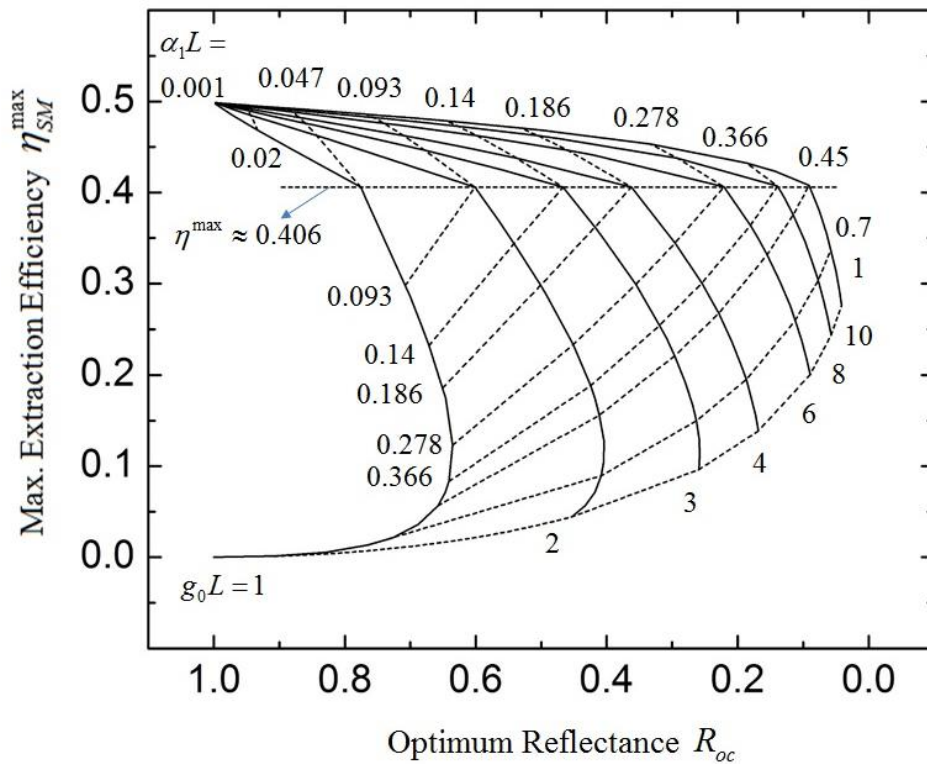


Figure 5-2 Maximal extraction efficiency of the single fundamental mode in uniformly side-pumped IAG fiber lasers (η_{SM}^{\max}) as a function of optimal output coupler reflectance R_{opt} , for various single-pass gains (solid lines) and distributed losses (dash lines).

In addition, as is similar to IAG planar waveguides, the kink points in IAG fiber lasers also satisfy the scaling law under weak coupling condition. Table 5-1 shows the solution of the kink points in IAG fiber lasers, from which it is seen that the scaling law is roughly satisfied, with a nearly fixed g_0 / α_1 value of ~ 21 and $-\ln R_{opt} / \alpha_1 L$ value of ~ 5.4 observed. Moreover, the optimum extraction efficiencies of the single mode at the kink points are nearly the same, with a value of ~ 0.406 , which is smaller than the value of 0.58 in IAG planar waveguide lasers.

Table 5-1 Solution of the kink points in IAG fiber lasers

$\alpha_1 L$	$g_0 L$	R_{opt}	η_{SM}^{max}	g_0/α_1	$-\ln(R_{opt})/\alpha_1 L$
0.047	1	0.775	0.406	21.433	5.453
0.093	2	0.601	0.406	21.435	5.452
0.140	3	0.466	0.406	21.444	5.451
0.186	4	0.362	0.406	21.466	5.448
0.278	6	0.221	0.406	21.584	5.430
0.366	8	0.139	0.407	21.841	5.394
0.449	10	0.091	0.408	22.254	5.338

5.2 Model validation from published experimental work

Let us take a look at one published experimental work [22] and try to use the previous theory to predict the threshold power of the 1st HOM (as shown in Eq. (5.4)). Although the coupling efficiency of side pumping is unknown, we could assume a fixed coupling efficiency for the same core diameter. The relationship between the pump power and the unsaturated gain could be derived from Eq. (4.32) by assuming a constant pump power P_p along the propagation direction

$$g_0 L = NL \left[\frac{\eta_c P_p \sigma_{ap} \pi \Gamma_p}{h\nu_p} (\sigma_{as} + \sigma_{es}) - \sigma_{as} \right]. \quad (5.9)$$

Here a pump coupling coefficient η_c is added in Eq. (5.9) and could be fitted based on the three pairs of measured threshold powers and theoretical threshold gains ($P_p^{th}, g_1^{th} L$) of the FM at output couplers of 37%, 45% and 90%. In fact, the parameter N is also unknown. Therefore another scaling parameter is added on N . For simplicity, there would be simply

only two fitting parameters to connect the threshold powers and threshold gains, demonstrated below as

$$g_0L = AP_p + B. \quad (5.10)$$

which illustrates that the gain has a linear relationship to the input pump power. Note that the pump coupling coefficient could be assumed fixed for the same core diameter, but different for different core diameters. Then the threshold power of the 1st HOM could be derived from the theoretical calculated threshold gain of the 1st HOM $g_2^{th}L$ and Eq. (5.10). Table 5-2 shows the calculated threshold powers of the 1st HOM for the experimental result from Ref. [22]. In all of the simulations, a signal loss of 0.08 m^{-1} is also considered for Kigre Q100 glass [106].

It is seen from Table 5-2 that at the core width of $100 \text{ }\mu\text{m}$, there are no HOM oscillations (the threshold is infinite) for all three output couplers at 37%, 45% and 90%, which corresponds well with the small measured value of M^2 at 50 W. For the $200 \text{ }\mu\text{m}$ core, there is no HOM at 90% coupler which corresponds to a small M^2 . The calculated HOM threshold powers are 54.2 W and 52.8 W for 37% and 45% couplers, respectively. The measured values of M^2 at 50 W were also small as the pump power (50 W) was below the thresholds. For the core width of $300 \text{ }\mu\text{m}$, the calculated HOM threshold powers were 33.7 W and 29.2 W for the output coupler of 37% and 45%, respectively. Then there would already exist the oscillation of HOM at the pump power of 50 W. This could be partially verified by the very high value of measured M^2 in the table. At the output coupler of 97% (there might be a mistake in the paper as the author might use the 90% output coupler), there is no HOM oscillation which also agrees well with the low measured value of M^2 . Although there is no direct measurement of the threshold power of the HOM, the measured

M^2 value is still a good indicator of the existence of HOMs, and the theoretical model seems to work well to predict the threshold power of the HOM.

Table 5-2 Calculated threshold power of the 1st HOM for the data from Ref. [22]

Core Width (μm)	Coupler	M^2_x (at 50W)	M^2_y (at 50W)	FM Threshold Power (W)	FM Threshold Gain $g_1^{th}L$	1 st HOM Threshold Power (W)	1 st HOM Threshold Gain $g_1^{th}L$
100	37%	1.60	1.44	26	1.06	inf	inf
	45%	1.45	1.44	21	0.96	inf	inf
	90%	1.34	1.34	12	0.61	inf	inf
200	37%	1.44	1.35	31	0.57	54	1.10
	45%	1.31	1.31	27	0.47	53	1.07
	90%	1.25	1.23	12	0.13	inf	inf
300	37%	1.89	1.95	27	0.52	34	0.64
	45%	1.60	1.71	25	0.42	30	0.54
	97%	1.32	1.35	7	0.08	inf	inf

5.3 Transverse mode competition in core-pumped index-antiguidded fiber lasers

In Section 5.1, the single mode capability in uniformly side-pumped IAG fiber lasers is investigated. Oscillator model including transverse mode competition due to spatial hole burning is proposed. A simple quasi-analytical method is used to calculate the gain oscillation threshold of the 1st HOM. The dependence of single-mode operation on single-pass internal loss (of FM) and output coupler is analyzed. The maximal output extraction efficiency in the region of single fundamental mode is calculated as a function of optimal output coupler at different pairs of single-pass gains and losses.

Compared to side pumping, core pumping is more favorable due to its high efficiency and simple pumping scheme. In this section, we would investigate the single

mode capability in core-pumped IAG fiber lasers. At first, a more complicated oscillator model for core-pumped IAG fiber lasers is provided. Then the gain threshold of the 1st HOM is calculated using the same semi-analytical method proposed in the last chapter, and the relation of single-mode robustness to output coupler and single-pass internal loss is analyzed. Finally, the output characteristics of single fundamental mode is investigated and compared to the results with side pumping scheme.

5.3.1 Oscillator model

Consider multiple competitive transverse modes with the same frequency ν_s , the governing equations for fundamentally signal mode (Eqs. (4.19) - (4.21)) will be changed to

$$\frac{N_2(r, \theta, z)}{N} \approx \frac{\frac{(P_p^+(z) + P_p^-(z))\sigma_{ap}\Gamma_p(r, \theta)}{h\nu_p} + \frac{\sum_i (P_i^+(z) + P_i^-(z))\sigma_{as}\Gamma_i(r, \theta)}{h\nu_s}}{\frac{(P_p^+(z) + P_p^-(z))(\sigma_{ap} + \sigma_{ep})\Gamma_p(r, \theta)}{h\nu_p} + \frac{1}{\tau} + \frac{\sum_i (P_i^+(z) + P_i^-(z))(\sigma_{as} + \sigma_{es})\Gamma_i(r, \theta)}{h\nu_s}}, \quad (5.11)$$

$$\pm \frac{dP_p^\pm(z)}{dz} = \left\{ \int_0^{2\pi} \int_0^a [(\sigma_{ap} + \sigma_{ep})N_2(r, \theta, z) - \sigma_{ap}N(r, \theta, z)] \Gamma_p(r, \theta) r dr d\theta \right\} P_p^\pm(z) - \alpha_p P_p^\pm(z), \quad (5.12)$$

$$\pm \frac{dP_i^\pm(z)}{dz} = \left\{ \int_0^{2\pi} \int_0^a [(\sigma_{as} + \sigma_{es})N_2(r, \theta, z) - \sigma_{as}N(r, \theta, z)] \Gamma_i(r, \theta) r dr d\theta \right\} P_i^\pm(z) - \alpha_i P_i^\pm(z). \quad (5.13)$$

where P_i^+ and P_i^- are the forward and backward signal powers of i^{th} transverse signal mode. $\Gamma_i(r, \theta)$ is the power filling distribution of i^{th} transverse signal mode. It needs to be noted that the coupling of signal modes is not considered in above equations. After the same derivation implemented in Section 4.4 with the assumption of $N_2 \ll N$, Eqs. (5.11)

- (5.13) could be reduced to

$$\frac{dP_i^+(z)}{dz} = \left[\int_0^{2\pi} \int_0^a \left[\frac{g_0(z)}{1 + \sum_i \Gamma_i(r, \theta) A_{core}(P_i^+(z) + c_i / P_i^+(z)) / P_{sat}} \right] \Gamma_i(r, \theta) r dr d\theta \right] P_i^+(z) - \alpha_i P_i^+(z). \quad (5.14)$$

which subjects to the boundary conditions

$$c_i = P_i^+(0)^2 / R_l = R_r P_i^+(L)^2. \quad (5.15)$$

where c_i is a constant related to the i^{th} single mode. Consider the pump is injected from the left end and no pump light is reflected or injected from the right end, the pump power and the unsaturated signal gain will have the same expression of Eq. (4.25) and Eq. (4.32). Thus, the signal powers as well as the gain oscillation thresholds of HOMs could be calculated from Eqs. (5.14) and (5.15).

5.3.2 The gain oscillation threshold of the first higher-order mode

Let us consider only two competitive transverse modes – LP₀₁ and LP₁₁ with the corresponding oscillator equations shown as

$$\frac{dP_1^+(z)}{dz} = \left[\int_0^{2\pi} \int_0^a \left[\frac{g_0(z)}{1 + \sum_i \Gamma_i(r, \theta) A_{core}(P_i^+(z) + c_i / P_i^+(z)) / P_{sat}} \right] \Gamma_1(r, \theta) r dr d\theta \right] P_1^+(z) - \alpha_1 P_1^+(z). \quad (5.16)$$

$$\frac{dP_2^+(z)}{dz} = \left[\int_0^{2\pi} \int_0^a \left[\frac{g_0(z)}{1 + \sum_i \Gamma_i(r, \theta) A_{core}(P_i^+(z) + c_i / P_i^+(z)) / P_{sat}} \right] \Gamma_2(r, \theta) r dr d\theta \right] P_2^+(z) - \alpha_2 P_2^+(z). \quad (5.17)$$

where $P_1(z)$ and $P_2(z)$ represent the transverse powers of FM and 1st HOM. The power filling distributions (or normalized intensity profiles) are the same as Eq. (5.2). Usually for IAG fiber lasers with large core, the power in the cladding could be negligible. Therefore we have

$$\int_0^{2\pi} \int_0^a \Gamma_i(r, \theta) r dr d\theta = \frac{P_i^{core}}{P_i^{core} + P_i^{clad}} \approx 1. \quad (5.18)$$

The threshold of the FM could be obtained by setting $P_1^\pm(z) = P_2^\pm(z) = 0$ in Eq. (5.16), yielding

$$\bar{g}_1^{th} L = \int_0^L g_0(z) dz = \alpha_1 L - \frac{1}{2} \ln R_l R_r. \quad (5.19)$$

here the expression is similar to Eq. (3.44), except that the gain is not uniform along propagation for end pumping. The average gain \bar{g}_1^{th} (over fiber length) is used for end-pumped lasers, and compared with the uniform gain in side-pumped lasers. The threshold power of the FM could then be calculated from Eq. (5.19) and is shown in Eq. (4.35). The gain threshold for the 1st HOM could be simply calculated by setting $P_2^\pm(z) = 0$ in Eqs. (5.16) and (5.17), yielding

$$\int_0^L \int_0^{2\pi} \int_0^a \frac{g_0(z)}{1 + \Gamma_1(r, \theta) A_{core} (P_1^+(z) + P_1^-(z)) / P_{sat}} \Gamma_1(r, \theta) r dr d\theta dz = \alpha_1 L - \frac{1}{2} \ln R_l R_r. \quad (5.20)$$

$$\int_0^L \int_0^{2\pi} \int_0^a \frac{g_0(z)}{1 + \Gamma_1(r, \theta) A_{core} (P_1^+(z) + P_1^-(z)) / P_{sat}} \Gamma_2(r, \theta) r dr d\theta dz = \alpha_2 L - \frac{1}{2} \ln R_l R_r. \quad (5.21)$$

It is seen that Eqs. (5.16) and (5.17) are reduced to two decoupled equations (5.20) and (5.21) which require much less computation work. The average gain threshold for the 1st

HOM is then calculated by $\bar{g}_2^{th} L = \int_0^L g_0(z) dz$.

5.3.3 Regions of single-fundamental-mode operation

Figure 5-3 demonstrates the typical contour plot of average gain threshold ratio $\bar{g}_2^{th} / \bar{g}_1^{th}$ between LP₁₁ to LP₀₁ mode as a function of single-pass internal loss and output coupler in core-pumped IAG fiber lasers. The simulation parameters are shown in Table 5-3 with many parameters chosen from Ref. [107], for 1.05 μm Nd³⁺-doped IAG fiber lasers.

Table 5-3 Simulation parameters for Figure 5-3

Parameter	Value	Parameter	Value
λ_p	803 (nm)	σ_{ap}	0.7×10^{-20} (cm ⁻²)
λ_s	1053 (nm)	σ_{ep}	3.76×10^{-22} (cm ⁻²)
N	1×10^{-20} (cm ⁻³)	σ_{as}	7.82×10^{-22} (cm ⁻²)
R_l	1	σ_{es}	4.4×10^{-20} (cm ⁻²)
L	10 (cm)	α_p	$(\lambda_p / \lambda_s)^2 \alpha_1$
τ	0.19 (ms)	α_2	$2.54 \alpha_1$
a	100 (μ m)		

Similar to uniformly side-pumped IAG fiber lasers shown in Figure 5-1, the gain threshold ratio becomes large in the top-right region where the output coupling loss T is small or the single-pass internal loss ($\alpha_1 L$) is large.

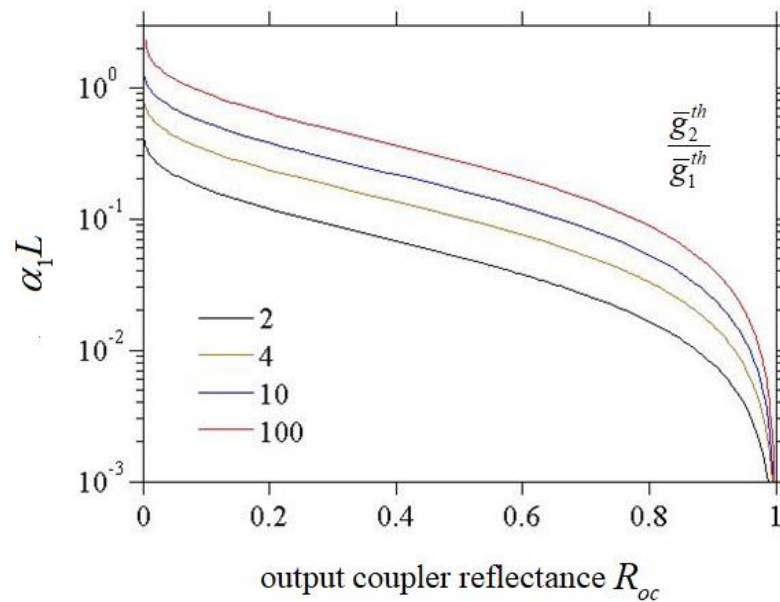


Figure 5-3 Contour plot of average gain threshold ratio $\bar{g}_2^{th} / \bar{g}_1^{th}$, as a function of single-pass loss $\alpha_1 L$ of the fundamental mode (logarithmic scale) and output coupler R_{oc} (linear scale) in core-pumped IAG fiber lasers.

5.3.4 Extraction efficiency of single fundamental mode

For core-pumped IAG lasers, in order to ensure single fundamental mode oscillation in IAG lasers, we need to choose the proper input power $P_p^+(0)$ such that the corresponding single-pass gain $\int_0^L g_0(z)dz$ is below the 1st HOM threshold $\bar{g}_2^{th}L$. The extraction efficiency of single fundamental mode is of interest for multimoded IAG lasers. In order to coincide with the expression of extraction efficiency in uniformly side-pumped lasers (Eq. (3.40)), the extraction efficiency of single fundamental mode in core-pumped IAG lasers could be written as

$$\eta_{SM} = \frac{(P_1^+(L) / P_{sat})(1 - R_{oc})}{g_0 L}. \quad (5.22)$$

where the saturated power P_{sat} is defined in Eq. (4.28).

Figure 5-4 demonstrates the maximal extraction efficiency of single fundamental mode η_{SM} in core-pumped IAG fiber lasers as a function of optimal output coupler R_{oc} , for various single-pass internal losses $\alpha_1 L$ and average unsaturated single-pass gains. The simulation parameters are the same as in Table 5-3. Similar to uniformly side-pumped IAG fiber lasers (Figure 5-2), the maximal extraction efficiency of single fundamental mode in core-pumped IAG fiber lasers is also suppressed due to transverse mode competition, for large value of \bar{g}_0 / α_1 . Moreover, the calculated absolute maximal extraction efficiency H_{SM}^{\max} is 0.499 which is the same as in uniformly side-pumped fiber lasers. This could be derived as follows.

Let $\alpha_2 = k\alpha_1$, as similar to Eq. (5.5) for uniformly side-pumped fiber lasers, the corresponding equation for core-pumped fiber lasers with non-uniform gain is expressed as

$$\int_0^L \int_0^{2\pi} \int_0^a \frac{g_0(z)(k\Gamma_1(r, \theta) - \Gamma_2(r, \theta))}{1 + \Gamma_1(r, \theta)A_{core}(P_1^+(z) + P_1^-(z))/P_{sat}} r dr d\theta dz = -\frac{(k-1)}{2} \ln R_{oc}. \quad (5.23)$$

At the limit of low loss $\alpha_1 L \rightarrow 0$ and weak coupling $R_{oc} \rightarrow 1$ where $P_1^+(z) = P_1^-(z) = P_1$ and $-\ln R_{oc} = 1 - R_{oc}$, Eq. (5.23) is changed to

$$\begin{aligned} \int_0^L \int_0^{2\pi} \int_0^a \frac{g_0(z)(k\Gamma_1(r, \theta) - \Gamma_2(r, \theta))}{1 + 2\Gamma_1(r, \theta)A_{core}P_1/P_{sat}} r dr d\theta dz = \\ \bar{g}_0 L \int_0^{2\pi} \int_0^a \frac{(k\Gamma_1(r, \theta) - \Gamma_2(r, \theta))}{1 + 2\Gamma_1(r, \theta)A_{core}P_1/P_{sat}} r dr d\theta = \frac{(k-1)}{2} (1 - R_{oc}). \end{aligned} \quad (5.24)$$

Since the right-hand side of Eq. (5.24) is close to zero, we have $2\Gamma_1(r, \theta)A_{core}P_1/P_{sat} \gg 1$ and Eq. (5.24) is further simplified to

$$\frac{\bar{g}_0 L}{2P_1/P_{sat}} \int_0^{2\pi} \int_0^a \frac{(k\Gamma_1(r, \theta) - \Gamma_2(r, \theta))}{A_{core}\Gamma_1(r, \theta)} r dr d\theta = \frac{(k-1)}{2} (1 - R_{oc}). \quad (5.25)$$

which then yields

$$H_{SM}^{\max} = \frac{P_1/P_{sat}(1 - R_{oc})}{\bar{g}_0 L} = \frac{k - 1.7714}{k - 1} = 0.4991. \quad (5.26)$$

Compare Eq. (5.25) to Eq. (5.7), it is seen that the absolute maximal extraction efficiency does not depend on the pump schemes, but relates to the ratio of modal profile and modal loss, which was stated previously in Section 3.4.5.

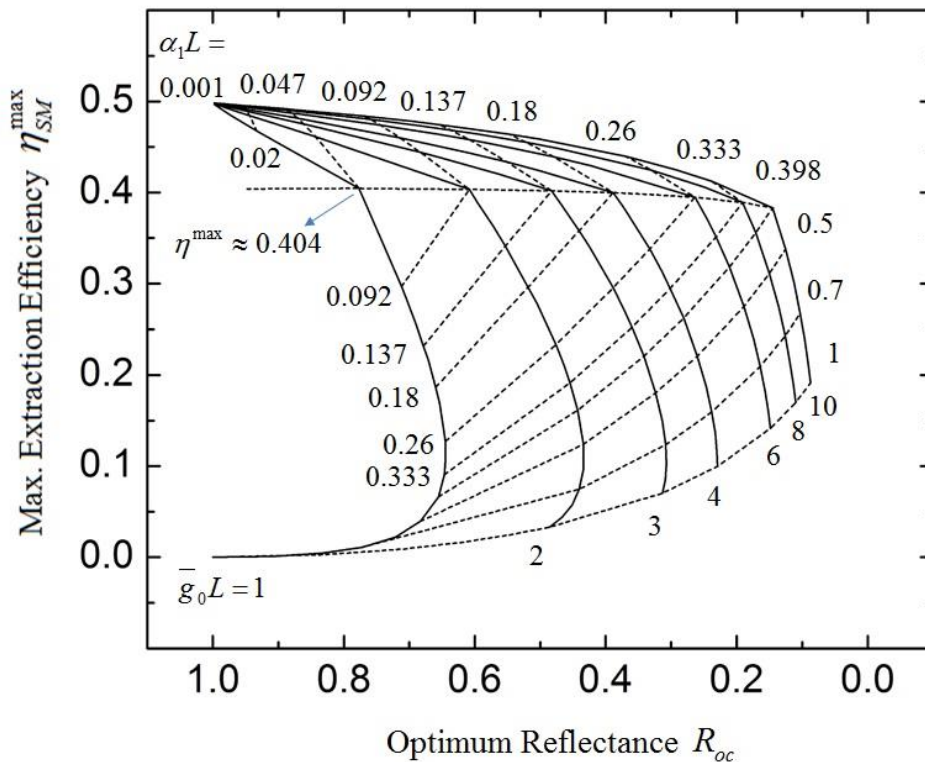


Figure 5-4 Maximal extraction efficiency of the single fundamental mode (η_{SM}^{\max}) in a multimoded core-pumped IAG fiber laser as a function of optimal output coupler R_{opt} , for various single-pass gains (solid lines) and distributed losses (dash lines).

In addition, it is seen from Figure 5-4 that the kink points in core-pumped IAG fiber lasers also satisfy the scaling law under weak coupling condition, which was discussed in Sections 3.4 and 5.1. Figure 5-4 shows the solution of the kink points in core-pumped IAG fiber lasers, from which it is seen that the scaling law is roughly satisfied with a nearly fixed g_0 / α_1 value of ~ 22 and $-\ln R_{opt} / \alpha_1 L$ value of ~ 5.4 . Moreover, it is seen that the kink occurs when the maximal extraction efficiency is over $\sim 40\%$.

Table 5-4 Kink points in core-pumped IAG fiber lasers

$\alpha_1 L$	$\bar{g}_0 L$	R_{opt}	η_{SM}^{max}	\bar{g}_0 / α_1	$-\ln(R_{opt})/\alpha_1 L$
0.047	1	0.777	0.405	21.455	5.417
0.092	2	0.609	0.404	21.656	5.379
0.137	3	0.483	0.402	21.923	5.326
0.180	4	0.388	0.400	22.256	5.262
0.260	6	0.264	0.395	23.074	5.123
0.333	8	0.191	0.390	24.056	4.982
0.398	10	0.145	0.383	25.128	4.851

5.4 Summary

For uniformly side-pumped IAG fiber lasers, single-mode operation is favored for large distributed loss of FM and small output coupling. With the consideration of transverse mode competition, the calculated extraction efficiency of single fundamental mode is suppressed when the small signal gain is large and distributed loss (of FM) is small, or roughly at $g_0/\alpha_1 > 21$. A quasi analytical method is proposed to calculate the threshold power of the 1st HOM, which seems to work well to predict the HOM threshold power in one published experimental work.

For core-pumped IAG fiber lasers with the consideration of transverse mode competition, the same quasi analytical method could be implemented to calculate the HOM threshold power. Based on the numerical model it is shown that single-mode operation also benefits from large distributed loss or small output coupling, which is similar to the scenario of uniform side pumping. Indeed, it could be assumed that the only difference between uniform side pumping and end pumping is the different gain evolution along the fiber, where in end pumping the unsaturated gain coefficient is non-uniform and the

corresponding single-pass gain is not proportional to the cavity length. A parameter of average single-pass gain could be used to feature the effective gain in end-pumped fiber lasers. The extraction efficiency of single fundamental mode is also calculated in core-pumped IAG fiber lasers, showing the similar trend of output suppression due to transverse mode competition.

In addition, it is seen that for both uniformly side-pumped and core-pumped IAG fiber lasers, the absolute maximal extraction efficiency of single fundamental mode is always $\sim 50\%$, or more generally, $(k-1.7714/k-1)$ with k the waveguide loss ratio between FM and 1st HOM (for IAG fibers, $k = 2.54$). In fact, this value is only dependent on the ratio of modal loss and modal profile between FM and 1st HOM.

CHAPTER 6 CONCLUSION

Index-antiguided structure is promising for large-mode-area high-power laser application due to its simple step-index structure. An intrinsic differential loss between FM and HOMs, with a loss ratio (between LP₀₁ and LP₁₁) of 2.54 in IAG fibers and 4 for IAG planar waveguides, makes IAG waveguides potential for large-mode-area operation. Up to 400 μm core size can be achieved in IAG fiber lasers. The current challenges of IAG fiber lasers are the low end pumping efficiency and the effect of HOM oscillation, which are solved by this dissertation.

In this dissertation, numerical analysis has shown that cladding pumping is not efficient for IAG fibers due to both index-antiguiding effect and large core size, and core pumping should be used in IAG fiber lasers. To achieve high output efficiency, the gain length $L_{gain} = 1/\sigma_{ap}N$ should be much smaller than the decay length $L_{decay} = -\ln R_{oc}/2\alpha_s$, and the fiber length should be chosen such that $L_{gain} \leq L \ll L_{decay}$. The reason for the low efficiency in the published Ref. [21] is due to the failure of satisfying the above conditions and use of cladding pumping.

The effect of transverse mode competition in IAG waveguide lasers is also comprehensively studied, showing that single-mode operation is favored when the waveguide loss of the FM is large and the output coupling loss is small (large R_{oc}). The extraction efficiency of single fundamental mode is calculated, demonstrating maximum value of $\sim 50\%$ (not including the factor of λ_p/λ_s) in both uniformly side-pumped and core-pumped IAG fiber lasers. This low efficiency is due to the small 2.54 modal loss ratio between FM and 1st HOM.

Future work on IAG fiber lasers can focus on the implementation of core pumping technique and optimization of laser parameters to yield high output efficiency and single-mode operation, based on the theoretical results from Chapter 4 and Chapter 5.

REFERENCES

- [1] D. J. Richardson, J. Nilsson, and W. A. Clarkson, "High power fiber lasers: current status and future perspectives [Invited]," *Journal of the Optical Society of America B*, vol. 27, pp. B63-B92, 2010.
- [2] E. Snitzer, H. Po, F. Hakimi, R. Tumminelli, and B. McCollum, "Double clad, offset core Nd fiber laser," in *Optical fiber sensors*, 1988, p. PD5.
- [3] Y.-C. Jeong, A. J. Boyland, J. K. Sahu, S.-H. Chung, J. Nilsson, and D. N. Payne, "Multi-kilowatt single-mode ytterbium-doped large-core fiber laser," *Journal of the Optical Society of Korea*, vol. 13, pp. 416-422, 2009.
- [4] V. Dominic, S. MacCormack, R. Waarts, S. Sanders, S. Bicknese, R. Dohle, *et al.*, "110 W fibre laser," *Electronics Letters*, vol. 35, pp. 1158-1160, 1999.
- [5] I. Photonics, "IPG photonics successfully tests world's first 10 kilowatt single-mode production laser," ed, 2009.
- [6] J. Limpert, T. Schreiber, S. Nolte, H. Zellmer, A. Tünnermann, R. Iliew, *et al.*, "High-power air-clad large-mode-area photonic crystal fiber laser," *Optics Express*, vol. 11, pp. 818-823, 2003.
- [7] S. Saitoh, K. Saitoh, M. Kashiwagi, S. Matsuo, and L. Dong, "Design optimization of large-mode-area all-solid photonic bandgap fibers for high-power laser applications," *Journal of Lightwave Technology*, vol. 32, pp. 440-449, 2013.
- [8] G. Gu, F. Kong, T. Hawkins, J. Parsons, M. Jones, C. Dunn, *et al.*, "Ytterbium-doped large-mode-area all-solid photonic bandgap fiber lasers," *Optics Express*, vol. 22, pp. 13962-13968, 2014.
- [9] L. Dong, X. Peng, and J. Li, "Leakage channel optical fibers with large effective area," *Journal of the Optical Society of America B*, vol. 24, pp. 1689-1697, 2007.
- [10] F. Kong, G. Gu, T. W. Hawkins, J. Parsons, M. Jones, C. Dunn, *et al.*, "Flat-top mode from a 50 μm -core Yb-doped leakage channel fiber," *Optics Express*, vol. 21, pp. 32371-32376, 2013.
- [11] C.-H. Liu, G. Chang, N. Litchinitser, D. Guertin, N. Jacobsen, K. Tankala, *et al.*, "Chirally coupled core fibers at 1550-nm and 1064-nm for effectively single-mode core size scaling," in *Lasers and Electro-Optics, CLEO 2007*, pp. 1-2, 2007.
- [12] X. Ma, C. Zhu, I.-N. Hu, A. Kaplan, and A. Galvanauskas, "Single-mode chirally-coupled-core fibers with larger than 50 μm diameter cores," *Optics Express*, vol. 22, pp. 9206-9219, 2014.
- [13] Y. Chen, T. McComb, V. Sudesh, M. Richardson, and M. Bass, "Very large-core, single-mode, gain-guided, index-antiguide fiber lasers," *Optics Letters*, vol. 32, pp. 2505-2507, 2007.
- [14] A. E. Siegman, "Gain-guided, index-antiguide fiber lasers," *Journal of the Optical Society of America B*, vol. 24, pp. 1677-1682, 2007.
- [15] M.-A. Miri, P. LiKamWa, and D. N. Christodoulides, "Large area single-mode parity-time-symmetric laser amplifiers," *Optics Letters*, vol. 37, pp. 764-766, 2012.
- [16] J. R. Marciante, R. G. Roides, V. V. Shkunov, and D. A. Rockwell, "Near-diffraction-limited operation of step-index large-mode-area fiber lasers via gain filtering," *Optics Letters*, vol. 35, pp. 1828-1830, 2010.

- [17] C. Wang, Y. Liu, L. W. Casperson, and T.-H. Her, "Power characteristics of planar index-antiguided waveguide lasers with transverse mode competition," *AIP Advances*, vol. 6, p. 125206, 2016.
- [18] A. Siegman, "Propagating modes in gain-guided optical fibers," *Journal of the Optical Society of America A*, vol. 20, pp. 1617-1628, 2003.
- [19] A. E. Siegman, Y. Chen, V. Sudesh, M. C. Richardson, M. Bass, P. Foy, *et al.*, "Confined propagation and near single-mode laser oscillation in a gain-guided, index antiguided optical fiber," *Applied Physics Letters*, vol. 89, p. 251101, 2006.
- [20] Y. Liu, L. W. Casperson, and T. H. Her, "Transverse mode competition in index-antiguided waveguide lasers," *Applied Physics Letters*, vol. 107, p. 241111, 2015.
- [21] V. Sudesh, T. McComb, Y. Chen, M. Bass, M. Richardson, J. Ballato, *et al.*, "Diode-pumped 200 μ m diameter core, gain-guided, index-antiguided single mode fiber laser," *Applied Physics B*, vol. 90, pp. 369-372, 2008.
- [22] X. Wang, Y. Chen, W. Hageman, G. U. Kim, M. Richardson, C. Xiong, *et al.*, "Transverse mode competition in gain-guided index antiguided fiber lasers," *Journal of the Optical Society of America B*, vol. 29, pp. 191-196, 2012.
- [23] Y. Liu, T.-H. Her, and L. Casperson, "High-efficiency continuous-wave index-antiguided planar waveguide laser with large mode area," in *CLEO: 2014*, p. SM2F.5, 2014.
- [24] C. Wang, T. H. Her, L. Zhao, X. Ao, L. W. Casperson, C. H. Lai, *et al.*, "Gain Saturation and Output Characteristics of Index-Antiguided Planar Waveguide Amplifiers With Homogeneous Broadening," *Journal of Lightwave Technology*, vol. 29, pp. 1958-1964, 2011.
- [25] C. Wang, T. H. Her, and L. W. Casperson, "Power characteristics of homogeneously broadened index-antiguided waveguide lasers," *Optics Letters*, vol. 37, pp. 815-817, 2012.
- [26] L. W. Casperson, "Laser power calculations - sources of error," *Applied Optics*, vol. 19, pp. 422-434, 1980.
- [27] L. Quintino, A. Costa, R. Miranda, D. Yapp, V. Kumar, and C. Kong, "Welding with high power fiber lasers—a preliminary study," *Materials & Design*, vol. 28, pp. 1231-1237, 2007.
- [28] M. S. F. d. Lima, F. A. Goia, R. Riva, and A. M. d. Espírito Santo, "Laser surface remelting and hardening of an automotive shaft using a high-power fiber laser," *Materials Research*, vol. 10, pp. 461-467, 2007.
- [29] H. Booth, "Laser Processing in Industrial Solar Module Manufacturing," *Journal of Laser Micro/Nanoengineering*, vol. 5, 2010.
- [30] E. Schneiderlochner, A. Grohe, S. Glunz, R. Preu, and W. Willeke, "Scanning Nd:YAG laser system for industrially applicable processing in silicon solar cell manufacturing," in *Photovoltaic Energy Conversion, 2003. Proceedings of 3rd World Conference*, pp. 1364-1367, 2003.
- [31] N. M. Fried and K. E. Murray, "High-power thulium fiber laser ablation of urinary tissues at 1.94 μ m," *Journal of Endourology*, vol. 19, pp. 25-31, 2005.
- [32] M. J. Bader, R. Sroka, C. Gratzke, M. Seitz, P. Weidlich, M. Staehler, *et al.*, "Laser therapy for upper urinary tract transitional cell carcinoma: indications and management," *European Urology*, vol. 56, pp. 65-71, 2009.

- [33] G. M. Hale and M. R. Querry, "Optical constants of water in the 200-nm to 200- μm wavelength region," *Applied Optics*, vol. 12, pp. 555-563, 1973.
- [34] T. Bilici, S. Mutlu, H. Kalaycioglu, A. Kurt, A. Sennaroglu, and M. Gulsoy, "Development of a thulium (Tm: YAP) laser system for brain tissue ablation," *Lasers in Medical Science*, vol. 26, p. 699, 2011.
- [35] H. Ludwig, T. Kruschat, T. Knobloch, H.-O. Teichmann, K. Rostasy, and V. Rohde, "First experiences with a 2.0- μm near infrared laser system for neuroendoscopy," *Neurosurgical Review*, vol. 30, pp. 195-201, 2007.
- [36] M. H. Bui, A. Breda, D. Gui, J. Said, and P. Schulam, "Less smoke and minimal tissue carbonization using a thulium laser for laparoscopic partial nephrectomy without hilar clamping in a porcine model," *Journal of Endourology*, vol. 21, pp. 1107-1112, 2007.
- [37] B. Chen, S. L. Thomsen, R. J. Thomas, J. Oliver, and A. J. Welch, "Histological and modeling study of skin thermal injury to 2.0 μm laser irradiation," *Lasers in Surgery and Medicine*, vol. 40, pp. 358-370, 2008.
- [38] R. Kaufmann, A. Hartmann, and R. Hibst, "Cutting and skin - ablative properties of pulsed mid - infrared laser surgery," *The Journal of Dermatologic Surgery and Oncology*, vol. 20, pp. 112-118, 1994.
- [39] S.-J. Xia, J. Zhuo, X.-W. Sun, B.-M. Han, Y. Shao, and Y.-N. Zhang, "Thulium laser versus standard transurethral resection of the prostate: a randomized prospective trial," *European Urology*, vol. 53, pp. 382-390, 2008.
- [40] M. H. Niemz, *Laser-tissue interactions: fundamentals and applications*: Springer Science & Business Media, 2013.
- [41] V. Coffey, "High-energy lasers: new advances in defense applications," *Optics and Photonics News*, vol. 25, pp. 28-35, 2014.
- [42] S. D. Jackson, "Towards high-power mid-infrared emission from a fibre laser," *Nature Photonics*, vol. 6, pp. 423-431, 2012.
- [43] <http://investor.ipgphotonics.com/~media/Files/I/Ipg-Photonics-IR/Annual%20Reports/2016-ar-final.pdf>.
- [44] A. V. Smith, B. T. Do, G. R. Hadley, and R. L. Farrow, "Optical damage limits to pulse energy from fibers," *IEEE Journal of Selected Topics in Quantum Electronics*, vol. 15, pp. 153-158, 2009.
- [45] J. Limpert, F. Roser, S. Klingebiel, T. Schreiber, C. Wirth, T. Peschel, *et al.*, "The rising power of fiber lasers and amplifiers," *IEEE Journal of Selected Topics in Quantum Electronics*, vol. 13, pp. 537-545, 2007.
- [46] G. P. Agrawal, *Nonlinear Fiber Optics*: Academic press, 2007.
- [47] P. Li, C. Zhu, S. Zou, H. Zhao, D. Jiang, G. Li, *et al.*, "Theoretical and experimental investigation of thermal effects in a high power Yb 3+-doped double-clad fiber laser," *Optics & Laser Technology*, vol. 40, pp. 360-364, 2008.
- [48] L. Zenteno, "High-power double-clad fiber lasers," *Journal of Lightwave Technology*, vol. 11, pp. 1435-1446, 1993.
- [49] J. W. Dawson, M. J. Messerly, R. J. Beach, M. Y. Shverdin, E. A. Stappaerts, A. K. Sridharan, *et al.*, "Analysis of the scalability of diffraction-limited fiber lasers and amplifiers to high average power," *Optics Express*, vol. 16, pp. 13240-13266, 2008.
- [50] D. E. Gray, *American institute of physics handbook*: McGraw-Hill, 1982.

- [51] W. F. Krupke, M. D. Shinn, J. E. Marion, J. A. Caird, and S. E. Stokowski, "Spectroscopic, optical, and thermomechanical properties of neodymium- and chromium-doped gadolinium scandium gallium garnet," *Journal of the Optical Society of America B*, vol. 3, pp. 102-114, 1986.
- [52] Y. Fan, B. He, J. Zhou, J. Zheng, H. Liu, Y. Wei, *et al.*, "Thermal effects in kilowatt all-fiber MOPA," *Optics Express*, vol. 19, pp. 15162-15172, 2011.
- [53] M. Eilchi and P. Parvin, "Heat Generation and Removal in Fiber Lasers," in *Fiber Laser*, ed: InTech, 2016.
- [54] R. House, J. Bettis, and A. Guenther, "Surface roughness and laser damage threshold," *IEEE Journal of Quantum Electronics*, vol. 13, pp. 361-363, 1977.
- [55] D. C. Brown and H. J. Hoffman, "Thermal, stress, and thermo-optic effects in high average power double-clad silica fiber lasers," *IEEE Journal of Quantum Electronics*, vol. 37, pp. 207-217, 2001.
- [56] J. P. Koplrow, D. A. Kliner, and L. Goldberg, "Single-mode operation of a coiled multimode fiber amplifier," *Optics Letters*, vol. 25, pp. 442-444, 2000.
- [57] R. T. Schermer, "Mode scalability in bent optical fibers," *Optics Express*, vol. 15, pp. 15674-15701, 2007.
- [58] F. Jansen, F. Stutzki, H.-J. Otto, T. Eidam, A. Liem, C. Jauregui, *et al.*, "Thermally induced waveguide changes in active fibers," *Optics Express*, vol. 20, pp. 3997-4008, 2012.
- [59] J. Knight, T. Birks, P. S. J. Russell, and D. Atkin, "All-silica single-mode optical fiber with photonic crystal cladding," *Optics Letters*, vol. 21, pp. 1547-1549, 1996.
- [60] T. A. Birks, J. C. Knight, and P. S. J. Russell, "Endlessly single-mode photonic crystal fiber," *Optics Letters*, vol. 22, pp. 961-963, 1997.
- [61] J. Limpert, N. D. Robin, I. Manek-Honninger, F. Salin, F. Roser, A. Liem, *et al.*, "High-power rod-type photonic crystal fiber laser," *Optics Express*, vol. 13, pp. 1055-1058, 2005.
- [62] F. Stutzki, F. Jansen, H.-J. Otto, C. Jauregui, J. Limpert, and A. Tünnermann, "Designing advanced very-large-mode-area fibers for power scaling of fiber-laser systems," *Optica*, vol. 1, pp. 233-242, 2014.
- [63] G. Gu, F. Kong, T. W. Hawkins, P. Foy, K. Wei, B. Samson, *et al.*, "Impact of fiber outer boundaries on leaky mode losses in leakage channel fibers," *Optics Express*, vol. 21, pp. 24039-24048, 2013.
- [64] F. Jansen, F. Stutzki, C. Jauregui, J. Limpert, and A. Tünnermann, "Avoided crossings in photonic crystal fibers," *Optics Express*, vol. 19, pp. 13578-13589, 2011.
- [65] M. Laurila, M. M. Jørgensen, K. R. Hansen, T. T. Alkeskjold, J. Broeng, and J. Lægsgaard, "Distributed mode filtering rod fiber amplifier delivering 292W with improved mode stability," *Optics Express*, vol. 20, pp. 5742-5753, 2012.
- [66] M. M. Jørgensen, S. R. Petersen, M. Laurila, J. Lægsgaard, and T. T. Alkeskjold, "Optimizing single mode robustness of the distributed modal filtering rod fiber amplifier," *Optics Express*, vol. 20, pp. 7263-7273, 2012.
- [67] D. Jain, C. Baskiotis, and J. K. Sahu, "Mode area scaling with multi-trench rod-type fibers," *Optics Express*, vol. 21, pp. 1448-1455, 2013.

- [68] D. Jain, C. Baskiotis, T. C. May-Smith, J. Kim, and J. K. Sahu, "Large mode area multi-trench fiber with delocalization of higher order modes," *IEEE Journal of Selected Topics in Quantum Electronics*, vol. 20, pp. 242-250, 2014.
- [69] G. Gu, F. Kong, T. W. Hawkins, M. Jones, and L. Dong, "Extending mode areas of single-mode all-solid photonic bandgap fibers," *Optics Express*, vol. 23, pp. 9147-9156, 2015.
- [70] F. Kong, G. Gu, T. W. Hawkins, M. Jones, J. Parsons, M. T. Kalichevsky-Dong, *et al.*, "~ 1 kilowatt Ytterbium-doped all-solid photonic bandgap fiber laser," in *SPIE LASE*, pp. 1008311-1008311-5, 2017.
- [71] W. S. Wong, X. Peng, J. M. McLaughlin, and L. Dong, "Breaking the limit of maximum effective area for robust single-mode propagation in optical fibers," *Optics Letters*, vol. 30, pp. 2855-2857, 2005.
- [72] L. Dong, H. A. McKay, L. Fu, M. Ohta, A. Marcinkevicius, S. Suzuki, *et al.*, "Ytterbium-doped all glass leakage channel fibers with highly fluorine-doped silica pump cladding," *Optics Express*, vol. 17, pp. 8962-8969, 2009.
- [73] L. Dong, T.-w. Wu, H. A. McKay, L. Fu, J. Li, and H. G. Winful, "All-glass large-core leakage channel fibers," *IEEE Journal of Selected Topics in Quantum Electronics*, vol. 15, pp. 47-53, 2009.
- [74] L. Dong, H. A. McKay, A. Marcinkevicius, L. Fu, J. Li, B. K. Thomas, *et al.*, "Extending effective area of fundamental mode in optical fibers," *Journal of Lightwave Technology*, vol. 27, pp. 1565-1570, 2009.
- [75] C.-H. Liu, G. Chang, N. Litchinitser, A. Galvanauskas, D. Guertin, N. Jacobson, *et al.*, "Effectively single-mode chirally-coupled core fiber," in *Advanced Solid-State Photonics*, p. ME2, 2007.
- [76] X. Ma, C.-H. Liu, G. Chang, and A. Galvanauskas, "Angular-momentum coupled optical waves in chirally-coupled-core fibers," *Optics Express*, vol. 19, pp. 26515-26528, 2011.
- [77] J. Limpert, F. Stutzki, F. Jansen, H.-J. Otto, T. Eidam, C. Jauregui, *et al.*, "Yb-doped large-pitch fibres: effective single-mode operation based on higher-order mode delocalisation," *Light: Science & Applications*, vol. 1, p. e8, 2012.
- [78] C. Xu and W. Huang, "Finite-difference beam propagation method for guide-wave optics," *Progress in Electromagnetics Research, PIER*, vol. 11, pp. 1-49, 1995.
- [79] Y. Tsuji and M. Koshiba, "Finite element beam propagation method with perfectly matched layer boundary conditions for three - dimensional optical waveguides," *International Journal of Numerical Modelling: Electronic Networks, Devices and Fields*, vol. 13, pp. 115-126, 2000.
- [80] S. Konno, S. Fujikawa, and K. Yasui, "206 W continuous-wave TEM[sub 00] mode 1064 nm beam generation by a laser-diode-pumped Nd:YAG rod laser amplifier," *Applied Physics Letters*, vol. 79, pp. 2696-2697, 2001.
- [81] T. H. Allik, W. W. Hovis, D. P. Caffey, and V. King, "Efficient diode-array-pumped Nd:YAG and Nd:Lu:YAG lasers," *Optics Letters*, vol. 14, pp. 116-118, 1989.
- [82] W. W. Rigrod, "Gain saturation and output power of optical masers," *Journal of Applied Physics*, vol. 34, pp. 2602-2609, 1963.

- [83] T.-H. Her, X. Ao, and L. W. Casperson, "Gain saturation in gain-guided slab waveguides with large-index antiguiding," *Optics Letters*, vol. 34, pp. 2411-2413, 2009.
- [84] W. Rigrod, "Homogeneously broadened CW lasers with uniform distributed loss," *IEEE Journal of Quantum Electronics*, vol. 14, pp. 377-381, 1978.
- [85] G. Schindler, "Optimum output efficiency of homogeneously broadened lasers with constant loss," *IEEE Journal of Quantum Electronics*, vol. 16, pp. 546-549, 1980.
- [86] D. P. Shepherd, S. J. Hettrick, C. Li, J. I. Mackenzie, R. J. Beach, S. C. Mitchell, *et al.*, "High-power planar dielectric waveguide lasers," *Journal of Physics D*, vol. 34, pp. 2420-2432, 2001.
- [87] J. Limpert, T. Schreiber, S. Nolte, H. Zellmer, T. Tunnermann, R. Iliew, *et al.*, "High-power air-clad large-mode-area photonic crystal fiber laser," *Optics Express*, vol. 11, pp. 818-23, 2003.
- [88] L. Dong, J. Li, and X. Peng, "Bend-resistant fundamental mode operation in ytterbium-doped leakage channel fibers with effective areas up to 3160 μm^2 ," *Optics Express*, vol. 14, pp. 11512-11519, 2006.
- [89] L. Zhu, P. Chak, J. K. S. Poon, G. A. DeRose, A. Yariv, and A. Scherer, "Electrically-pumped, broad-area, single-mode photonic crystal lasers," *Optics Express*, vol. 15, pp. 5966-5975, 2007.
- [90] Y. Liu, T. H. Her, A. Dittli, and L. W. Casperson, "Continuous-wave hybrid index-antiguided and thermal-guided planar waveguide laser," *Applied Physics Letters*, vol. 103, p. 191103, 2013.
- [91] K. Kubodera and K. Otsuka, "SINGLE-TRANSVERSE-MODE LINDP4O12 SLAB WAVEGUIDE LASER," *Journal of Applied Physics*, vol. 50, pp. 653-659, 1979.
- [92] M. J. F. Digonnet and C. J. Gaeta, "Theoretical analysis of optical fiber laser amplifiers and oscillators," *Applied Optics*, vol. 24, pp. 333-342, 1985.
- [93] M. Gong, Y. Yuan, C. Li, P. Yan, H. Zhang, and S. Liao, "Numerical modeling of transverse mode competition in strongly pumped multimode fiber lasers and amplifiers," *Optics Express*, vol. 15, pp. 3236-3246, 2007.
- [94] D. Scarano and I. Montrosset, "Transversal mode competition in erbium-doped Ti:LiNbO₃ waveguide lasers," *IEEE Journal of Quantum Electronics*, vol. 32, pp. 628-637, 1996.
- [95] A. E. Siegman, *Lasers*. CA: University Science, 1986.
- [96] W. Hageman, Y. Chen, X. Wang, L. Gao, G. U. Kim, M. Richardson, *et al.*, "Scalable side-pumped, gain-guided index-antiguided fiber laser," *Journal of the Optical Society of America B*, vol. 27, pp. 2451-2459, 2010.
- [97] D. T. Nguyen, A. Chavez-Pirson, S. Jiang, and N. Peyghambarian, "A novel approach of modeling cladding-pumped highly Er-Yb co-doped fiber amplifiers," *IEEE Journal of Quantum Electronics*, vol. 43, pp. 1018-1027, 2007.
- [98] P. Konieczny, J. Świdorski, A. Zając, and M. Skorczakowski, "Analysis of activation of active double-clad optical fibers," *Optica Applicata*, vol. 35, 2005.
- [99] X. Ao, T. H. Her, and L. W. Casperson, "Gain guiding in large-core Bragg fibers," *Optics Express*, vol. 17, pp. 22666-22672, 2009.

- [100] N.-K. Chen and L.-J. Jian, "Core-pumped gain-guided index-antiguided continuous wave lasing in dispersion-engineered erbium-doped fiber," *Optics Letters*, vol. 37, pp. 3057-3059, 2012.
- [101] V. Sudesh, T. McComb, M. Richardson, W. Hagemann, M. Bass, J. Ballato, *et al.*, "Waveguide-pumping gain guided index antiguided fiber laser," ed: Google Patents, 2010.
- [102] I. Kelson and A. A. Hardy, "Strongly pumped fiber lasers," *IEEE Journal of Quantum Electronics*, vol. 34, pp. 1570-1577, 1998.
- [103] L. Dong, X. Peng, and J. Li, "Leakage channel optical fibers with large effective area," *Journal of the Optical Society of America B*, vol. 24, pp. 1689-1697, 2007.
- [104] S. H. Huang, C. Zhu, C. H. Liu, X. Q. Ma, C. Swan, A. Galvanauskas, *et al.*, "Power scaling of CCC fiber based lasers", 2009.
- [105] P. G. Yarandi, S. Karbasi, and A. Mafi, "Improving the power efficiency in end-pumped gain-guided index-antiguided fiber amplifiers," *Journal of Lightwave Technology*, vol. 30, pp. 3203-3210, 2012.
- [106] http://www.kigre.com/products/laser_glass.pdf.
- [107] X. Shen, W. Wei, H. Zou, and L. Zhang, "Analysis of dual-end-pumped Nd³⁺-doped index-crossover gain guided-index antiguided fiber laser," *Optics Communications*, vol. 366, pp. 205-209, 2016.

APPENDIX SIMULATION CODE

Below shows part of the modeling code in the dissertation. If readers are interested in more comprehensive code, please contact the author.

Table 1 Matlab code for Figure 4-9 (η_{max} vs. R_{opt} for uniformly side-pumped IAG fiber lasers without transverse mode competition)

```

clear all
clc
g=[1;2;3;4;6;8;10];
alpha1=5e-4;
alpha2=2.54*alpha1;
Rl=1;Rl1=1;Rl2=1;Rr1=1;Rr2=1;

Ropt=zeros(length(g),1);
I11_out_opt=zeros(length(g),1);

c1=1;
dc=0.0001;
zspan=0:0.01:1;
Rr0=0.06;dR=1e-4;
parfor m=1:length(g)

[Ropt(m),I11_out_opt(m)]=Optimal_R_1M(g(m),Rl,Rl1,Rl2,Rr1,Rr2,alpha1);
end
eita=I11_out_opt./g;
figure
plot(Ropt,eita)

function [Ropt,I11_out_opt]=Optimal_R_1M(g0,Rl,Rl1,Rl2,Rr1,Rr2,alpha1)
dR=1e-4;
Rth0=exp(2*(alpha1-g0))/Rl/Rl1/Rl2/Rr1/Rr2;
c1=1;
dc=0.0001;
zspan=0:0.01:1;
%R0=Rth0+1e3;
R0=0.99;
I11_outR=Iout_1D1M_fiber(g0,c1,dc,Rl,Rl1,R0+dR/2,Rr1,alpha1,zspan);
I11_outL=Iout_1D1M_fiber(g0,c1,dc,Rl,Rl1,R0-dR/2,Rr1,alpha1,zspan);
dif=(I11_outR-I11_outL)/dR;

count=0;count_max=20;
while abs(dif)>1e-8&&count<count_max
    R1=R0+dR;

I11_outR=Iout_1D1M_fiber(g0,c1,dc,Rl,Rl1,R1+dR/2,Rr1,alpha1,zspan);
    I11_outL=Iout_1D1M_fiber(g0,c1,dc,Rl,Rl1,R1-
dR/2,Rr1,alpha1,zspan);
    dif1=(I11_outR-I11_outL)/dR;

```

```

R0=abs(R0+dif/(dif-dif1)*dR);

I1l_outR=Iout_1D1M_fiber(g0,c1,dc,Rl,Rl1,R0+dR/2,Rr1,alpha1,zspan);
I1l_outL=Iout_1D1M_fiber(g0,c1,dc,Rl,Rl1,R0-
dR/2,Rr1,alpha1,zspan);
dif=(I1l_outR-I1l_outL)/dR;
count=count+1;
end
Ropt=R0;
I1l_out_opt=Iout_1D1M_fiber(g0,c1,dc,Rl,Rl1,R0,Rr1,alpha1,zspan);
end

function Iout=Iout_1D1M_fiber(g0,c1,dc,Rl,Rl1,Rr,Rr1,alpha1,zspan)
count=0;count_max=60;
r=linspace(0,1,200);
I10=sqrt(c1*Rl*Rl1);
I1l=sqrt(c1/Rr/Rr1);
[z,I] = ode45(@(z,I) IAG_fiber_onemode(z,I,g0,alpha1,c1,r),zspan,I10);
dif1=I(end,1)-I1l;

while abs(dif1)>1e-8&&count<count_max
dc=c1/100;
c2=c1+dc;
I10=sqrt(c2*Rl*Rl1);
I1l=sqrt(c2/Rr/Rr1);
[z,I] = ode45(@(z,I)
IAG_fiber_onemode(z,I,g0,alpha1,c2,r),zspan,I10);
dif2=I(end,1)-I1l;
c1=abs(c1+dif1/(dif1-dif2)*dc);
count=count+1;

I10=sqrt(c1*Rl*Rl1);
I1l=sqrt(c1/Rr/Rr1);
[z,I] = ode45(@(z,I)
IAG_fiber_onemode(z,I,g0,alpha1,c1,r),zspan,I10);
dif1=I(end,1)-I1l;
end
Iout=sqrt(c1/Rr/Rr1)*(1-Rr);
end

function dIdt = IAG_fiber_onemode(z,I,g0,alpha1,c1,r)
dIdt=0;
j01=2.4048;
const1=0.269515643830234;
f1=besselj(0,j01*r).^2/const1;
int1 = 2*f1.*r./(1+f1.*(I+c1./I));
integrall=trapz(r,int1);
dIdt = g0*I*integrall-alpha1*I;
end

```

Table 2 Matlab code for calculation of the 1st HOM threshold gain in uniformly side-pumped IAG fiber lasers

```

clear all
clc
alpha1=0.2;
alpha2=2.54*alpha1;
Rl1=1;Rr1=1;
Rl2=1;Rr2=1;
Rl=1;Rr=0.5;

gth=alpha1-1/2*log(Rl*Rl1*Rr*Rr1);
g0=gth+0.1; %initial guess
g0=2.1098;
dg=0.0001;
c1=1; % initial guess
dc=0.0001;
zspan=0:0.01:1;
r=linspace(0,1,200);
count_max=40;
count=0;
f0=HOMthreshold_calc_fiber(g0,c1,dc,Rl,Rl1,Rl2,Rr,Rr1,Rr2,alpha1,alpha
2,zspan,r);

while abs(f0)>1e-7&&count<count_max
g1=g0+dg;
f1=HOMthreshold_calc_fiber(g1,c1,dc,Rl,Rl1,Rl2,Rr,Rr1,Rr2,alpha1,alpha
2,zspan,r);
g0=abs(g0+f0/(f0-f1)*dg);
f0=HOMthreshold_calc_fiber(g0,c1,dc,Rl,Rl1,Rl2,Rr,Rr1,Rr2,alpha1,alpha
2,zspan,r);
count=count+1;
end
% calculated 1st HOM threshold
g0

function
f=HOMthreshold_calc_fiber(g0,c1,dc,Rl,Rl1,Rl2,Rr,Rr1,Rr2,alpha1,alpha2
,zspan,r)
count=0;count_max=60;
j01=2.4048;j11=3.8317;
%const1=2*trapz(r,besselj(0,j01*r).^2.*r);
%const2=2*trapz(r,besselj(1,j11*r).^2.*r);
const1=0.269515643830234;
const2=0.162215636332671;
f1=abs(besselj(0,j01*r).^2)/const1;
f2=abs(besselj(1,j11*r).^2)/const2;

I10=sqrt(c1*Rl*Rl1);
I11=sqrt(c1/Rr/Rr1);
[z,I] = ode45(@(z,I) IAG_fiber_onemode(z,I,g0,alpha1,c1,r),zspan,I10);
dif1=I(end,1)-I11;

while abs(dif1)>1e-6&&count<count_max

```

```

dc=c1/100;
c2=c1+dc;
I10=sqrt(c2*Rl*Rl1);
I11=sqrt(c2/Rr/Rr1);
[z, I] = ode45(@ (z, I)
IAG_fiber_onemode(z, I, g0, alpha1, c2, r), zspan, I10);
dif2=I(end, 1)-I11;
c1=abs(c1+dif1/(dif1-dif2)*dc);
count=count+1;

I10=sqrt(c1*Rl*Rl1);
I11=sqrt(c1/Rr/Rr1);
[z, I] = ode45(@ (z, I)
IAG_fiber_onemode(z, I, g0, alpha1, c1, r), zspan, I10);
dif1=I(end, 1)-I11;
end
Iz=I+c1./I;
int_z=zeros(length(Iz), 1);
for ii=1:length(Iz)
    F=2*f2.*r./(1+f1.*Iz(ii));
    int_z(ii)=trapz(r, F);
end
LHS=g0*trapz(zspan, int_z);
RHS=alpha2-0.5*log(Rl*Rr*Rl2*Rr2);
f=LHS-RHS;
end

```

Table 3 Matlab code for Figure 5-1 (contour plot of gain threshold ratio g_2^{th} / g_1^{th} , as a function of $\alpha_1 L$ and R_{oc} , in uniformly side-pumped IAG fiber lasers)

```

clear all
clc

Rl=1;Rl1=1;Rl2=1;Rr1=1;Rr2=1;
gr=100; % set gain threshold ratio
%alpha1=[linspace(0.001,0.04,100)
linspace(0.045,0.233,100)];%linspace(0.001,0.0755,50)
alpha1=[linspace(0.001,0.04,64) linspace(0.045,0.2,8)
linspace(0.21,3,96)];
alpha2=2.54*alpha1;

Rth=zeros(length(alpha1), 1);
parfor m=1:length(alpha1)
Rth(m)=Rth_gratio_fiber(gr,Rl,Rl1,Rl2,Rr1,Rr2,alpha1(m),alpha2(m));
end

figure
semilogy(Rth,alpha1)
xlim([0 1])
ylim([1e-3 3])

```

```

function R=Rth_gratio_fiber(gr,Rl,Rl1,Rl2,Rr1,Rr2,alpha1,alpha2)
R0=0.0001;%R0=0.00001;% initial guess of Rr
gth_FM=alpha1-1/2*log(Rl*Rl1*R0*Rr1);%FM gain threshold
g0=gth_FM*gr;
%Rth_0=exp(-2*(g0-alpha1))/Rl/Rl1/Rr1/Rl2/Rr2;
%R0=Rth_0+0.0001;%0.999;%Rth_0; %initial guess

dR=0.00001;%dR=0.000001;
c1=1; % initial guess
dc=0.0001;
zspan=0:0.01:1;
r=linspace(0,1,200);
count_max=20;
count=0;
f0=HOMthreshold_calc_fiber(g0,c1,dc,Rl,Rl1,Rl2,R0,Rr1,Rr2,alpha1,alpha
2,zspan,r);

while abs(f0)>1e-10&&count<count_max
R1=R0+dR;
gth_FM=alpha1-1/2*log(Rl*Rl1*R1*Rr1);%FM gain threshold
g0=gth_FM*gr;
f1=HOMthreshold_calc_fiber(g0,c1,dc,Rl,Rl1,Rl2,R1,Rr1,Rr2,alpha1,alpha
2,zspan,r);
R0=abs(R0+f0/(f0-f1)*dR);
gth_FM=alpha1-1/2*log(Rl*Rl1*R0*Rr1);
g0=gth_FM*gr;
f0=HOMthreshold_calc_fiber(g0,c1,dc,Rl,Rl1,Rl2,R0,Rr1,Rr2,alpha1,alpha
2,zspan,r);
count=count+1;
end
R=R0;
end

```

Table 4 Matlab code for Figure 5-2 (η_{SM}^{\max} vs. R_{opt} in uniformly side-pumped IAG fiber lasers)

```

% Calculate the range of output coupler [Rth1L, Rth1R] for single-mode
operation, for given single-pass gain and distributive loss.

clear all
clc

Rl=1;Rl1=1;Rl2=1;Rr1=1;Rr2=1;
g=[2 3 4 6 8 10];
alpha1=0.1399;%8.215e-4*1.98;
alpha2=2.54*alpha1;

%g0=alpha1-0.5*log(Rl*Rr);

```

```

Rth1L=zeros (length(g) , 1);
Rth1R=zeros (length(g) , 1);
for m=1:length(g)
Rth1L(m)=Rth_1L(g(m) , Rl, Rl1, Rl2, Rr1, Rr2, alpha1, alpha2);
Rth1R(m)=Rth_1R(g(m) , Rl, Rl1, Rl2, Rr1, Rr2, alpha1, alpha2);
end

figure
plot(g, Rth1L, g, Rth1R, 'r')

function R=Rth_1L(g0, Rl, Rl1, Rl2, Rr1, Rr2, alpha1, alpha2)
%gth=alpha1-1/2*log(Rl*Rl1*Rr*Rr1);
Rth_0=exp(-2*(g0-alpha1))/Rl/Rl1/Rr1/Rl2/Rr2;
R0=Rth_0+1e-7;%initial guess
dR=0.0001;
c1=1; % initial guess
dc=0.0001;
zspan=0:0.01:1;
r=linspace(0,1,200);
count_max=20;
count=0;
f0=HOMthreshold_calc_fiber(g0, c1, dc, Rl, Rl1, Rl2, R0, Rr1, Rr2, alpha1, alpha
2, zspan, r);

while abs(f0)>1e-7&&count<count_max
R1=R0+dR;
f1=HOMthreshold_calc_fiber(g0, c1, dc, Rl, Rl1, Rl2, R1, Rr1, Rr2, alpha1, alpha
2, zspan, r);
R0=abs(R0+f0/(f0-f1)*dR);
f0=HOMthreshold_calc_fiber(g0, c1, dc, Rl, Rl1, Rl2, R0, Rr1, Rr2, alpha1, alpha
2, zspan, r);
count=count+1;
end
R=R0;
end

function R=Rth_1R(g0, Rl, Rl1, Rl2, Rr1, Rr2, alpha1, alpha2)
R0=0.999;%initial guess
dR=0.0001;
c1=1; % initial guess
dc=0.0001;
zspan=0:0.01:1;
r=linspace(0,1,200);
count_max=20;
count=0;
f0=HOMthreshold_calc_fiber(g0, c1, dc, Rl, Rl1, Rl2, R0, Rr1, Rr2, alpha1, alpha
2, zspan, r);

while abs(f0)>1e-7&&count<count_max
R1=R0+dR;
f1=HOMthreshold_calc_fiber(g0, c1, dc, Rl, Rl1, Rl2, R1, Rr1, Rr2, alpha1, alpha
2, zspan, r);
R0=abs(R0+f0/(f0-f1)*dR);

```

```

f0=HOMthreshold_calc_fiber(g0,c1,dc,Rl,Rl1,Rl2,R0,Rr1,Rr2,alpha1,alpha
2,zspan,r);
count=count+1;
end
R=R0;
end

% Calculate  $\eta_{SM}^{max}$  vs.  $R_{opt}$  for a fixed distributive loss and different
single-pass gains. The whole figure is constructed by running
different sets of distributive loss and single-pass gains.

clear all
clc
g=[1;2;3;4;6;8;10];
alpha1=0.001;
alpha2=2.54*alpha1;
Rl=1;Rl1=1;Rl2=1;Rr1=1;Rr2=1;
% alpha 0.001
%Rth1_L=[0.137104539 0.018537342 0.002509387 0.000363816 0 0 0];
%Rth1_R=[0.997771086 0.997844562 0.997876191 0.997894796 0.997916624
0.997929497 0.997938208];

% alpha 0.01
%Rth1_L=[0.15273407 0.020637258 0.0027924 0.000378294 0 0 0];
%Rth1_R=[0.971420143 0.974516771 0.975727953 0.976410988 0.97718759
0.977634567 0.977933212];

% alpha 0.02
%Rth1_L=[0.173723777 0.023344656 0.003155555 0.000426982 0 0 0];
%Rth1_R=[0.932792135 0.943656657 0.94755588 0.949683196 0.952044833
0.953378342 0.954259384];

% alpha 0.03
%Rth1_L=[0.199756974 0.026521261 0.003577984 0.000483992 0 0 0];
%Rth1_R=[0.884415174 0.908724775 0.916686881 0.920901052 0.925482238
0.928027321 0.929693314];

% alpha 0.046656629
%Rth1_L=[0.26234566 0.033161837 0.004444985 0.000600517 0 0 0];
%Rth1_R=[0.775380539 0.842415484 0.860421075 0.869475286 0.87900567
0.884175077 0.887514117];

% alpha 0.05
%Rth1_L=[0.279988056 0.034748294 0.004648375 0.000627767 0 0 0];
%Rth1_R=[0.747087113 0.827920646 0.84848331 0.858714007 0.869414792
0.875191953 0.878914858];

% alpha 0.093304
%Rth1_L=[0 0.069490287 0.008651348 0.00115404 0 0 0];
%Rth1_R=[0 0.601262259 0.677816666 0.709696153 0.740352132 0.756012724
0.765825182];

% alpha 0.1
%Rth1_L=[0 0.079208167 0.009600357 0.001275461 0 0 0];

```

```
%Rth1_R=[0 0.558120075 0.649091757 0.685451261 0.719923955 0.737389267  
0.748290186];  
  
% alpha 0.12  
%Rth1_L=[0 0.129755231 0.013323729 0.001737328 0 0 0];  
%Rth1_R=[0 0.402367657 0.559999518 0.611815186 0.658726248 0.681912223  
0.696224969];  
  
% alpha 0.1399  
%Rth1_L=[0 0 0.019082115 0.002402463 0.000182219 0 0];  
%Rth1_R=[0 0 0.466452562 0.537327299 0.59803759 0.627299704  
0.645179062];  
  
% alpha 0.15  
%Rth1_L=[0 0 0.023320932 0.002852533 0 0 0];  
%Rth1_R=[0 0 0.416869984 0.499277641 0.567490802 0.599939597  
0.619668107];  
  
% alpha 0.186339  
%Rth1_L=[0 0 0.06219924 0.0055716 9.28E-05 0 0];  
%Rth1_R=[0 0 0.212705553 0.36235962 0.460170638 0.504336685  
0.530748868];  
  
% alpha 0.2  
%Rth1_L=[0 0 0 0.007376072 0.000123424 0 0];  
%Rth1_R=[0 0 0 0.311188575 0.421254567 0.469812335 0.498684645];  
  
% alpha 0.277985  
%Rth1_L=[0 0 0 0 0.000593689 0 0];  
%Rth1_R=[0 0 0 0 0.221003875 0.292143201 0.33323252];  
  
% alpha 0.366282  
%Rth1_L=[0 0 0 0 0.007437522 8.40E-05 0];  
%Rth1_R=[0 0 0 0 0.047447394 0.138667255 0.187183831];  
  
% alpha 0.4  
%Rth1_L=[0 0 0 0 0 0.000203346 0];  
%Rth1_R=[0 0 0 0 0 0.094263388 0.143436492];  
  
% alpha 0.44936  
%Rth1_L=[0 0 0 0 0 0 0];  
%Rth1_R=[0 0 0 0 0 0 0];  
  
% alpha 0.54  
%Rth1_L=[0 0 0 0 0 0 0];  
%Rth1_R=[0 0 0 0 0 0 0];  
  
% alpha 0.63  
%Rth1_L=[0 0 0 0 0 0 0];  
%Rth1_R=[0 0 0 0 0 0 0];  
  
% alpha 0.7  
%Rth1_L=[0 0 0 0 0 0 0];  
%Rth1_R=[0 0 0 0 0 0 0];
```

```

% alpha 1
Rth1_L=[0 0 0 0 0 0 0];
Rth1_R=[0 0 0 0 0 0 0];

eita=zeros(length(g),1);
Ropt=zeros(length(g),1);

for m=1:length(g)

[Rout,I1l_out]=Iout_vs_R_fiber(g(m),Rl,Rl1,Rl2,Rr1,Rr2,alpha1,Rth1_L(m)
),Rth1_R(m));
    %figure
    %plot(Rout,I1l_out/g(m))
    for ii=1:length(I1l_out)
        if I1l_out(ii)>g(m)
            I1l_out(ii)=0;
        end
    end
    n=find(max(I1l_out)==I1l_out);
    Ropt(m)=Rout(n);
    eita(m)=I1l_out(n)/g(m);
end

figure
plot(Ropt,eita)

```

Table 5 Matlab code for calculation of the trace of kink points in Figure 5-2 (refer to Table 5-1), for uniformly side-pumped IAG fiber lasers

```

clear all
clc
g0=0.21433;
dg=0.0002;
dR=0.0001;
alpha1=0.01;
alpha2=2.54*alpha1;
Rl=1;Rl1=1;Rl2=1;Rr1=1;Rr2=1;
count_max2=20;
c1=1;% initial guess
dc=0.0001;
zspan=0:0.01:1;

% obtain Rth_1R
Rr_goal=Rth_1R(g0,Rl,Rl1,Rl2,Rr1,Rr2,alpha1,alpha2);
Ropt=Optimal_R_fiber(g0,c1,dc,dR,Rr_goal,Rl,Rl1,Rl2,Rr1,Rr2,alpha1,alpha2,zspan);
fg0=Ropt-Rr_goal;
count2=0;
while abs(fg0)>1e-9&&count2<count_max2
    g1=g0+dg;

```

```

Rr_goal=Rth_1R(g1,Rl,Rl1,Rl2,Rr1,Rr2,alpha1,alpha2);

Ropt=Optimal_R_fiber(g1,c1,dc,dR,Rr_goal,Rl,Rl1,Rl2,Rr1,Rr2,alpha1,alpha2,zspan);
    fg1=Ropt-Rr_goal;
    g0=abs(g0+fg0/(fg0-fg1)*dg);
    Rr_goal=Rth_1R(g0,Rl,Rl1,Rl2,Rr1,Rr2,alpha1,alpha2);

Ropt=Optimal_R_fiber(g0,c1,dc,dR,Rr_goal,Rl,Rl1,Rl2,Rr1,Rr2,alpha1,alpha2,zspan);
    fg0=Ropt-Rr_goal;
    count2=count2+1;
end
g0 % single-pass gain at the kink point
eta=Iout_1D1M_fiber(g0,c1,dc,Rl,Rl1,Rr_goal,Rr1,alpha1,zspan)/g0 %
extraction efficiency at the kink point
-log(Rr_goal)/alpha1 % last column of Table 5-2

function
Ropt=Optimal_R_fiber(g0,c1,dc,dR,Rr,Rl,Rl1,Rl2,Rr1,Rr2,alpha1,alpha2,zspan)
df0=(Iout_1D1M_fiber(g0,c1,dc,Rl,Rl1,Rr+dR/2,Rr1,alpha1,zspan)-
Iout_1D1M_fiber(g0,c1,dc,Rl,Rl1,Rr-dR/2,Rr1,alpha1,zspan))/dR/g0;
count1=0;
count_max1=10;
while abs(df0)>1e-6&&count1<count_max1
df1=(Iout_1D1M_fiber(g0,c1,dc,Rl,Rl1,Rr+3*dR/2,Rr1,alpha1,zspan)-
Iout_1D1M_fiber(g0,c1,dc,Rl,Rl1,Rr+dR/2,Rr1,alpha1,zspan))/dR/g0;
Rr=abs(Rr+df0/(df0-df1)*dR);
df0=(Iout_1D1M_fiber(g0,c1,dc,Rl,Rl1,Rr+dR/2,Rr1,alpha1,zspan)-
Iout_1D1M_fiber(g0,c1,dc,Rl,Rl1,Rr-dR/2,Rr1,alpha1,zspan))/dR/g0;
count1=count1+1;
end
Ropt=Rr;
    end

```

Table 6 Matlab code for Figure 5-3 (contour plot of gain threshold ratio g_2^{th} / g_1^{th} , as a function of $\alpha_1 L$ and R_{oc} , in core-pumped IAG fiber lasers)

```

clear all
clc
N=1e26;% doping density, unit m-3
sigma_ap=0.7e-24;sigma_ep=3.76e-26;% unit m^2
c=299792458; % speed of light (m)
lambda_p=8.03e-7;% pump wavelength (m)
v_p=c/lambda_p;
sigma_as=7.82e-26;sigma_es=4.4e-24;% unit m^2
lambda_s=1.053e-6;% signal wavelength (m)
v_s=c/lambda_s;
tau=1.9e-4;
L=0.1;% cavity length (m)
a=100e-6;% core radius (m)

```

```

Acore=pi*a^2;
Tau_p=1/Acore;
Rl=1;Rl1=1;Rl2=1;Rr1=1;Rr2=1;
gr=10; % set gain threshold ratio

alpha_1L=[linspace(0.001,0.04,64) linspace(0.045,0.2,8)
linspace(0.21,1.5,64)];
alpha_1=alpha_1L/L;
alpha_2=2.54*alpha_1;
alpha_p=(lambda_p/lambda_s)^2*alpha_1;

Rth=zeros(length(alpha_1),1);
parfor m=1:length(alpha_1)
Rth(m)=Rth_gratio_fiber(gr,Rl,Rl1,Rl2,Rr1,Rr2,N,sigma_ap,sigma_ep,lambda_p,sigma_as,sigma_es,lambda_s,tau,alpha_p(m),alpha_1(m),alpha_2(m),L,a,Tau_p);
end

figure
semilogy(Rth,alpha_1L)
xlim([0 1])
ylim([1e-3 10])

function
R=Rth_gratio_fiber(gr,Rl,Rl1,Rl2,Rr1,Rr2,N,sigma_ap,sigma_ep,lambda_p,sigma_as,sigma_es,lambda_s,tau,alpha_p,alpha_1,alpha_2,L,a,Tau_p)
h=6.626e-34;% Planck constant
c=299792458; % speed of light (m)
v_p=c/lambda_p;
v_s=c/lambda_s;
R0=0.0001;%R0=0.00001;% initial guess of Rr
gth_FM=alpha_1*L-1/2*log(Rl*Rl1*R0*Rr1);%FM gain threshold
g_L0=gth_FM*gr;
Pp0=(g_L0+N*L*sigma_as)*(h*v_p)*(sigma_ap*N+alpha_p)/(N*sigma_ap*tau*(sigma_as+sigma_es)*Tau_p)/(1-exp(-(sigma_ap*N+alpha_p)*L));% input pump power (W)
guess=0.5*g_L0;
c1=(-guess/log(Rr1*R0))^2*Rr1*R0;

dR=0.00001;%dR=0.000001;
dc=0.1;
zspan=0:0.01:1;
r=linspace(0,1,200);
count_max=20;
count=0;
%f0=HOMthreshold_calc_fiber(g_L0,c1,dc,Rl,Rl1,Rl2,R0,Rr1,Rr2,alpha1,alpha2,zspan,r);
f0=HOMthreshold_calc_fiber_endpump_R(zspan,r,N,sigma_ap,sigma_ep,lambda_p,sigma_as,sigma_es,lambda_s,tau,alpha_p,alpha_1,alpha_2,L,a,c1,dc,Rl,Rl1,Rl2,R0,Rr1,Rr2,Pp0);

while abs(f0)>1e-7&&count<count_max
Rl=R0+dR;
gth_FM=alpha_1*L-1/2*log(Rl*Rl1*Rl1*Rr1);%FM gain threshold

```

```

g_L0=gth_FM*gr;
Pp0=(g_L0+N*L*sigma_as)*(h*v_p)*(sigma_ap*N+alpha_p)/(N*sigma_ap*tau*(
sigma_as+sigma_es)*Tau_p)/(1-exp(-(sigma_ap*N+alpha_p)*L));% input
pump power (W)
guess=0.5*g_L0;
c1=(-guess/log(Rr1*R1))^2*Rr1*R1;
f1=HOMthreshold_calc_fiber_endpump_R(zspan,r,N,sigma_ap,sigma_ep,lambd
a_p,sigma_as,sigma_es,lambdas,tau,alpha_p,alpha_1,alpha_2,L,a,c1,dc,R
l,Rl1,Rl2,R1,Rr1,Rr2,Pp0);

R0=abs(R0+f0/(f0-f1)*dR);
gth_FM=alpha_1*L-1/2*log(Rl*Rl1*R0*Rr1);%FM gain threshold
g_L0=gth_FM*gr;
Pp0=(g_L0+N*L*sigma_as)*(h*v_p)*(sigma_ap*N+alpha_p)/(N*sigma_ap*tau*(
sigma_as+sigma_es)*Tau_p)/(1-exp(-(sigma_ap*N+alpha_p)*L));% input
pump power (W)
guess=0.5*g_L0;
c1=(-guess/log(Rr1*R0))^2*Rr1*R0;
f0=HOMthreshold_calc_fiber_endpump_R(zspan,r,N,sigma_ap,sigma_ep,lambd
a_p,sigma_as,sigma_es,lambdas,tau,alpha_p,alpha_1,alpha_2,L,a,c1,dc,R
l,Rl1,Rl2,R0,Rr1,Rr2,Pp0);

count=count+1;
end
R=R0;
end

function
f=HOMthreshold_calc_fiber_endpump_R(zspan,r,N,sigma_ap,sigma_ep,lambd
_p,sigma_as,sigma_es,lambdas,tau,alpha_p,alpha_1,alpha_2,L,a,c1,dc,Rl
,Rl1,Rl2,Rr,Rr1,Rr2,Pp0)
c=299792458;% speed of light (m)
h=6.626e-34;% Planck constant
v_p=c/lambdap;
v_s=c/lambdas;
count_max=40;
count=0;
j01=2.4048;j11=3.8317;
%const1=2*pi*trapz(r,besselj(0,j01*r).^2.*r);
%const2=2*pi*trapz(r,besselj(1,j11*r).^2.*r);
const1=0.846708366684588*a^2;
const2=0.509615451400111*a^2;
Tau_s1=abs(besselj(0,j01*r).^2)/const1;
Tau_s2=abs(besselj(1,j11*r).^2)/const2;
Acore=pi*a^2;
Psat=(h*v_s)*Acore/((sigma_as+sigma_es)*tau);
g0=N*(Pp0*exp(-(sigma_ap*N+alpha_p)*L*zspan)*sigma_ap/Psat*(v_s/v_p)-
sigma_as);% g0(z)

Ps0=sqrt(c1*Rl*Rl1);PsL=sqrt(c1/Rr/Rr1);
[z,P] = ode45(@ (z,P)
IAG_fiber_onemode_endpump_R(z,P,r,N,sigma_ap,sigma_ep,v_p,sigma_as,sig
ma_es,v_s,tau,alpha_p,alpha_1,L,a,c1,Pp0),zspan,Ps0);
dif_1=P(end)-PsL;
while abs(dif_1)>1e-6&&count<count_max

```

```

    dc=min(dc,c1/100);
    c11=c1+dc;
    Ps0=sqrt(c11*Rl*Rl1);PsL=sqrt(c11/Rr/Rr1);
    [z,P] = ode45(@ (z,P)
IAG_fiber_onemode_endpump_R(z,P,r,N,sigma_ap,sigma_ep,v_p,sigma_as,sig
ma_es,v_s,tau,alpha_p,alpha_1,L,a,c11,Pp0),zspan,Ps0);
    dif_11=P(end)-PsL;

    c1=abs(c1+dif_1/(dif_1-dif_11)*dc);
    Ps0=sqrt(c1*Rl*Rl1);PsL=sqrt(c1/Rr/Rr1);
    [z,P] = ode45(@ (z,P)
IAG_fiber_onemode_endpump_R(z,P,r,N,sigma_ap,sigma_ep,v_p,sigma_as,sig
ma_es,v_s,tau,alpha_p,alpha_1,L,a,c1,Pp0),zspan,Ps0);
    dif_1=P(end)-PsL;

    count=count+1;
end
Pz=P+c1./P;
int_z=zeros(length(Pz),1);
for ii=1:length(Pz)
    F=2*pi*a^2* Tau_s2.*r./(1+Tau_s1*Acore*Pz(ii));
    int_z(ii)=trapz(r,F);
end
LHS=trapz(zspan,g0'.*int_z*L);
RHS=alpha_2*L-0.5*log(Rl*Rr*Rl2*Rr2);
f=LHS-RHS;

end

function dPdz =
IAG_fiber_onemode_endpump_R(z,P,r,N,sigma_ap,sigma_ep,v_p,sigma_as,sig
ma_es,v_s,tau,alpha_p,alpha_1,L,a,c1,Pp0)
h=6.626e-34;% Planck constant
j01=2.4048;
%const1=2*pi*trapz(r,besselj(0,j01*r).^2.*r);
const1=0.846708366684588*a^2;
Tau_s1=abs(besselj(0,j01*r).^2)/const1;
Acore=pi*a^2;
Psat=(h*v_s)*Acore/((sigma_as+sigma_es)*tau);
g0=N*(Pp0*exp(-(sigma_ap*N+alpha_p)*L*z)*sigma_ap/Psat*(v_s/v_p)-
sigma_as);
int1=g0*L*Tau_s1.*r*a^2./(1+Tau_s1*Acore*(P+c1/P));
integrall=2*pi*trapz(r,int1);
dPdz=P*integrall-alpha_1*L*P;
end

```

Table 7 Matlab code for calculation of Figure 5-4 (η_{SM}^{\max} vs. R_{opt} in core-pumped IAG fiber lasers)

```

% Calculate the range of output coupler [Rth_1, Rth_1R] for single-
mode operation, for given single-pass gain and distributive loss.

clear all
clc

r=linspace(0,1,200);
zspan=0:0.01:1;
N=1e26;% doping density, unit m-3
sigma_ap=0.7e-24;sigma_ep=3.76e-26;% unit m^2
c=299792458; % speed of light (m)
lambda_p=8.03e-7;% pump wavelength (m)
v_p=c/lambda_p;
sigma_as=7.82e-26;sigma_es=4.4e-24;% unit m^2
lambda_s=1.053e-6;% signal wavelength (m)
v_s=c/lambda_s;
tau=1.9e-4;
a=100e-6;% core radius (m)

Rl=1;Rl1=1;Rl2=1;Rr1=1;Rr2=1;
g_L=[1 2 3 4 6 8 10];

alpha1=1.6*0;% absorption (m^-1)
alpha2=1.6*0;
alphap=1.6*0;

L=0.1;
%Alpha1=0.39796/L;
Alpha1=0.01/L;
alpha_1=Alpha1+alpha1;
alpha_2=2.54*Alpha1+alpha2;
alpha_p=(lambda_p/lambda_s)^2*Alpha1+alphap

Rth1L=zeros(length(g_L),1);
Rth1R=zeros(length(g_L),1);
parfor m=1:length(g_L)

Rth1L(m)=Rth_1L_endpump_R(zspan,r,N,sigma_ap,sigma_ep,lambda_p,sigma_a
s,sigma_es,lambda_s,tau,g_L(m),Rl,Rl1,Rl2,Rr1,Rr2,alpha_1,alpha_2,alph
a_p,L,a);

Rth1R(m)=Rth_1R_endpump_R(zspan,r,N,sigma_ap,sigma_ep,lambda_p,sigma_a
s,sigma_es,lambda_s,tau,g_L(m),Rl,Rl1,Rl2,Rr1,Rr2,alpha_1,alpha_2,alph
a_p,L,a);
end
figure
plot(g_L,Rth1L,g_L,Rth1R,'r')

```

```

function
R=Rth_1L_endpump_R(zspan,r,N,sigma_ap,sigma_ep,lambda_p,sigma_as,sigma
_es,lambda_s,tau,g_L,Rl,Rl1,Rl2,Rr1,Rr2,alpha_1,alpha_2,alpha_p,L,a)
%gth=alpha1-1/2*log(Rl*Rl1*Rr*Rr1);
Rth_0=exp(-2*(g_L-alpha_1*L))/Rl/Rl1/Rr1/Rl2/Rr2;
R0=Rth_0+1e-5;%initial guess
h=6.626e-34;% Planck constant
c=299792458; % speed of light (m)
v_p=c/lambda_p;
Acore=pi*a^2;
Tau_p=1/Acore;
dc=0.1;dR=0.0001;

guess=0.5*g_L;
Pp0=(g_L+N*L*sigma_as)*(h*v_p)*(sigma_ap*N+alpha_p)/(N*sigma_ap*tau*(s
igma_as+sigma_es)*Tau_p)/(1-exp(-(sigma_ap*N+alpha_p)*L));% input pump
power (W)
c1=(-guess/log(Rr1*R0))^2*Rr1*R0;
f0=HOMthreshold_calc_fiber_endpump_R(zspan,r,N,sigma_ap,sigma_ep,lambda
_p,sigma_as,sigma_es,lambda_s,tau,alpha_p,alpha_1,alpha_2,L,a,c1,dc,R
l,Rl1,Rl2,R0,Rr1,Rr2,Pp0);
count=0;
count_max=20;

while abs(f0)>1e-7&&count<count_max
Rl=R0+dR;
c1=(-guess/log(Rr1*Rl))^2*Rr1*Rl;
f1=HOMthreshold_calc_fiber_endpump_R(zspan,r,N,sigma_ap,sigma_ep,lambda
_p,sigma_as,sigma_es,lambda_s,tau,alpha_p,alpha_1,alpha_2,L,a,c1,dc,R
l,Rl1,Rl2,Rl,Rr1,Rr2,Pp0);

R0=abs(R0+f0/(f0-f1)*dR);
c1=(-guess/log(Rr1*R0))^2*Rr1*R0;
f0=HOMthreshold_calc_fiber_endpump_R(zspan,r,N,sigma_ap,sigma_ep,lambda
_p,sigma_as,sigma_es,lambda_s,tau,alpha_p,alpha_1,alpha_2,L,a,c1,dc,R
l,Rl1,Rl2,R0,Rr1,Rr2,Pp0);

count=count+1;
end
R=R0;
end

function
R=Rth_1R_endpump_R(zspan,r,N,sigma_ap,sigma_ep,lambda_p,sigma_as,sigma
_es,lambda_s,tau,g_L,Rl,Rl1,Rl2,Rr1,Rr2,alpha_1,alpha_2,alpha_p,L,a)
R0=0.999;%initial guess
h=6.626e-34;% Planck constant
c=299792458; % speed of light (m)
v_p=c/lambda_p;
Acore=pi*a^2;
Tau_p=1/Acore;
dc=0.1;dR=0.0001;

guess=0.5*g_L;

```

```

Pp0=(g_L+N*L*sigma_as)*(h*v_p)*(sigma_ap*N+alpha_p)/(N*sigma_ap*tau*(s
igma_as+sigma_es)*Tau_p)/(1-exp(-(sigma_ap*N+alpha_p)*L));% input pump
power (W)
c1=(-guess/log(Rr1*R0))^2*Rr1*R0;
f0=HOMthreshold_calc_fiber_endpump_R(zspan,r,N,sigma_ap,sigma_ep,lambd
a_p,sigma_as,sigma_es,lambda_s,tau,alpha_p,alpha_1,alpha_2,L,a,c1,dc,R
l,Rl1,Rl2,R0,Rr1,Rr2,Pp0);
count=0;
count_max=20;

while abs(f0)>1e-7&&count<count_max
Rl=R0+dR;
c1=(-guess/log(Rr1*Rl))^2*Rr1*Rl;
f1=HOMthreshold_calc_fiber_endpump_R(zspan,r,N,sigma_ap,sigma_ep,lambd
a_p,sigma_as,sigma_es,lambda_s,tau,alpha_p,alpha_1,alpha_2,L,a,c1,dc,R
l,Rl1,Rl2,Rl,Rr1,Rr2,Pp0);

R0=abs(R0+f0/(f0-f1)*dR);
c1=(-guess/log(Rr1*R0))^2*Rr1*R0;
f0=HOMthreshold_calc_fiber_endpump_R(zspan,r,N,sigma_ap,sigma_ep,lambd
a_p,sigma_as,sigma_es,lambda_s,tau,alpha_p,alpha_1,alpha_2,L,a,c1,dc,R
l,Rl1,Rl2,R0,Rr1,Rr2,Pp0);

count=count+1;
end
R=R0;
end

% Calculate  $\eta_{SM}^{max}$  vs.  $R_{opt}$  for a fixed distributive loss and different
single-pass gains. The whole figure is constructed by running
different sets of distributive loss and single-pass gains.

clear all
clc
h=6.626e-34;% Planck constant
r=linspace(0,1,200);
zspan=0:0.01:1;
N=1e26;% doping density, unit m-3
sigma_ap=0.7e-24;sigma_ep=3.76e-26;% unit m^2
c=299792458;% speed of light (m)
lambda_p=8.03e-7;% pump wavelength (m)
v_p=c/lambda_p;
sigma_as=7.82e-26;sigma_es=4.4e-24;% unit m^2
lambda_s=1.053e-6;% signal wavelength (m)
v_s=c/lambda_s;
tau=1.9e-4;
L=0.1;% cavity length (m)
a=100e-6;% core radius (m)
Acore=pi*a^2;
Tau_p=1/Acore;
alpha1=1.6*0;% absorpion coef. (m^-1)
alphap=1.6*0;
n0=1.5734;
dn=-0.0045;
% input alpha

```

```

Alpha1=0.4/L;

alpha_1=Alpha1+alpha1;
alpha_p=(lambda_p/lambda_s)^2*Alpha1+alphap;
Rl1=1;Rr1=1;Rl=1;%Rr=linspace(0.1,0.99,96);

g_L=[1;2;3;4;6;8;10];

% alpha 0.001
%Rth1_L=[0.136482427 0.018412845 0.002487186 0.000341852 0 0 0];
%Rth1_R=[0.997778599 0.997850205 0.997881225 0.997899525 0.997921047
0.997933767 0.997942381];

% alpha 0.01
%Rth1_L=[0.151986565 0.020485135 0.002764805 0.000373098 0 0 0];
%Rth1_R=[0.971520539 0.974584761 0.975786003 0.976464243 0.977236069
0.977680612 0.977977773];

% alpha 0.02
%Rth1_L=[0.172853532 0.02316859 0.003123211 0.000421426 0 0 0];
%Rth1_R=[0.933042062 0.943809661 0.947682292 0.94979716 0.952146632
0.953474032 0.954351361];

% alpha 0.03
%Rth1_L=[0.19871 0.02631972 0.003540711 0.000477538 0 0 0];
%Rth1_R=[0.884880773 0.908977794 0.916889411 0.921080655 0.925640099
0.928174477 0.929834014];

% alpha 0.04661
%Rth1_L=[0.260544504 0.032886617 0.004395657 0.000592035 0 0 0];
%Rth1_R=[0.776869277 0.843066857 0.860929089 0.869921406 0.879393911
0.884534823 0.887856458];

% alpha 0.05
%Rth1_L=[0.278223483 0.03448509 0.004599963 0.000619258 0 0 0];
%Rth1_R=[0.74843558 0.828419269 0.848857369 0.859036013 0.869689984
0.875444801 0.879154295];

% alpha 0.092352
%Rth1_L=[0 0.067812799 0.008455148 0.001124122 0 0 0];
%Rth1_R=[0 0.608493978 0.682665379 0.713777823 0.74378148 0.759135834
0.768764763];

% alpha 0.1
%Rth1_L=[0 0.078696533 0.009527925 0.001260877 0 0 0];
%Rth1_R=[0 0.559681329 0.649990697 0.686168192 0.720499471 0.737903511
0.748769572];

% alpha 0.12
%Rth1_L=[0 0.12872985 0.013258269 0.001721804 5.30E-05 0 0];
%Rth1_R=[0 0.405031509 0.561134519 0.612692863 0.65941597 0.682523622
0.696792476];

% alpha 0.1368406

```

```
%Rth1_L=[0 0 0.017971584 0.002269661 8.61E-06 0 0];
%Rth1_R=[0 0 0.482505021 0.549832599 0.608110116 0.636327102
0.653599475];

% alpha 0.15
%Rth1_L=[0 0 0.023338379 0.002844833 3.42E-05 0 0];
%Rth1_R=[0 0 0.418339969 0.500365092 0.568330553 0.600679413
0.620352537];

% alpha 0.179723
%Rth1_L=[0 0 0.049280531 0.004931086 8.47E-05 0 0];
%Rth1_R=[0 0 0.257725387 0.388401404 0.480273684 0.522193658
0.547337819];

% alpha 0.2
%Rth1_L=[0 0 0 0.007496341 0.000123088 0 0];
%Rth1_R=[0 0 0 0.312286461 0.422216844 0.470683439 0.499500157];

% alpha 0.2600366
%Rth1_L=[0 0 0 0 0.000416274 0 0];
%Rth1_R=[0 0 0 0 0.263896797 0.330551398 0.369229761];

% alpha 0.3
%Rth1_L=[0 0 0 0 0.001058807 0 0];
%Rth1_R=[0 0 0 0 0.172274786 0.249253149 0.293127109];

% alpha 0.332555
%Rth1_L=[0 0 0 0 0.002583083 2.33E-05 0];
%Rth1_R=[0 0 0 0 0.106268033 0.190777479 0.237828843];

% alpha 0.39796
%Rth1_L=[0 0 0 0 0 0.000229977 0];
%Rth1_R=[0 0 0 0 0 0.094736594 0.14506471];

% alpha 0.4
Rth1_L=[0 0 0 0 0 0.00024438 0];
Rth1_R=[0 0 0 0 0 0.092191052 0.142558099];

% alpha 0.5
%Rth1_L=[0 0 0 0 0 0 0];
%Rth1_R=[0 0 0 0 0 0 0];

% alpha 0.6
%Rth1_L=[0 0 0 0 0 0 0];
%Rth1_R=[0 0 0 0 0 0 0];

% alpha 0.7
%Rth1_L=[0 0 0 0 0 0 0];
%Rth1_R=[0 0 0 0 0 0 0];

% alpha 0.8
%Rth1_L=[0 0 0 0 0 0 0];
%Rth1_R=[0 0 0 0 0 0 0];
```

```

% alpha 0.9
%Rth1_L=[0 0 0 0 0 0 0];
%Rth1_R=[0 0 0 0 0 0 0];

% alpha 1
%Rth1_L=[0 0 0 0 0 0 0];
%Rth1_R=[0 0 0 0 0 0 0];

eita=zeros(length(g_L),1);
Ropt=zeros(length(g_L),1);

for m=1:length(g_L)

[Rout,Pout]=Pout_vs_R_IAG_fiber_onemode_endpump_R(N,sigma_ap,sigma_ep,
lambda_p,sigma_as,sigma_es,lambda_s,tau,alpha_p,alpha_1,L,a,Rl,Rl1,Rr1
,g_L(m),Rth1_L(m),Rth1_R(m));
    %figure
    %plot(Rout,Pout/g_L(m))
    %hold on
    for ii=1:length(Pout)
        if Pout(ii)>g_L(m)
            Pout(ii)=0;
        end
    end
    n=find(max(Pout)==Pout);
    Ropt(m)=Rout(n);
    eita(m)=Pout(n)/g_L(m);
end

figure
plot(Ropt,eita)

function
[Rout,Pout]=Pout_vs_R_IAG_fiber_onemode_endpump_R(N,sigma_ap,sigma_ep,
lambda_p,sigma_as,sigma_es,lambda_s,tau,alpha_p,alpha_1,L,a,Rl,Rl1,Rr1
,g_L,Rth1_L,Rth1_R)
h=6.626e-34;% Planck constant
r=linspace(0,1,200);
zspan=0:0.01:1;
c=299792458; % speed of light (m)
v_p=c/lambda_p;
%v_s=c/lambda_s;
Acore=pi*a^2;
Tau_p=1/Acore;
Pp0=(g_L+N*L*sigma_as)*(h*v_p)*(sigma_ap*N+alpha_p)/(N*sigma_ap*tau*(s
igma_as+sigma_es)*Tau_p)/(1-exp(-(sigma_ap*N+alpha_p)*L));% input pump
power (W)
dR=0.001;
Rth0=exp(2*(alpha_1*L-g_L))/Rl/Rl1/Rr1;
if Rth1_L~=0&&Rth1_R~=0
    Rout=[linspace(Rth0+1e-5,Rth1_L,max(ceil((Rth1_L-Rth0)/dR),200))
linspace(Rth1_R,0.9999,max(ceil((0.9999-Rth1_R)/dR),200))];
elseif Rth1_L==0&&Rth1_R~=0
    Rout=linspace(Rth1_R,0.9999,max(ceil((0.9999-Rth1_R)/dR),200));
else

```

```

Rout=linspace(Rth0,0.9999,max(ceil((0.9999-Rth0)/dR),200));
end
%Rout=Rout(2:end-1);
Pout=zeros(length(Rout),1);
guess=0.5*g_L;
dc=0.0001;
c1=(-guess./log(Rr1*Rout)).^2*Rr1.*Rout;

parfor m=1:length(Rout)

Pout(m)=Pout_IAG_fiber_onemode_endpump_R(zspan,r,N,sigma_ap,sigma_ep,lamb
da_p,sigma_as,sigma_es,lambdas,tau,alpha_p,alpha_1,L,a,c1(m),dc,Rl,Rl1,Rout(m),Rr1,Pp0);
end

end

function Pout =
Pout_IAG_fiber_onemode_endpump_R(zspan,r,N,sigma_ap,sigma_ep,lambdas,
sigma_as,sigma_es,lambdas,tau,alpha_p,alpha_1,L,a,c1,dc,Rl,Rl1,Rr,Rr1
,Pp0)
c=299792458; % speed of light (m)
v_p=c/lambdas_p;
v_s=c/lambdas_s;
count_max=40;
count=0;

Ps0=sqrt(c1*Rl*Rl1);PsL=sqrt(c1/Rr/Rr1);
[z,P] = ode45(@(z,P)
IAG_fiber_onemode_endpump_R(z,P,r,N,sigma_ap,sigma_ep,v_p,sigma_as,sig
ma_es,v_s,tau,alpha_p,alpha_1,L,a,c1,Pp0),zspan,Ps0);
dif_1=P(end)-PsL;
Pout=0;
while abs(dif_1)>1e-6&&count<count_max
dc=min(dc,c1/100);
c1=c1+dc;
Ps0=sqrt(c1*Rl*Rl1);PsL=sqrt(c1/Rr/Rr1);
[z,P] = ode45(@(z,P)
IAG_fiber_onemode_endpump_R(z,P,r,N,sigma_ap,sigma_ep,v_p,sigma_as,sig
ma_es,v_s,tau,alpha_p,alpha_1,L,a,c1,Pp0),zspan,Ps0);
dif_11=P(end)-PsL;

c1=abs(c1+dif_1/(dif_1-dif_11)*dc);
Ps0=sqrt(c1*Rl*Rl1);PsL=sqrt(c1/Rr/Rr1);
[z,P] = ode45(@(z,P)
IAG_fiber_onemode_endpump_R(z,P,r,N,sigma_ap,sigma_ep,v_p,sigma_as,sig
ma_es,v_s,tau,alpha_p,alpha_1,L,a,c1,Pp0),zspan,Ps0);
dif_1=P(end)-PsL;

count=count+1;
end
if count~=count_max
Pout=PsL*(1-Rr);
end
%figure

```

```

%plot(z,P(:,1),z,P(:,2),'r')
end

```

Table 8 Matlab code for calculation of the trace of kink point in Figure 5-4 (refer to Table 5-4), for core-pumped IAG fiber lasers

```

clear all
clc
g0_L=10;% initial guess of g_L
dg=0.0002;
Rl=1;Rl1=1;Rl2=1;Rr1=1;Rr2=1;
r=linspace(0,1,200);
zspan=0:0.01:1;
N=1e26;% doping density, unit m-3
sigma_ap=0.7e-24;sigma_ep=3.76e-26;% unit m^2
c=299792458; % speed of light (m)
lambda_p=8.03e-7;% pump wavelength (m)
v_p=c/lambda_p;
sigma_as=7.82e-26;sigma_es=4.4e-24;% unit m^2
lambda_s=1.053e-6;% signal wavelength (m)
v_s=c/lambda_s;
tau=1.9e-4;
a=100e-6;% core radius (m)

alpha1=1.6*0;% absorption coef. (m^-1)
alpha2=1.6*0;
alphap=1.6*0;

L=0.1;
Alpha1=0.39796/L;
alpha_1=Alpha1+alpha1;
alpha_2=2.54*Alpha1+alpha2;
alpha_p=(lambda_p/lambda_s)^2*Alpha1+alphap;

% obtain Rth_R
Rr_goal=Rth_1R_endpump_R(zspan,r,N,sigma_ap,sigma_ep,lambda_p,sigma_as,
,sigma_es,lambda_s,tau,g0_L,Rl,Rl1,Rl2,Rr1,Rr2,alpha_1,alpha_2,alpha_p
,L,a);
%Rr_goal=0.6
[Ropt,eita]=Optimal_R_fiber_endpump_R(g0_L,Rr_goal,Rl,Rl1,Rr1,alpha_1,
alpha_p,L);
fg0=Ropt-Rr_goal;
count=0;count_max=20;
while abs(fg0)>1e-9&&count<count_max
    g1_L=g0_L+dg;

Rr_goal=Rth_1R_endpump_R(zspan,r,N,sigma_ap,sigma_ep,lambda_p,sigma_as,
,sigma_es,lambda_s,tau,g1_L,Rl,Rl1,Rl2,Rr1,Rr2,alpha_1,alpha_2,alpha_p
,L,a);

[Ropt,eita]=Optimal_R_fiber_endpump_R(g1_L,Rr_goal,Rl,Rl1,Rr1,alpha_1,
alpha_p,L);
fg1=Ropt-Rr_goal;
g0_L=abs(g0_L+fg0)/(fg0-fg1)*dg;

```

```

Rr_goal=Rth_1R_endpump_R(zspan,r,N,sigma_ap,sigma_ep,lambda_p,sigma_as
,sigma_es,lambda_s,tau,g0_L,Rl,Rl1,Rl2,Rr1,Rr2,alpha_1,alpha_2,alpha_p
,L,a);

[Ropt,eita]=Optimal_R_fiber_endpump_R(g0_L,Rr_goal,Rl,Rl1,Rr1,alpha_1,
alpha_p,L);
    fg0=Ropt-Rr_goal;
    count=count+1;
end
g0_L % single-pass gain at the kink point
eita % extraction efficiency at the kink point
-log(Rr_goal)/(alpha_1*L) % last column of Table 6-2

```

Table 9 BPM code for cladding-pumped IAG fiber lasers (implemented in Figure 4-4, Figure 4-5 and Figure 4-6)

```

% 2D-scalar BPM with PML
clear all
clc
% definition of structure
r=100; % core radius (um)
%L1=100; % cladding length um
%L2=124; % whole length
L1=340; % cladding length um
L2=400; % whole length
Lz=26e3; % propagation distance um
Lpml=20; % PML thickness
L=L2+2*Lpml;
nco=1.5689; ncl=1.5734; nair=1; % Corning SMF28, core, cladding and
air index
%ncl=1.5689; nco=1.5734;
lambda0=0.802; % um
k0=2*pi/lambda0;
epsilon0=8.854e-12;
mu0=1.2566e-6;
c=sqrt(1/epsilon0/mu0);
omega=2*pi*c/lambda0;
dx=2; dz=5; % um, dy=dx
N1=L1/dx+1; N2=L2/dx+1; Npml=Lpml/dx;
N=L/dx+1;
Nz=Lz/dz+1;
ref=1e-10;% PML Reflection
m=2;% order of PML
sigmax=(m+1)/2*epsilon0*c*nair/Lpml*log(1/ref); % sigma max
n=nair*ones(N,N); % refractive index

% Calculate sx/s, sy/s, PML definition
sxs=ones(N,N); % sx/s
sys=ones(N,N); % sy/s
lambda_launch=lambda0;
k0_launch=2*pi/lambda_launch;

```

```

nco_launch=nco;ncl_launch=ncl;
omega_launch=2*pi*c/lambda_launch;
for i=1:N
    if i<=Npml;
        sxs(:,i)=ones(N,1)/(1-li*sigmax*((Npml-
i+1)/Npml)^m/omega/epsilon0/nair^2);
        sys(i,:)=ones(1,N)/(1-li*sigmax*((Npml-
i+1)/Npml)^m/omega/epsilon0/nair^2);
    elseif i>=(N-Npml);
        sxs(:,i)=ones(N,1)/(1-li*sigmax*((i-
N+Npml)/Npml)^m/omega/epsilon0/nair^2);
        sys(i,:)=ones(1,N)/(1-li*sigmax*((i-
N+Npml)/Npml)^m/omega/epsilon0/nair^2);
    end
end

% field define, assume x polarized LP01 and LP11
Ex=zeros(N^2,Nz);
Ex0=zeros(N,N);
Ex1=zeros(N,N);
A=sparse(N^2,N^2);
B=sparse(N^2,N^2);

% filter indexes
Indi1=[];Indj1=[];
Indi2=[];Indj2=[];
for i=1:N
    for j=1:N
        R=sqrt((i-(N+1)/2)^2+(j-(N+1)/2)^2)*dx;
        if R<=r
            Indi1=[Indi1;i];Indj1=[Indj1;j];
        elseif R>=r&&R<=L1/2
            Indi2=[Indi2;i];Indj2=[Indj2;j];
        end
    end
end

% LP01 mode profile
idx1=sub2ind(size(Ex0),Indi1,Indj1);idx2=sub2ind(size(Ex0),Indi2,Indj2);
R1=sqrt((Indi1-(N+1)/2).^2+(Indj1-(N+1)/2).^2)*dx;
R2=sqrt((Indi2-(N+1)/2).^2+(Indj2-(N+1)/2).^2)*dx;

% index profile
neff_imag=-log(0.4)/3.3e-3/2/k0/1e6; % imaginary part of core index
n(idx1)=nco-li*neff_imag;
n(idx2)=ncl;

nn=zeros(N,N,Nz);
for Z=1:Nz
    nn(:,:,Z)=n;
end

figure
[X,Y]=meshgrid((0:(N-1))*dx-L/2,(0:Nz-1)*dz);

```

```

nn_xz=abs(squeeze(nn(:,(N+1)/2,:)));
nn_yz=abs(squeeze(nn((N+1)/2,:,)));
mesh(Y,X,nn_xz')
shading interp
figure
mesh(Y,X,nn_yz')
shading interp

% launch LP01 mode
% obtain neff
%1.448675164708124, 1.443997253441347
%r_launch=200;% launched mode radius, LP01 um
%neff_01_launch=LP01_neff_IAG(r_launch,nco_launch,ncl_launch,lambda0);
%neff_01_launch=neff_clad_fiber;
n0=nco; % reference index
Ex_launch=zeros(N,N);
%kt0_launch=k0_launch*sqrt(nco_launch^2-neff_01_launch^2);
%wt0_launch=k0_launch*sqrt(ncl_launch^2-neff_01_launch^2);
%Ex_launch(idx1)=besselj(0,2.405/r_launch*R1);
%Ex_launch(idx2)=besselj(0,2.405/r_launch*R2);
phi=0.4*rand(N); % phase noise amplitude
Ex_launch(idx1)=1*exp(1i*2*pi*phi(idx1));
Ex_launch(idx2)=1*exp(1i*2*pi*phi(idx2));
%Ex_launch(idx2)=besselj(0,kt0_launch*r)/besselh(0,1,wt0_launch*r)*bes
selh(0,1,wt0_launch*R2);
%Ex_launch((N+1)/2,(N+1)/2)=1;

% LPF method to generate the input field
%NA=0.22;
%X2=LPF_shaping(Ex_launch,N,NA,dx,lambda0); % low-pass filter shaping
%Ex_launch2=zeros(N,N);
%Ex_launch2(idx1)=X2(idx1);
%Ex_launch2(idx2)=X2(idx2);
%figure
%mesh(abs(Ex_launch2))
%shading interp
%Pp=sum(sum(abs(Ex_launch).^2));
%Pp2=sum(sum(abs(Ex_launch2).^2));
figure
[X,Y]=meshgrid((1:N)*dx-(N+1)/2*dx,(1:N)*dx-(N+1)/2*dx);
mesh(Y,X,abs(Ex_launch'))
shading interp
%Ex_launch=Ex_launch2;
Ex(:,1)=reshape(Ex_launch,N^2,1);
Pcore=zeros(Nz,1);Pclad=zeros(Nz,1);

alpha=0.5;
dx2=dx^2;
% gmres iteration
tol=1e-12;
maxit=100;
restart=20;
A=sparse(A);
B=sparse(B);
for Z=1:(Nz-1)
    % (i,j)=(1,1),(N,N)

```

```

B(1,2)=-1i*dz*(1-alpha)*sxs(1,1)*0.5*(sxs(2,1)+sxs(1,1))/dx2;
B(1,N+1)=-1i*dz*(1-alpha)*sxs(1,1)*0.5*(sxs(1,2)+sxs(1,1))/dx2;
B(1,1)=2*n0*k0-1i*dz*(1-alpha)*(k0^2*(nn(1,1,Z)^2-n0^2)-
sxs(1,1)*(0.5*sxs(2,1)+0.5*sxs(1,2)+3*sxs(1,1))/dx2);
A(1,2)=1i*dz*alpha*sxs(1,1)*0.5*(sxs(2,1)+sxs(1,1))/dx2;
A(1,N+1)=1i*dz*alpha*sxs(1,1)*0.5*(sxs(1,2)+sxs(1,1))/dx2;
A(1,1)=2*n0*k0+1i*dz*alpha*(k0^2*(nn(1,1,Z)^2-n0^2)-
sxs(1,1)*(0.5*sxs(2,1)+0.5*sxs(1,2)+3*sxs(1,1))/dx2);
for i=2:(N-1)
    % i=2:(N-1),j=1
    B(i,i+1)=-1i*dz*(1-
alpha)*sxs(i,1)*0.5*(sxs(i+1,1)+sxs(i,1))/dx2; % E(i+1,j)
    B(i,i-1)=-1i*dz*(1-alpha)*sxs(i,1)*0.5*(sxs(i-
1,1)+sxs(i,1))/dx2; % E(i-1,j)
    B(i,i+N)=-1i*dz*(1-
alpha)*sxs(i,1)*0.5*(sxs(i,2)+sxs(i,1))/dx2; % E(i,j+1)
    B(i,i)=2*n0*k0-1i*dz*(1-alpha)*(k0^2*(nn(i,1,Z)^2-n0^2)-
sxs(i,1)*(0.5*sxs(i+1,1)+0.5*sxs(i-
1,1)+0.5*sxs(i,2)+0.5*sxs(i,1)+2*sxs(i,1))/dx2); % E(i,j)
    A(i,i+1)=1i*dz*alpha*sxs(i,1)*0.5*(sxs(i+1,1)+sxs(i,1))/dx2; %
E(i+1,j)
    A(i,i-1)=1i*dz*alpha*sxs(i,1)*0.5*(sxs(i-1,1)+sxs(i,1))/dx2; %
E(i-1,j)
    A(i,i+N)=1i*dz*alpha*sxs(i,1)*0.5*(sxs(i,2)+sxs(i,1))/dx2; %
E(i,j+1)
    A(i,i)=2*n0*k0+1i*dz*alpha*(k0^2*(nn(i,1,Z)^2-n0^2)-
sxs(i,1)*(0.5*sxs(i+1,1)+0.5*sxs(i-
1,1)+0.5*sxs(i,2)+0.5*sxs(i,1)+2*sxs(i,1))/dx2); % E(i,j)
    % i=2:(N-1),j=N
    B(i+(N-1)*N,i+1+(N-1)*N)=-1i*dz*(1-
alpha)*sxs(i,N)*0.5*(sxs(i+1,N)+sxs(i,N))/dx2; % E(i+1,j)
    B(i+(N-1)*N,i-1+(N-1)*N)=-1i*dz*(1-alpha)*sxs(i,N)*0.5*(sxs(i-
1,N)+sxs(i,N))/dx2; % E(i-1,j)
    B(i+(N-1)*N,i+(N-2)*N)=-1i*dz*(1-alpha)*sxs(i,N)*0.5*(sxs(i,N-
1)+sxs(i,N))/dx2; % E(i,j-1)
    B(i+(N-1)*N,i+(N-1)*N)=2*n0*k0-1i*dz*(1-
alpha)*(k0^2*(nn(i,N,Z)^2-n0^2)-sxs(i,N)*(0.5*sxs(i+1,N)+0.5*sxs(i-
1,N)+0.5*sxs(i,N)+0.5*sxs(i,N-1)+2*sxs(i,N))/dx2); % E(i,j)
    A(i+(N-1)*N,i+1+(N-
1)*N)=1i*dz*alpha*sxs(i,N)*0.5*(sxs(i+1,N)+sxs(i,N))/dx2; % E(i+1,j)
    A(i+(N-1)*N,i-1+(N-1)*N)=1i*dz*alpha*sxs(i,N)*0.5*(sxs(i-
1,N)+sxs(i,N))/dx2; % E(i-1,j)
    A(i+(N-1)*N,i+(N-2)*N)=1i*dz*alpha*sxs(i,N)*0.5*(sxs(i,N-
1)+sxs(i,N))/dx2; % E(i,j-1)
    A(i+(N-1)*N,i+(N-1)*N)=2*n0*k0+1i*dz*alpha*(k0^2*(nn(i,N,Z)^2-
n0^2)-sxs(i,N)*(0.5*sxs(i+1,N)+0.5*sxs(i-
1,N)+0.5*sxs(i,N)+0.5*sxs(i,N-1)+2*sxs(i,N))/dx2); % E(i,j)
end

for j=2:(N-1)
    % j=2:(N-1),i=1
    B(1+(j-1)*N,2+(j-1)*N)=-1i*dz*(1-
alpha)*sxs(1,j)*0.5*(sxs(2,j)+sxs(1,j))/dx2; % E(i+1,j)
    B(1+(j-1)*N,1+j*N)=-1i*dz*(1-
alpha)*sxs(1,j)*0.5*(sxs(1,j+1)+sxs(1,j))/dx2; % E(i,j+1)

```

```

        B(1+(j-1)*N,1+(j-2)*N)=-1i*dz*(1-alpha)*sxs(1,j)*0.5*(sxs(1,j-
1)+sxs(1,j))/dx2; % E(i,j-1)
        B(1+(j-1)*N,1+(j-1)*N)=2*n0*k0-1i*dz*(1-
alpha)*(k0^2*(nn(1,j,Z)^2-n0^2)-
sxs(1,j)*(0.5*sxs(2,j)+0.5*sxs(1,j)+0.5*sxs(1,j+1)+0.5*sxs(1,j-
1)+2*sxs(1,j))/dx2); % E(i,j)
        A(1+(j-1)*N,2+(j-
1)*N)=1i*dz*alpha*sxs(1,j)*0.5*(sxs(2,j)+sxs(1,j))/dx2; % E(i+1,j)
        A(1+(j-
1)*N,1+j*N)=1i*dz*alpha*sxs(1,j)*0.5*(sxs(1,j+1)+sxs(1,j))/dx2; %
E(i,j+1)
        A(1+(j-1)*N,1+(j-2)*N)=1i*dz*alpha*sxs(1,j)*0.5*(sxs(1,j-
1)+sxs(1,j))/dx2; % E(i,j-1)
        A(1+(j-1)*N,1+(j-1)*N)=2*n0*k0+1i*dz*alpha*(k0^2*(nn(1,j,Z)^2-
n0^2)-sxs(1,j)*(0.5*sxs(2,j)+0.5*sxs(1,j)+0.5*sxs(1,j+1)+0.5*sxs(1,j-
1)+2*sxs(1,j))/dx2); % E(i,j)
        % j=2:(N-1),i=N
        B(N+(j-1)*N,N-1+(j-1)*N)=-1i*dz*(1-alpha)*sxs(N,j)*0.5*(sxs(N-
1,j)+sxs(N,j))/dx2; % E(i-1,j)
        B(N+(j-1)*N,N+j*N)=-1i*dz*(1-
alpha)*sxs(N,j)*0.5*(sxs(N,j+1)+sxs(N,j))/dx2; % E(i,j+1)
        B(N+(j-1)*N,N+(j-2)*N)=-1i*dz*(1-alpha)*sxs(N,j)*0.5*(sxs(N,j-
1)+sxs(N,j))/dx2; % E(i,j-1)
        B(N+(j-1)*N,N+(j-1)*N)=2*n0*k0-1i*dz*(1-
alpha)*(k0^2*(nn(N,j,Z)^2-n0^2)-sxs(N,j)*(0.5*sxs(N,j)+0.5*sxs(N-
1,j)+0.5*sxs(N,j+1)+0.5*sxs(N,j-1)+2*sxs(N,j))/dx2); % E(i,j)
        A(N+(j-1)*N,N-1+(j-1)*N)=1i*dz*alpha*sxs(N,j)*0.5*(sxs(N-
1,j)+sxs(N,j))/dx2; % E(i-1,j)
        A(N+(j-
1)*N,N+j*N)=1i*dz*alpha*sxs(N,j)*0.5*(sxs(N,j+1)+sxs(N,j))/dx2; %
E(i,j+1)
        A(N+(j-1)*N,N+(j-2)*N)=1i*dz*alpha*sxs(N,j)*0.5*(sxs(N,j-
1)+sxs(N,j))/dx2; % E(i,j-1)
        A(N+(j-1)*N,N+(j-1)*N)=2*n0*k0+1i*dz*alpha*(k0^2*(nn(N,j,Z)^2-
n0^2)-sxs(N,j)*(0.5*sxs(N,j)+0.5*sxs(N-
1,j)+0.5*sxs(N,j+1)+0.5*sxs(N,j-1)+2*sxs(N,j))/dx2); % E(i,j)
    end
    for i=2:(N-1)
        indj=2:(N-1);
        idxj1=sub2ind(size(A),i+(indj-1)*N,i+1+(indj-1)*N);
        idxj2=sub2ind(size(A),i+(indj-1)*N,i-1+(indj-1)*N);
        idxj3=sub2ind(size(A),i+(indj-1)*N,i+indj*N);
        idxj4=sub2ind(size(A),i+(indj-1)*N,i+(indj-2)*N);
        idxj5=sub2ind(size(A),i+(indj-1)*N,i+(indj-1)*N);
        B(idxj1)=-1i*dz*(1-
alpha)*sxs(i,indj)*0.5*(sxs(i+1,indj)+sxs(i,indj))/dx2; % E(i+1,j)
        B(idxj2)=-1i*dz*(1-alpha)*sxs(i,indj)*0.5*(sxs(i-
1,indj)+sxs(i,indj))/dx2; % E(i-1,j)
        B(idxj3)=-1i*dz*(1-
alpha)*sxs(i,indj)*0.5*(sxs(i,indj+1)+sxs(i,indj))/dx2; % E(i,j+1)
        B(idxj4)=-1i*dz*(1-alpha)*sxs(i,indj)*0.5*(sxs(i,indj-
1)+sxs(i,indj))/dx2; % E(i,j-1)
        B(idxj5)=2*n0*k0-1i*dz*(1-alpha)*(k0^2*(nn(i,indj,Z).^2-n0^2)-
sxs(i,indj)*(0.5*sxs(i+1,indj)+0.5*sxs(i-
1,indj)+0.5*sxs(i,indj+1)+0.5*sxs(i,indj-1)+2*sxs(i,indj))/dx2); %
E(i,j)
    end

```

```

A(idxj1)=1i*dz*alpha*sxs(i,indj)*0.5.*(sxs(i+1,indj)+sxs(i,indj))/dx2;
% E(i+1,j)
    A(idxj2)=1i*dz*alpha*sxs(i,indj)*0.5.*(sxs(i-
1,indj)+sxs(i,indj))/dx2; % E(i-1,j)

A(idxj3)=1i*dz*alpha*sxs(i,indj)*0.5.*(sxs(i,indj+1)+sxs(i,indj))/dx2;
% E(i,j+1)
    A(idxj4)=1i*dz*alpha*sxs(i,indj)*0.5.*(sxs(i,indj-
1)+sxs(i,indj))/dx2; % E(i,j-1)
    A(idxj5)=2*n0*k0+1i*dz*alpha*(k0^2*(nn(i,indj,Z).^2-n0^2)-
sxs(i,indj).*(0.5*sxs(i+1,indj)+0.5*sxs(i-
1,indj)+0.5*sxs(i,indj+1)+0.5*sxs(i,indj-1)+2*sxs(i,indj))/dx2); %
E(i,j)
    end
    Ex(:,Z+1)=gmres(A,(B*Ex(:,Z)),restart,tol,maxit);
    Z
end
Ex3D=zeros(N,N,Nz);
for Z=1:(Nz-1)
    Ex3D(:,:,Z)=reshape(Ex(:,Z),N,N);
    temp=Ex3D(:,:,Z);
    Pcore(Z)=sum(abs(temp(idx1)).^2);
    Pclad(Z)=sum(abs(temp(idx2)).^2);
end
figure
plot((0:(Nz-2))*dz,Pcore(1:Nz-1)/Pcore(1),(0:(Nz-2))*dz,Pclad(1:Nz-
1)/Pclad(1),'r',(0:(Nz-2))*dz,Pcore(1:Nz-1)/(Pcore(1)+Pclad(1)),'k')
figure
[X,Y]=meshgrid((0:(N-1))*dx-L/2,(0:Nz-1)*dz);
Ex_xz=abs(squeeze(Ex3D(:,(N+1)/2,:)));
Ex_yz=abs(squeeze(Ex3D((N+1)/2,:,:)));
mesh(Y,X,Ex_xz')
shading interp
figure
mesh(Y,X,Ex_yz')
shading interp
[X1,Y1]=meshgrid((0:(N-1))*dx-L/2,(0:(N-1))*dx-L/2);
Ex_xy=abs(squeeze(Ex3D(:,:,Nz-1)));
figure
mesh(Y1,X1,Ex_xy')
shading interp

```